UNIVERSITÀ
DEGLI STUDI
DI PADOVA

University Centre of Studies and Activities for Space
"Giuseppe Colombo"- CISAS
University of Padova, Italy

Course: Space Science Technology and Measurement (STMS)

Curriculum: Mechanical Measurements for Engineering and Space (MMIS)

Cycle: XXX °

Power Stages and Control of Wireless Power Transfer Systems (WPTSs)

School director: Prof. Giampiero Naletto

Supervisor: Prof. Giuseppe Buja

PhD student
Rupesh Kumar Jha
Metricola: 1108596

Abstract

Wireless charging of electric vehicle (EV) batteries by inductive power transfer (IPT) offers unique advantages compared to conventional conductive chargers. Due to the absence of a galvanic connection, the charging process requires no user interaction and no moving of mechanical components. For public transport systems, e.g., public buses or tramways, this makes possible a fully automated opportunity charging at bus stations, taxicab stands, or traffic lights. The schematic of wireless battery charger (WBC) is made of two stages, one is transmitter stage and another one is receiver stage. Both the stages include coils and capacitors to resonate at the supply frequency along with power conversion circuits. The transmitter coil is buried in the ground while receiving coil is situated in the vehicle.

Based on the connection of resonating capacitors four topologies are possible which can be divided into two arrangements i) transmitter capacitor in series while receiver capacitor is in either series or in parallel, giving rise to SS and SP topologies, ii) transmitting capacitor in parallel while receiving capacitor is in either series or in parallel, giving rise to PS and PP topologies. In the thesis, these topologies have been studied in detail in terms of efficiency, power sizing of supply inverter and resonating coils, behavior under the extreme condition of open and short circuit of the receiver.

Power conversion circuitry of a WBC system includes a diode rectifier to supply the load with a direct voltage and resorts to different solutions for charging the battery. The two most used solutions are either in a straightforward manner through the diode rectifier or through a chopper in cascade to the diode rectifier. These two arrangements have been discussed and compared in terms of efficiency and power sizing of supply inverter and transmitting and receiving coil, including the selection of the optimum chopper input voltage.

Due to aging and thermal effect, the parameters of the reactive components of a WBC system may change and this can deviates the resonance frequency from the supply frequency. In this thesis the impact of such mismatch on efficiency and supply inverter power sizing factor of WBC with SS topology has been studied. Three supply frequency updating techniques to keep in resonance either the transmitter stage or the receiver stage or the impedance seen from power supply have been investigated.

The thesis continues with the study of high power WBC systems which includes power supply architecture, core material and coil geometry. A review of different power supply architectures such as single phase with two stage and parallel topologies including their merits and demerits have been presented. Reviewing some paper on coil geometry, DD coil is found to be suitable for high power application. Using JMAG simulation tool, a transmitter track of three DD coils and a receiver with one DD coil has been analyzed when receiver is moving on the transmitting track.

Due to disfavor of ferrite as a core material for high-power WBC system, a varieties of different powdered magnetic materials have been considered here and compared in terms of saturated value of the magnetic flux density, magnetic properties -like dependency of their permeability on temperature, magnetic field strength and frequency-, power losses and cost.

At last, two methods to model the WPT system have been considered. The methods model the system by considering the envelop of the signals.

Sommario

La ricarica wireless delle batterie a bordo dei veicoli elettrici, ottenuta utilizzando il trasferimento di potenza induttivo, offre vantaggi unici rispetto ai caricabatterie tradizionali. A causa dell'assenza di una connessione galvanica, il processo di ricarica non richiede alcuna interazione dell'utente né alcuna movimentazione di un componente meccanico. Per i sistemi di trasporto pubblico, ad esempio autobus o tram, questo rende possibile la cosiddetta carica di opportunità completamente automatizzata presso i depositi degli autobus, le corsie dei taxi, o ai semafori. I caricabatterie wireless sono costituiti da due stadi: uno stadio trasmittente e uno stadio di ricezione. Entrambi gli stadi includono bobine e condensatori, dimensionati per risuonare alla frequenza di alimentazione, e convertitori statici di potenza. La bobina del trasmettitore è interrata nel manto stradale, mentre la bobina ricevente è situata a bordo del veicolo.

Sulla base della connessione dei condensatori risonanti sono possibili quattro topologie circuitali diverse che possono essere raggruppate in due principali: i) un condensatore in serie con la bobina di trasmissione con il condensatore lato ricevitore in serie o in parallelo costituisce le topologie SS e SP, rispettivamente, e ii) un condensatore in parallelo alla bobina di trasmissione con il condensatore della sezione ricevente in serie o in parallelo costituisce le topologie PS e PP, rispettivamente. Nella tesi queste topologie sono state studiate dettagliatamente in termini di efficienza, dimensionamento dell'invertitore di alimentazione e progetto delle bobine risonanti, e di comportamento nelle condizioni estreme di circuito aperto e di cortocircuito del ricevitore.

Il circuito di conversione di potenza di un sistema per la ricarica wireless induttiva di un veicolo elettrico include un raddrizzatore a diodi nello stadio di ricezione per ottenere un bus di tensione in continua e utilizza differenti modi per caricare la batteria del veicolo. Le due soluzioni più diffuse eseguono la carica o direttamente attraverso il raddrizzatore a diodi oppure attraverso un chopper collegato in cascata ad esso. Queste due modalità sono state discusse e confrontate in termini di efficienza, di dimensionamento sia dell'invertitore di alimentazione, che delle bobine di trasmissione e ricezione, includendo nell’analisi la scelta della tensione ottima in ingresso al chopper.

A causa dell'invecchiamento e dell'effetto termico, i parametri dei componenti reattivi di un circuito di ricarica wireless possono variare e questo fa sì che la frequenza di risonanza e la frequenza di alimentazione non siano perfettamente identiche. In questa tesi è stato studiato l'impatto che tale deviazione ha sull'efficienza e sul dimensionamento dell’invertitore in un sistema di ricarica wireless con topologia SS. Sono state studiate tre tecniche di adattamento della frequenza di alimentazione per mantenere in risonanza o lo stadio trasmittente o quello di ricezione oppure l’impedenza vista dall’alimentazione.

La tesi prosegue con lo studio dei sistemi di ricarica wireless per elevate potenze che richiedono una specifica architettura di alimentazione, particolari materiali per la costruzione del nucleo magnetico, oltre ad una peculiare geometria delle bobine. E’ stata presentata una panoramica di diverse architetture di alimentazione come, ad esempio, le topologie monofase a due stadi e in parallelo, inclusi i loro pregi e svantaggi. Sulla base di un’accurata revisione

della letteratura della geometria delle bobine, la geometria DD si è rivelata essere la più conveniente per le applicazioni di alta potenza. Utilizzando il codice agli elementi finiti JMAG, è stato simulato il comportamento di un sistema di ricarica wireless costituito da tre bobine di trasmissione e una bobina di ricezione, tutte di tipo DD.

Poiché, date le sue caratteristiche, le ferriti non si prestano bene per sistemi ad alta potenza, sono state considerate altre tipologie di materiali magnetici. Sono state analizzate e confrontate diverse leghe amorfe in base all'induzione magnetica di saturazione, alle proprietà magnetiche, come la dipendenza della permeabilità dalla temperatura, dal campo magnetico applicato e dalla frequenza, alle perdite di potenza e al costo.

Infine, sono stati considerati due metodi per modellizzare il WPT. I metodi modellizzano il sistema considerando l'inviluppo dei segnali.

Dedicated to my mother

Acknowledgement

I would like to express my deepest gratitude to each and every one who helped me with their constant support and motivation during my doctoral program. At first, I would like to thank my supervisor Professor Giuseppe Buja for his supervision and experienced guidance. His continuous support and encouragements gave me more confidence in my research and successful accomplishment of the course. I would also like to thank Professor Manuele Bertoluzzo for his valuable guidance, cooperation, constructive discussions and support that enriched my knowledge and skills. I would also like to thank Dr. Ritesh Keshri for his sincere support during my program.

I am grateful to my supervisor Prof. Buja and thank him once again who ensured full funding for all three years during my stay in Padova and provided hassle-free economic environment. In this order, I would like to acknowledge *Fondazione Ing. Aldo Gini* for the research grant and university of Padova for the research fellowship.

This journey would have not been pleasant without my friends and fellows, in this way I would like to thank to my lab colleagues Kishore, Syamnaresh, Kundan, Hemant, Christian, Mattia, Stefano, Shreya, Filippo and Elena for their help and healthy work environment, and I show my gratitude in the same way to Kishore, Sandhya, Nisarg, Mamta, Jagjeet, Pandy, Sarada, Arpit, Elina, Soni, Maiti, Sushmitha, Pankaj, Jitendra, Munna, Shivam, Gaurav, Sehaj, Saurabh, Anna, Maria, Shashank, Federica, Federico and all.

At last but not the least, I always remember my family that is my biggest support and source of motivation. I am grateful and would like to thank my parents to promote me to enhance my career, and many thanks to my sisters Shweta, Navita and brother Brajesh for their moral support.

Contents

NOMENCLATURE			
A_S	Power source power sizing	P_I	P_B at beginning of battery charging
A_T	Transmitter coil power sizing	P_S	Active power delivered by the power source
A_R	Receiver coil power sizing	P_B	Power absorbed by the battery
C_T, C_R	Transmitter and receiver resonant capacitors	V_{co}	I_B at cutoff
C_{DC}	DC bus capacitor	V_M	V_B in CV mode
CC	Constant current mode	P_F	P_B at completion of battery charging (at I_{co})
CV	Constant voltage mode	P_N	Nominal battery power defined as V_M I_{CC}
I_B	Battery current	R_L	Load resistance seen from the receiver terminals
$\bar{I}_C$	Current through receiver resonating capacitor	r_T, r_R	Transmitter and receiver coil parasitic resistances
$\bar{I}_T$, $\bar{I}_R$	Transmitter and receiver current	r_S	Power source internal resistance
$\bar{I}_{L,s}$, $\bar{I}_{L,P}$	Current at diode rectifier input for SS and SP topology	$\bar{V}_{Tt}$, $\bar{V}_{Rt}$	Terminal voltage of transmitter and receiver coils
$\bar{I}_S$	Supply current	$\bar{V}_T$, $\bar{V}_R$	Voltage induced in the transmitter and receiver coils due to M
I_{CC}	I_B in CC mode	$\bar{V}_{L,s}$, $\bar{V}_{L,P}$	Voltage at diode rectifier input for SS and SP topology
I_{DC}	Current upstream chopper capacitor	V_{DC}	Voltage across chopper capacitor
I_{co}	I_B at cutoff	V_B	Battery voltage
k	Coil coupling coefficient	$\bar{V}_S$	Supply voltage
L_T, L_R	Transmitter and receiver coil inductances	V_{DC}	Voltage across chopper capacitor
M	Coil mutual inductance	$\dot{Z}_T$, $\dot{Z}_R$	Impedances of transmitter and receiver stages
Instantaneous value of a quantity is denoted with a lower-case symbol. Rms and average values are denoted with an upper-case symbol. Phasor representation of a sinusoidal quantity is denoted with a bar over the upper-case symbol. Power sizing data are normalized to the nominal battery power.			

Chapter 1

Introduction

1.1 Background

The rapid increase in global warming and the energy scarcity are the big concerns for the society and mother earth. Internal combustion engine-based vehicles are still the major means of transportation and the source of a large part of pollution. Rapid growth of automobile industries and increasing car ownership have lead into environmental pollution, shortage of energy source and other issues. These issues arising from automobile industries have moved researchers from all the world to give more attention on it. Possibilities to improve this situation are either promoting the vehicle efficiency improvements or shift to alternative energy source and vehicle technologies. Electric vehicle (EV) is the best suitable option among existing technologies since it offers high efficiency, lower noise, zero emission etc. There are *several* electric vehicles available like, Nissan Leaf, Mitsubishi iMiev, Renault Fluence and so on. However EV suffers from high purchase cost, performance, autonomy and recharging limitation which prevent it from being true alternatives. Government is investing a lot of manpower and material resources to develop public recharging infrastructure to make it accessible for all and researches on energy storage (e.g battery) are going on in order to make EV less costly.

1.2 Historical background of EVs

Electric vehicle is not new invention and as a matter of fact have been around since before the internal combustion engine vehicles. In 1834 Thomas Davenport first made EVs and during 1890s EVs were sold ten times more than gasoline cars. EVs ruled the roadway vehicle and showrooms and remained more popular until mid 1910s. Some popular car manufacturing companies like Studebaker and Oldsmobile started as an EV manufacturing company before switching to manufacture combustion engine vehicles. Till mid- 1910s EVs were first choice for customers as well as manufacturers. Emerging combination of cheap oil and the non-electrification overcomes the EVs technology and ICE vehicle took place of it.

From 60s to 80s, a number of events materialized in order to make aware of negative environmental effects but nobody took it seriously and ignored it. Since 70s, 80s and 90s many nations realized the negative aspect of it and shortage of foreign oil. Awareness of negative aspect of combustion fuel as well as dependency of ICE engine on it resulted into the re-emergence of EVs. In the late 90s a new technology related to the EVs got introduced to the market the hybrid. Hybrid cars mainly runs on gasoline but are equipped with battery which get charged during braking and function when driving under certain speed, resulting into one third reduction in fuel consumption.

Success of Toyota car manufacturing company bring a new revolution towards EVs. Many car maker went for plug-in hybrid electric vehicles (PHEV) which have smaller combustion engine but larger battery pack and electric motors.

1.3 The benefits from EV utilization

Electric vehicle (EV) is the best suitable option among existing technologies since it offers [1]

A. Low energy consumption

Most of the conventional cars however convert approx. 20% of the gasoline energy into engine energy, EVs use 90% of its electric energy charged into the battery to deliver power to car motors. Apart from high efficiency, the ability of EV to be charged during off-peak period makes it more convenient to use excess power produced by generator.

B. No more oil dependency

Oil and fossil fuel are primary source of energy, which, with the passes of time and heavy consumption of it is getting limited, and now are the scarce energy source of energy. In the U.S. 40% of energy comes from petroleum of which 40% goes to automobiles. Electrification of transport will play major role to reduce oil dependency.

C. Environmental impacts

EVs have good impact on environment as they reduce the overall energy consumption and air pollution. A study in U.S. shows that, due to elimination of ICE, total volatile organic compound (VOC), carbon monoxide (CO) and NOx emissions are reduced significantly. A study on the impact of using EVs powered by electricity generated by coal power plants clarify that green house gas (GHG) emissions can be controlled by 59% compared to ICE vehicle. So even EV is powered by electricity generated by coal, the emission of GHG would be lower compared to ICE vehicle. One should not only think about the emission from the vehicle itself but also on the polluting steps in its whole life cycle. In case of EV increasing amount of waste batteries brings slight negative impact to environment. Fortunately, lithium ion battery is more environmental friendly than other battery like lead-acid, and Nickel–cadmium.

1.4 Conventional battery charging and introduction of wireless power transfer (WPT)

In accordance with the technological development, EV can be divided into pure battery EV, hybrid EV and fuel cell EV of three types. Conventional charging scheme i.e wired charging is capable to charge EV by connecting physically the charging station and vehicles. And hence, is not trustworthy for human beings due to presence of exposed conductors, interlocks and connector that may cause electric shock hazardous which motivated and inspired researches and companies to move from wired to wireless charging. In addition to the overcome of the demerits associated with wired charging there are other advantages associated with EV wireless charging, for example, opportunity-charging scenarios, where the vehicle is idle during traffic or parking for a short time. This concept is very well suited for mass transit application where, using this technique, bus can be charged while passengers are embarking and disembarking from bus.

There are three WPT technologies, which are electric (capacitive), magnetic (inductive), and electromagnetic (radiation). Among all these technologies magnetic WPT technology is found

to be most appropriate for EV charging since electromagnetic WPT technology suffers from a heavy demand of direct-line-of sight transmission path, complicated tracking system and large size antenna, while capacitive WPT technology is limited due to its small power capabilities and trivial transmission range.

Schematics of wireless battery charger (WBC) is drawn in Fig. 1.4.1. It is made of two stages, the transmitter that is fed by the grid and the receiver that charges the EV battery. In addition to the resonant coil, each stage includes a power conversion circuitry; in the transmitting stage it consists of a rectifier and a high-frequency inverter. Depending upon the series or parallel connected resonant capacitor in the transmitter stage, power source can be either a voltage source or a current source. The power conversion circuitry of the receiver consists of another rectifier that usually charges the battery through a chopper.

1.5 Objective of the thesis

- To understand and carry out a review of existing technologies for wireless battery charging system.
- To investigate and study of different resonant technique for WBC system in terms of efficiency, power sizing of power source inverter and coil set.
- To investigate the performance of WBC system for two different receiver arrangement where one arrangement charges the battery with chopper while another one does without chopper.
- To study the effect of parameter deviation due to aging on the performance of resonant WBC system. Different possible technique to overcome or compensate such weakness and selection of one based on efficiency and power sizing of supply system.
- To study the power supply structures, core materials and coil geometry for high power WBC system.
- To develop a dynamic model for WBC system.

Thesis Structure

This thesis is organized in nine chapters including the introduction. The outline of thesis is mentioned below.

Chapter 2

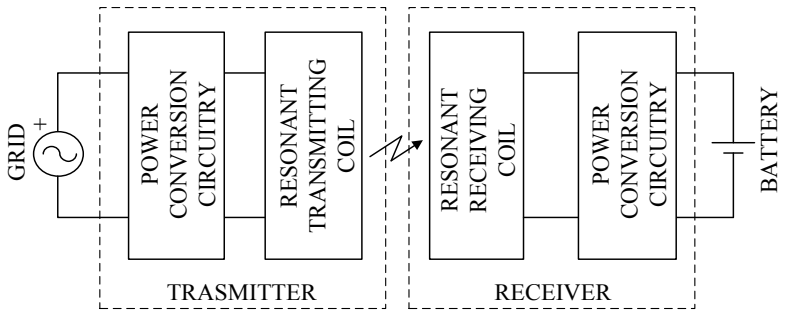

Fig. 1.4.1 WBC schematics

Starting from the necessity and importance of wireless power transfer technology, this chapter gives an overview of different possible technique for it and explain in detail the best suitable technique i.e. inductive power transfer. Configuration of WBC system and its structure is illustrated in detail.

Chapter 3

Starting with the different basic compensation topologies possible for WBC system, some figures of merits have been suggested. All the four possible WBC configuration have been studied in detail and compared on the basis of decided figures of merits.

Chapter 4

According to chapter 3 SS topology is found to be suitable one among all, this chapter presents two charging arrangement for SS resonant WBC system. These two suggested arrangements have been evaluated and compared in order to find suitable one for WBC.

Chapter 5

Selecting the suitable arrangement from chapter 4, this chapter continues with the study of WBC system during mismatch of supply frequency with LC pair resonant frequency. Three different types of frequency tuning have been studied and compared in terms of better performance.

Chapter 6

Evolution of WBC system in these days follows with its adaptability for high power level, which not only increases the range of power transfer and make it suitable for public transport like bus and train but reduces battery-charging time. Therefore, this chapter of the thesis deals with the power supply system for high power WBC system. It presents basic review for different power supply architecture available for WBC system including their advantages and disadvantages.

Chapter 7

Continuing the research for high power WBC system, this chapter presents a study on different coil geometries available for WBC system. Based on the literature survey, DD coil has been studied in this chapter. Later on, a track of three DD coils while receiver DD coil is moving has been analyzed in this chapter.

Chapter 8

This chapter discusses the different magnetic material available for high power WBC system. Starting from the approach for their development and manufacturing process, classification of magnetic materials and their detailed investigations are presented.

Chapter 9

This chapter includes the dynamic modeling of the WBC system. Two methods such as Generalized State Space Averaging (GSSA) and Laplace Phasor Transform (LPT) technique have been discussed here.

1.6 References

[1] Allen, D. T.; Shonnard, D. R. Green Engineering: Environmentally Conscious Design of Chemical Processes; Prentice Hall: New York, 2001.

Chapter 2

Electric vehicles and Wireless battery charging

2.1 Introduction

Vehicles powered by electricity have the potential to reduce many of the problems like smog forming and global warming. Electric vehicles powered by a clean electricity grid offer a key pathway to achieve significant reduction in global warming. Powered by domestically produced electricity, electric vehicles could be a significant part of reducing oil dependence [1], [2].

Electric vehicles are propelled by an electric motor that is supplied with power from a rechargeable battery. In recent scenario of battery charging due to many unwanted precautions and massy arrangement, options of wireless charging are being investigated. History of wireless power transfer (WPT) began when Nikola Tesla invented his famous Tesla coil in 1891. Motivation for using WPT technique for charging of EV comes from the presence of exposed conductor, interlocks and connectors that may cause electric sock hazards which is against human safety [3]. Other advantages with WPT are no need of physical infrastructure like grids and in this way there is no need to manage the charging station after rains and natural disasters. In addition to above mentioned advantages the technique of WPT is suitable for opportunity charging scenarios, where the vehicle is idle during traffic or parking for a short time [4]. This concept is very well suited for mass transit application, where using this technique bus can be charged while passengers are embarking and disembarking from bus.

There are various techniques of wireless power transfer, but among them resonant inductive power transfer (IPT) is preferred technology for transportation application. A brief introduction of all the different WPT techniques are presented and explanation of IPT charging technique is done in this chapter.

2.2 Moving from wired to wireless charging

The use of wireless EV charging is strongly recommended because of the following shortcomings associated with the current wired EV charging

a. The current standards for EVs by Society of Automotive Engineers (SAE) make use of J1772, a North American standard for electric connectors used in EVs. Even if it is efficient, it must be prevented from inadvertent disconnections. Along with this it must have grounded pole which is first to make contact and last to break contact, and it must contain an interlock device to prevent vehicle startup while connected.
b. The EV inlet must be energized until it is attached to the EV supply equipment and also must be de-energized prior to removal of the connector. No EV inlet is present in the wireless system.
c. Depending on the output of public charging stations may at times be quite inconvenient. Unlike a couple of minutes at the gas station, electric charging via EV supply equipment may require plugging in for three-four hours to get a full charge.
d. The need for multiple charging standards and plug standards would be reduced.

(a) (b)

Fig. 2.3.2 (a) capacitive coupling (b) magnetic coupling

e. The power pads would only operate when the vehicle is parked above it and thus cuts down on the costs of charging

2.3 Wireless power transfer systems (WPTSs)

Wireless Power Transfer is the transmission of electric power from one point to another through air without the use of wire. WPTSs are made of two stages, transmitter and receiver, as shown in Fig. 2.3.1. Both of them consist of a power converter, a coupling device and an electronic control unit (ECU). There are three main types of WPT technologies electric (capacitive), magnetic (inductive), and electromagnetic (radiation) [5] which are discussed below.

2.3.1 Electric (capacitive) WPT

Electric or capacitive WPT technology uses alternate electric field to transfer the power. Electrical coupling device is shown in Fig. 2.3.2 (a). Electrical energy delivered via a high-frequency oscillating power electronic converter is connected to two primary metal plates. When two isolated secondary plates are placed in addition, an alternating electric field is formed between the plates resulting in a displacement current that can flow through. As a result, power can be transferred to the load without direct electrical contact and a certain freedom of movement between the primary and secondary plates is possible [6].

2.3.2 Magnetic (inductive) WPT

Inductive power transfer is a popular technique of wireless power transfer which falls in the category of magnetic WPTS [7]. It works on the same principle of transformer where one coil transfers power to another coil by means of electromagnetic induction as shown in Fig. 2.3.2 (b). In the case of EV charging, since there is large airgap between the two coils it suffers from large leakage inductance, which results into some drawbacks [8], outlined as

i) Not efficient for EV charging.
ii) Need large VA sizing of power source

Thanks to resonant technique, which is explained later, removes all the limitation of traditional IPT by increasing its efficiency, reducing size of power source and so extending

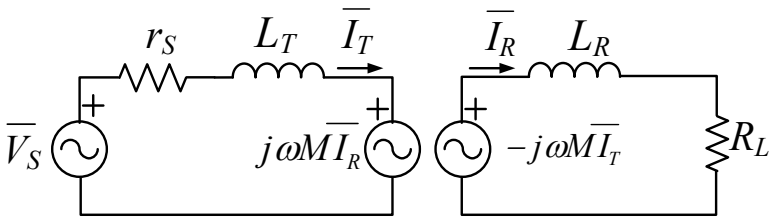

Fig. 2.4.1 IPT system

the power transfer range. Resonant IPT system needs capacitors connected with transmitting and receiving coils to resonate at supply frequency.

2.3.3 Electromagnetic (radiation) WPT

Power transmission via radio waves can be made more directional, allowing longer distance power beaming, with shorter wavelengths of electromagnetic radiation, typically in the microwave range. A rectenna may be used to convert the microwave energy back into electricity. Rectenna conversion efficiencies exceeding 95% have been realized. Power beaming using microwaves has been proposed for the transmission of energy from orbiting solar power satellites to Earth and the beaming of power to spacecraft leaving orbit has been considered [9].

Table 2.1 compares the WPT technologies in terms of power transfer, range and efficiency. It is found that resonant IPT is the most suitable technology for EV charging.

2.4 Basics of IPT and need of resonance

In two magnetically coupled coil, if one coil is energized with alternating current, the other one gets induced emf. This is Faraday's law, and the same principle can be used in loosely coupled coils in WPT system for battery charging of EVs.

The electric circuitry of an inductive coupling WPTS is shown in Fig. 2.4.1, where $\overline{V}_S$ is the controlled voltage source, obtained by means of a front-end rectifier cascaded by a square-wave, high frequency voltage inverter (explained in detail in the next section of this chapter), L_T and L_R are the self-inductances of the transmitting and the receiving coils, M is their mutual inductance, and r_S and R_L are the power source internal resistance and load resistances. R_L

Table #2.1

Technology	Power	Range	Efficiency	Comments
Traditional IPT	High	Low	High	Too small range for EV charging
Resonant IPT	High	Medium	High	Capable for EV charging
Electromagnetic field	High	High	High	Need direct line-of-sight transmission path, large antennas, and complex tracking mechanisms.
Capacitive power transfer	Low	Low	High	Both power and ranges are too small for EV charging

represents the voltage/current ratio at the battery terminals during charging, referred to the receiver coil. An important role (for the efficiency) is exerted by the parasitic resistance of the coils, which here are neglected.

Voltage equations of the transmitter and receiver stages are

$$\begin{cases} \bar{V}_S = \dot{Z}_T \bar{I}_T + j\omega M \bar{I}_R \\ -j\omega M \bar{I}_T = \dot{Z}_R \bar{I}_R \end{cases} \tag{2.4.1}$$

where $\dot{Z}_T$ and $\dot{Z}_R$ are impedances of transmitter and receiver stages respectively which are given as,

$$\begin{aligned} \dot{Z}_T &= r_S + j\omega L_T \\ \dot{Z}_R &= R_L + j\omega L_R \end{aligned} \tag{2.4.2}$$

Here, ω is the angular frequency of $\bar{V}_S$. From (2.4.1), the currents flowing in the transmitter and receiver stages are derived as

$$\begin{cases} \bar{I}_T = \frac{\bar{V}_S \dot{Z}_R}{\dot{Z}_T \dot{Z}_R + \omega^2 M^2} \\ \bar{I}_R = -\frac{\bar{V}_S j\omega M}{\dot{Z}_T \dot{Z}_R + \omega^2 M^2} \end{cases} \tag{2.4.3}$$

By (2.4.1) and (2.4.3), the complex power $\bar{S}_S$ delivered by the supply inverter, the apparent power A_I of the supply inverter and real power P_L absorbed by the load can be calculated as

$$\bar{S}_S = \bar{V}_S \bar{I}_T^* = \frac{|\bar{V}_S|^2}{|\dot{Z}_T \dot{Z}_R + \omega^2 M^2|^2} . \dot{Z}_R^* . \left(\dot{Z}_T \dot{Z}_R + \omega^2 M^2\right) \tag{2.4.4}$$

$$A_I = \frac{|\bar{V}_S|^2 |\dot{Z}_R|}{|\dot{Z}_T \dot{Z}_R + \omega^2 M^2|} \tag{2.4.5}$$

$$P_L = R_L |\bar{I}_R|^2 = \frac{R_L |\bar{V}_S|^2 \omega^2 M^2}{|\dot{Z}_T \dot{Z}_R + \omega^2 M^2|^2} = Re(\bar{S}_S) \tag{2.4.6}$$

Efficiency (η) and supply inverter power sizing factor (SIPSF) of IPT system for Fig. 2.3.3 can be defined as in (2.4.7)

$$\begin{cases} \eta = \frac{P_L}{P_S} \\ SIPSF = \frac{A_I}{P_L} \end{cases} \tag{2.4.7}$$

Here P_S is the real power delivered by the supply inverter. Significance of the efficiency is an index of the power lost in the power transfer process whilst the power sizing factor of supply inverter is an index of the sizing power of the voltage source for a given power absorbed by the load. They are calculated in (2.4.8) and (2.4.9) as

$$\eta = \frac{\omega^2 M^2 R_L}{|\dot{Z}_R|^2 r_S + \omega^2 M^2 R_L} \tag{2.4.8}$$

$$SIPSF = \frac{|\dot{Z}_R| |\dot{Z}_R \dot{Z}_T + \omega^2 M^2|}{\omega^2 M^2 R_L} \tag{2.4.9}$$

It is clear from (2.4.8) and (2.4.9) that reduction of $|\dot{Z}_T|$ is favorable for supply inverter power sizing factor and reduction of $|\dot{Z}_R|$ is favorable for both supply inverter power sizing factor and efficiency. This is possible if both the stages of IPT system are compensated by

inserting a capacitor resonating with their respective inductors. Based upon the series or parallel connection of resonating capacitor with inductor there are four basic resonant

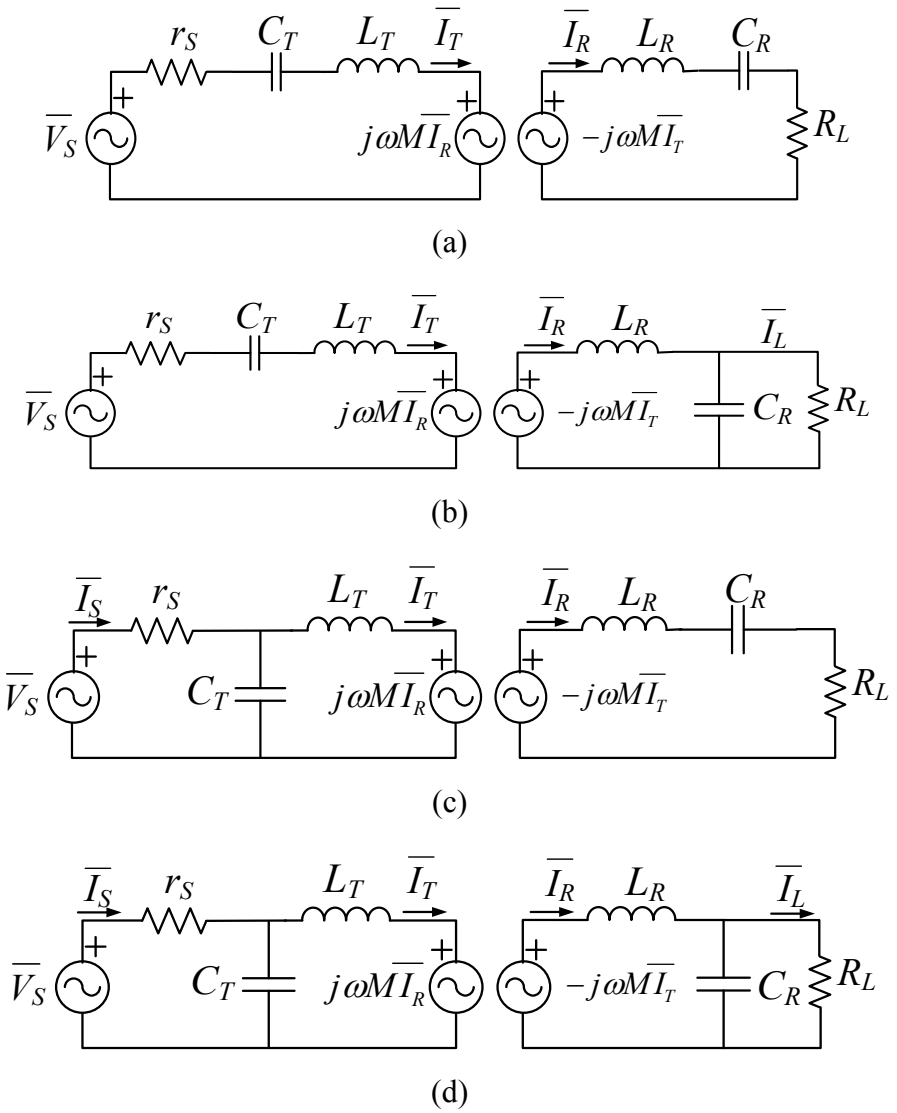

Fig. 2.4.2 IPT system with (a) SS, (b) SP, (c) PS and (d) PP resonant topologies.

topologies for IPTS. As shown in Fig. 2.3.1 they are SS (Series-Series), SP (Series- Parallel), PS (Parallel- Series) and PP (Parallel- Parallel) resonant IPTS [10], [11]. Taking example of SS topology as shown in Fig. 2.4.2(a), resonating capacitors are in series with inductors and are selected in order to compensate the self-inductances of the coils at chosen frequency ω. At resonance it can be given that

$$\begin{aligned} \omega^2 C_T &= \frac{1}{L_T} \\ \omega^2 C_R &= \frac{1}{L_R} \end{aligned} \tag{2.4.10}$$

Impedances of transmitting and receiving stages are now

$$\dot{Z_T} = r_S + j\left(\omega L_T - \frac{1}{\omega C_T}\right) \tag{2.4.11}$$

$$\dot{Z}_R = R_L + j\left(\omega L_R - \frac{1}{\omega C_R}\right) \tag{2.4.12}$$

which by using (2.4.10) takes the form of

$$\begin{aligned} \dot{Z}_T &= r_S \\ \dot{Z}_R &= R_L \end{aligned} \tag{2.4.13}$$

and efficiency and supply inverter power sizing factor result for SS into

$$\eta_{res} = \frac{\omega^2 M^2}{\omega^2 M^2 + R_L r_S} \tag{2.4.14}$$

$$SIPSF_{res} = \frac{\omega^2 M^2 + R_L r_S}{\omega^2 M^2} \tag{2.4.15}$$

Above finding in (2.4.14) and (2.4.15) confirms that resonance in both stages of IPTS makes it more convenient by improving efficiency and lowering the supply inverter power sizing factor.

2.5 Wireless charging of Electric Vehicles (EVs)

A typical resonant IPT system which further will be considered as the wireless battery charger (WBC) system consists of two physically detached subsystems with power transfer through induction. The system supplying the power is stationary and is named the transmitter. The system receiving the power is attached to vehicle and is named the receiver. The power is transferred via induction between two magnetically coupled coils, much like in a transformer. The coupling medium between the coils is air, which has a much higher magnetic reluctance than the ferromagnetic materials used in transformers. General scheme of WBC system is shown in Fig. 2.5.1 where grid is power supplier for entire WBC system. In order to achieve high efficiency and small size of component, frequency of transmitter current should be high. SAE, in its guideline TIR J2954, fixed the supply frequency of wireless battery chargers (WBC) in the range of 81.39-90 kHz. There are two well-known approach to achieve high frequency transmitting current for WBC system as linear amplifier and switch mode power converters. Linear amplifier suffers from high power loss and is applicable where efficiency is not so important. While, switch mode power converter have high efficiency makes it suitable for WBC application. Based on the input source of switch mode power supply it can be divided into DC-AC inverters and direct AC-AC converter. At present most of the power converter used for WBC system are three stage i.e. AC-DC-AC rectifier. In order to obtain DC power source from grid supply with high power factor, PWM rectifier are used. For high-frequency inverter phase shift control technique is used instead of PWM technique due to the

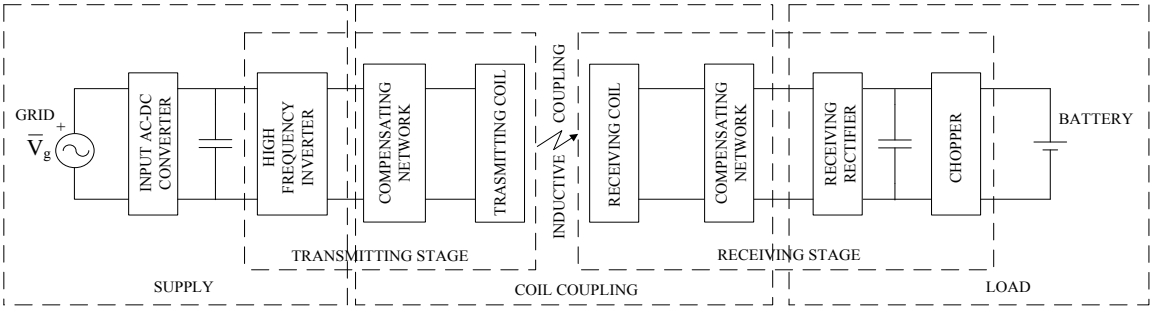

Fig. 2.5.1 WBC scheme.

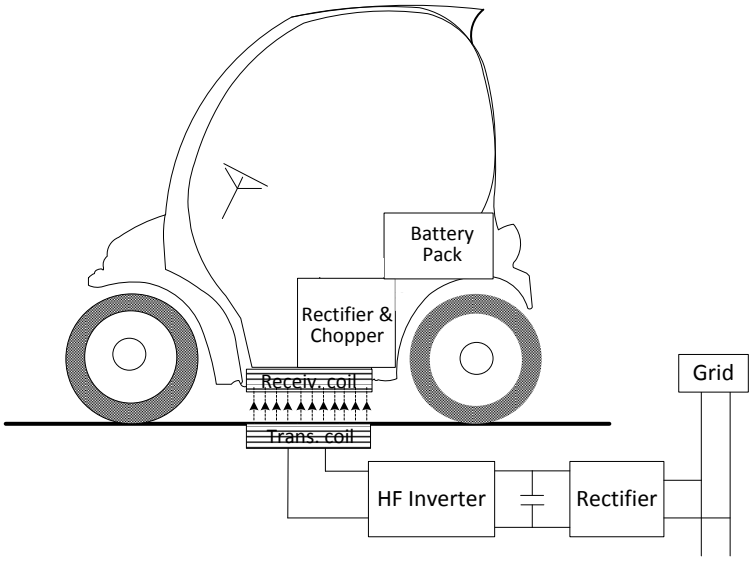

Fig. 2.6.1 Wireless static EV charging

fact that PWM switching frequency will become very high (more than 85 kHz) which is too high for the available switches [12].

At the receiver stage, diode rectifier is used to convert high-frequency input voltage to DC voltage cascaded with buck chopper which converts fixed DC input voltage to variable DC output voltage. Based on the state of vehicle during charging it can be classified as static and dynamic EV charging [13]. If vehicle is stationary during charging known as static charging and if moving on the charging track situated in the road known as dynamic charging of EV.

2.6 Wireless static charging of EV

Such scheme of EV charging is most appropriate for the situation where vehicle is stationary, for example while parking, at bus stop and other similar situation. Arrangement of stationary charging is shown in Fig. 2.6.1 where a transmitting pad is buried in the ground and receiving pad is mounted on the underside of the vehicle. Sometime primary pad is elevated by several centimeters in order to reduce the vertical distance between the coils. An automatic guidance system to help the driver is provided in the vehicle for better alignment of vehicle respect to primary charging of pad. The charging station and vehicle exchange the data either using inductive link or other short-range communication methods. With this feature it becomes very easy for charging station to adjust the charging procedure according to the condition of the battery or the driver's preferences.

2.7 Wireless dynamic charging of EV

Apart from offering great advantages, static wireless charging has still some limitations like size, volume and cost due to presence of large battery. It was suggested by some researchers to charge EV while moving on track as shown in Fig. 2.7.1. Dynamic wireless charging eliminates partially or completely the overnight charging through a compact network of dynamic chargers installed on the track capable to maintain the battery charged which, on consequence, reduces the range anxiety. Dynamic charging helps to lower the cost of EV by

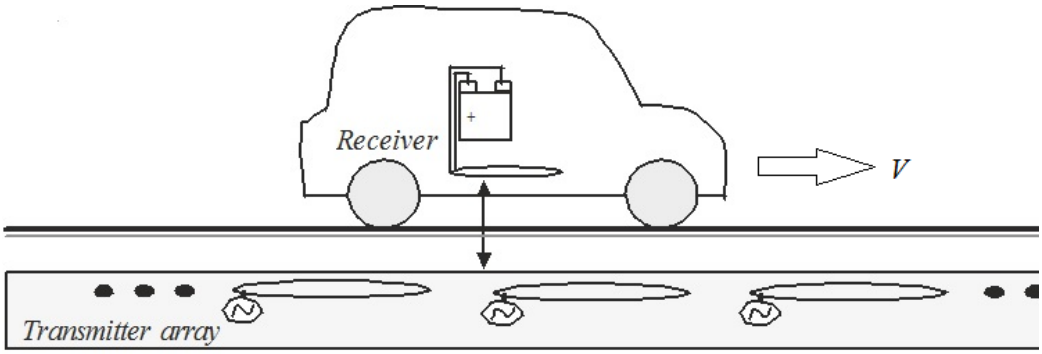

Fig. 2.7.1 Wireless dynamic EV charging

reducing the size of battery pack. Indeed, it does not need any battery pack support if it is always supplied by charging pads.

2.8 Conclusions

Starting with importance of wireless charging over conventional wired charging of EV this chapter discusses three different technologies to make this idea real. Three main techniques i.e. electric, magnetic and electromagnetic radiation for wireless power transfer can be used. For EV charging magnetic WPT technique is found to be most promising. A brief introduction and working principle of IPTS is discussed along with necessity of resonant technology and its advantages in terms of efficiency and power source power sizing factor. A general structure of WBC system is discussed, the chapter concludes with a brief introduction about static and dynamic charging of EV.

2.9 References:

[1] Greene, D. L., 1997, Survey Evidence on the Importance of Fuel Availability to Choice of alternative Fuels and Vehicles, Oak Ridge National Laboratory, Tennessee.

[2] Potoglou, D. & Kanaroglou, P. S., 2007, Household Demand and Willingness to Pay for Clean Vehicles, in Transportation Research Part D: Transport and Environment, vol. 12, no. 4. 264-274.

[3] L. Collins, “Cutting the Cord,” Engineering & Technology, vol. 2, no. 6, pp. 30-33, June 2007.

[4] S. Lukic and Z. Pantic, “Cutting the Cord: Static and Dynamic Inductive Wireless Charging of Electric Vehicles,” *IEEE Electrification Magazine*, vol. 1, no. 1, pp. 57-64, Sept. 2013.

[5] F. Musavi, W. Eberle, “Overview of wireless power transfer technologies for electric vehicle battery charging”, IET Power Electronics, vol.7, no.1, pp.60-66, Jan. 2014.

[6] Chun Qiu, K.T. Chau, Chunhua Liu, C.C. Chan, “Overview of Wireless Power Transfer for Electric Vehicle Charging”, Intern. Battery, Hybrid and Fuel Cell EV Symp, pp.1-9,Oct. 2013

[7] L. Collins, “Cutting the Cord,” Engineering & Technology, vol. 2, no. 6, pp. 30-33, June 2007.

[8] S. A. Sabki and N. M. L. Tan, “Wireless power transfer for electric vehicle,” in Proc. IEEE Power Engineering and Optimization Conference (PEOCO), 2014, pp. 41-46.

[9] T. Franke, I. Neumann, F. Bühler, P. Cocron and J. F. Krems, “Experiencing Range in an Electric Vehicle -Understanding Psychological Barriers”, available: www.researchgate.net.

[10] S. Chopra, and P. Bauer, “Analysis and design considerations for a contactless power transfer system,” in Proc. IEEE INTELEC, pp. 1–6, 9–13 Oct. 2011.

[11] C. Wang, G.A. Covic, and O.H. Stielau, “Power transfer capability and bifurcation phenomena of loosely coupled inductive power transfer systems*,” IEEE Trans. on Ind. Electron.*, vol. 51, no. 1, pp. 148–157, Feb. 2004.

[12] G. Buja, M. Bertoluzzo, and K.N. Mude, “Design and Experimentation of WPT Charger for Electric City-Car”, *IEEE Transaction on Industrial Electronics*, vol. 62, no. 62, pp. 7436 – 7447, Dec. 2015.

[13] S. Lukic and Z. Pantic, “Cutting the Cord: Static and Dynamic Inductive Wireless Charging of Electric Vehicles,” *Magazine in IEEE Electrification* vol. 1, no. 1, pp. 57-64, Sept. 2013.

Chapter 3

Efficiency and power sizing of SS, SP, PS and PP topology

3.1 Introduction

In the first generation of WBC the charging means was Inductive Power Transfer (IPT) scheme having drawbacks of low efficiency and high power supply sizing factor [1][2] which motivated researchers towards resonant technique by greatly mitigating all such demerits associated with it [3] [4]. Based on the placement of resonating capacitors four combination of LC connection are possible which can be divided into two arrangement i) transmitting capacitor in series while receiving capacitor is in either series or in parallel, giving rise to SS and SP topologies [5][6].ii) transmitting capacitor in parallel while receiving capacitor is in either series or in parallel, giving rise to PS and PP topologies [7][8].

In several studies, it has been found that, i) for unity input power factor, transmitting capacitor for SS topology is independent of the load and magnetic coupling coefficient k, while for SP it depends upon k only and for PS and PP it depends upon both [9], [10], ii) in terms of coupling coil set fabrication cost, SS and SP are economical than PS and PP, especially for high power application [11], iii) SS has highest misalignment tolerance while it reduces with SP, PS and PP respectively, iv) PS and PP are safe for the source in the absence of receiving side but are unable to transfer rated power if coils are not perfectly aligned whereas SS and SP are able to transfer power above the rated value during misalignment but with an unsafe behavior for the source [12], v) for SS and SP, a voltage source converter could be connected directly to the coil while an inductor is inserted to change the converter to a current source for PS and PP [13], vi) SS and SP have inherent capability to manage receiver short-circuit by adjusting the supply voltage, vii) considering no parasitic resistance, unity input power factor and constant the supply voltage, SS has load independent output current while SP has output voltage constant, however keeping transmitting current constant, SS has load independent output voltage and, SP has load independent output current [14], viii) SS exhibits higher efficiency than the SP in all the useful range of the charging power and that, at the same time, it necessitates much lower power sizing for both the power source and the coil coupling set [15].

This chapter compares the SS, SP, PS and PP topologies from the point of view of efficiency during entire battery charging profile, supply inverter power sizing factor (SIPSF) and coil coupling set power sizing factor (CCPSF). It also includes their behavior under the extreme condition of open and short circuit of the receiver

3.2 Battery charging profile

There are two modes of battery charging profile as shown in Fig. 3.2.1, one is constant current (CC) charging mode and another one is constant voltage (CV) charging mode [12].

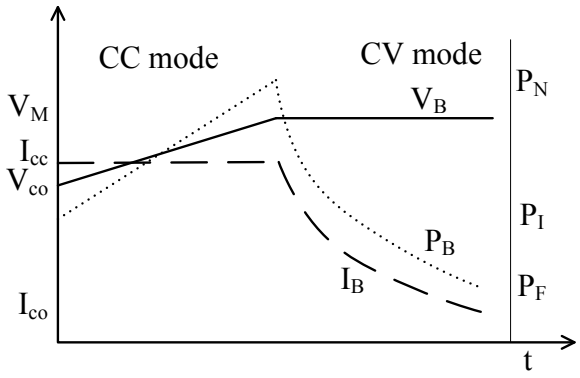

Fig. 3.2.1. Battery charging: normalized profiles of voltage (solid line), current (dashed line), and power (dotted line).

During CC mode, battery current I_B is constant at I_{CC} while, battery voltage V_B increases linearly from its cut-off voltage V_{CO} to its maximum value V_M. Power absorbed by the battery follows the product of I_B and V_B starting from P_I to its maximum at the border of two modes having corresponding value as P_N designated as its nominal value. During CV mode, V_B is kept constant to V_M and battery current decreases from I_{CC} to its cut-off value I_{CO} while, power decreases to P_F at the end of this mode.

3.3 WBC basics

The scheme of principle of a WBC is shown in Fig. 3.3.1, and consists of the power supply, the two coupled coils, and the load, where the latter one includes the EV battery. In the figure, the inductances of the transmitter and receiver coils are denoted with L_T and L_R respectively, and their parasitic resistances with r_T and r_R. As explicated below, currents through the coils are nearly sinusoidal. Then, the voltages induced in the transmitter and receiver coils can be assumed to be sinusoidal and expressed as

$$\begin{aligned} \bar{V}_T &= j\omega M \bar{I}_R \\ \bar{V}_R &= -j\omega M \bar{I}_T \end{aligned} \tag{3.3.1}$$

Because of the high quality factor (one hundred and more) of the coils, the parasitic resistances affect currents and voltages of the scheme only marginally. Therefore, to simplify the analysis, r_T and r_R are disregarded in determining voltage and current of the circuit and in evaluating its sizing powers; of course, they are taken into account in the calculation of the efficiency and, when needed, in the analysis of the extreme operating conditions.

3.4 Compensation types

3.4.1 Resonant transmitter

The circuital schemes of the transmitter of WBC with series and parallel resonance are shown in Figs.3.4.1 (a) and (b), respectively. In both the schemes, the resonance capacitor is denoted with C_T.

In WBC with series resonance of the transmitter, the power supply is a controlled voltage source, obtained by means of a front-end rectifier cascaded by a square-wave, high-frequency voltage inverter whose output voltage magnitude can be controlled by the phase shift technique or by adjusting the DC voltage at the inverter input. Since the series-resonant LC circuit abates the high-order harmonics of current at the inverter output almost entirely, only the fundamental component of current, denoted with $\bar{I}_S$, flows in the transmitter coil, thus justifying the second of (3.3.1). An equal sinusoidal-like behavior of the receiver justifies the first of (3.3.1). Further to the sinusoidal waveform of $\bar{I}_S$, only the fundamental component of the voltage supply, denoted with $\bar{V}_S$ in Fig. 3.4.1 (a), participates in the net power flow toward the receiver.

WBC with parallel resonance of the transmitter in Fig. 3.4.1 (b) is the dual version of the scheme in Fig. 3.4.1 (a). Due to the parallel-resonant LC circuit, current $\bar{I}_T$ is composed almost entirely by a fundamental component. This circumstance and the equal sinusoidal-like behavior of the receiver justify (3.3.1) also for this resonance. Furthermore, this gives rise to a sinusoidal voltage $\bar{V}_{Tt}$ across the transmitter coil. Since $\bar{V}_{Tt}$ coincides with the inverter output voltage, only the fundamental component of the supply current, denoted again with $\bar{I}_S$, participates in the net power flow toward the receiver.

For both the types of resonance, voltage $\bar{V}_{Tt}$ is expressed as

$$\bar{V}_{Tt} = j\omega L_T \bar{I}_T + \bar{V}_T \tag{3.4.1}$$

3.4.2 Series resonant receiver

The circuital scheme of the receiver of WBC with series resonance is shown in Fig. 3.4.2(a). The receiver coil forces current $\bar{I}_{L,S}$ into resonant capacitor C_R and, then, into the load, constituted by the cascade of a diode rectifier, DC bus capacitor C_{DC}, a chopper and the EV battery. DC component I_{DC} of the current at the diode rectifier output is equal to the average value of the rectified current. Let i) the voltage drop across the rectifier be negligible, ii) capacitor C_{DC} be large enough to fully filter the harmonics of the rectified current, and iii) voltage V_{DC} across capacitor C_{DC} be regulated at a constant value. It follows that the current

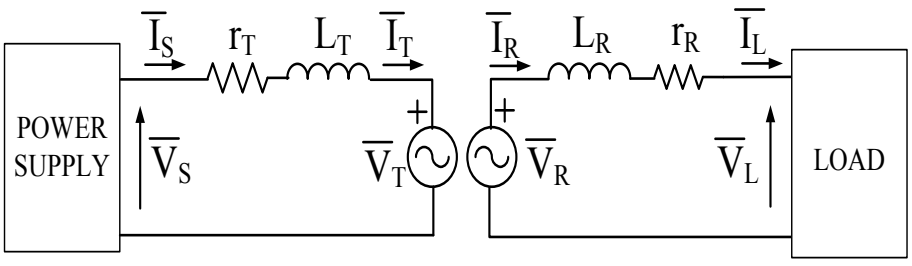

Fig. 3.3.1. Basic WBC scheme

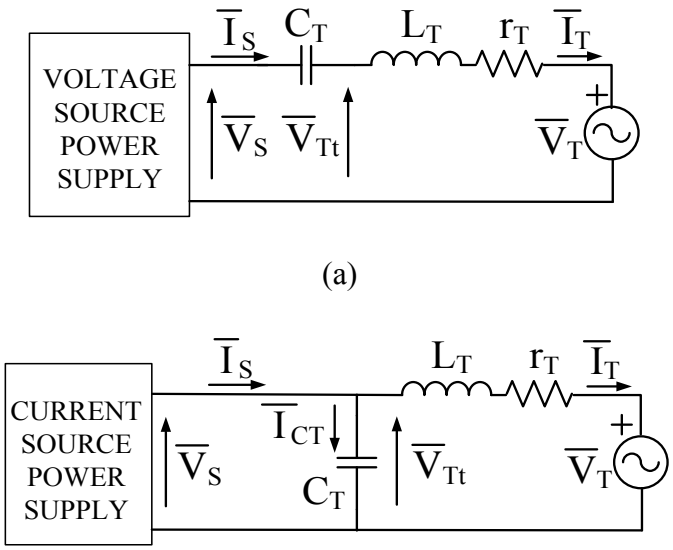

Fig. 3.4.1. Transmitter scheme with (a) series and (b) parallel resonance.

entering into the chopper is I_{DC}, and voltage at the rectifier input has a square waveform of magnitude V_{DC}.

Due to the filtering action of the series LC circuit, current $\overline{I}_{L,S}$ entering into the diode rectifier is sinusoidal so that only the fundamental component of the rectifier input voltage denoted with $\overline{V}_{L,S}$ in Fig. 3.4.2(a), contributes to the net power flow toward the battery. Since the commutations of the diode rectifier are driven by current $\overline{I}_{L,S}$, voltage $\overline{V}_{L,S}$ is in phase to $\overline{I}_{L,S}$

The relationships between the rms and DC values of voltages and currents at the diode rectifier input and output are

$$V_{L,S} = \frac{1}{\sqrt{2}}\frac{4}{\pi}V_{DC} \tag{3.4.2}$$

$$I_{L,S} = \frac{1}{\sqrt{2}}\frac{\pi}{2}I_{DC} \tag{3.4.3}$$

Being these quantities strictly related to the power injected into the battery, all the

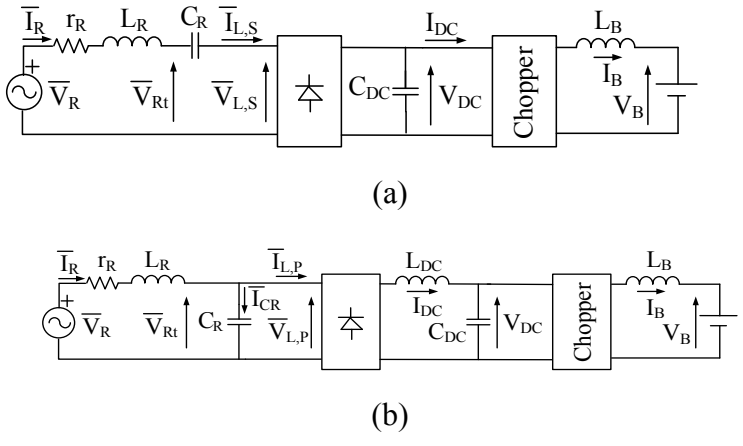

Fig. 3.4.2. Receiver scheme with (a) series and (b) parallel resonance.

voltages and currents that characterize the operation of WBC are conveniently formulated in terms of $\bar{V}_{L,S}$ and $\bar{I}_{L,S}$.

Because of the series connection of L_R and C_R in the receiver, it is

$$\bar{I}_R = \bar{I}_{L,S} \tag{3.4.4}$$

whilst, due to the L_R,C_R resonance, it is

$$\bar{V}_R = \bar{V}_{L,S} \tag{3.4.5}$$

From (3.4.4) and (3.4.5), and using the identity $1/\omega C_R=\omega L_R$, the voltage across the receiver coil can be written as

$$\bar{V}_{Rt} = \bar{V}_{L,S} - j\omega L_R \bar{I}_{L,S} \tag{3.4.6}$$

The voltage induced in the transmitter coil and the current flowing through it are found from (3.3.1), (3.4.4) and (3.4.5). They are

$$\bar{V}_T = j\omega M \bar{I}_{L,S} \tag{3.4.7}$$

$$\bar{I}_T = -\frac{\bar{V}_{L,S}}{j\omega M} \tag{3.4.8}$$

By substituting (3.4.7) and (3.4.8) into (3.4.1), the voltage across the transmitter coil can be expressed as

$$\bar{V}_{Tt} = -\frac{L_T}{M}\bar{V}_{L,S} + j\omega M \bar{I}_{L,S} \tag{3.4.9}$$

3.4.3 Parallel resonant receiver

The circuital scheme of the receiver of WBC with parallel resonance is shown in Fig. 3.4.2 (b). Here the receiver coil forces voltage $\bar{V}_{L,P}$ across the load. Then, the DC component V_{DC} of the voltage at the diode rectifier output is given by the average value of the rectified voltage. Let i) the voltage drop across the rectifier be negligible, ii) DC bus inductor L_{DC} be large enough to fully filter the harmonics of the rectified voltage, and iii) the voltage across capacitor C_{DC} be regulated at a constant value. It follows that current I_{DC} upstream capacitor C_{DC} has a DC waveform and current at the rectifier input has a square waveform of magnitude I_{DC}. Moreover, it follows that the voltage across capacitor C_{DC} is equal to V_{DC}. Due to the filtering action of the parallel L_R,C_R circuit, voltage $\bar{V}_{L,P}$ applied to the diode rectifier input is sinusoidal so that only the fundamental component of current at the rectifier. input, denoted with $\bar{I}_{L,P}$ in Fig. 3.4.2 (b), contributes to the net power flow toward the battery. Since here the commutations of the diode rectifier are driven by voltage $\bar{V}_{L,P}$, current $\bar{I}_{L,P}$ is in phase to $\bar{V}_{L,P}$. The relationships between the rms and DC values of voltages and currents at the diode rectifier input and output are

$$V_{L,P} = \frac{1}{\sqrt{2}}\frac{\pi}{2}V_{DC} \tag{3.4.10}$$

$$I_{L,P} = \frac{1}{\sqrt{2}}\frac{4}{\pi}I_{DC} \tag{3.4.11}$$

From Fig. 3.4.2 (b), it can be recognized that the receiver coil is flowed by the current

$$\bar{I}_R = \bar{I}_{L,P} + \bar{I}_{C_R} = \bar{I}_{L,P} + j\frac{\bar{V}_{L,P}}{\omega L_R} \tag{3.4.12}$$

and is subjected to a voltage of

$$\bar{V}_{Rt} = \bar{V}_{L,P} \tag{3.4.13}$$

while the voltage induced in it is equal to

$$\bar{V}_R = j\omega L_R \bar{I}_R + \bar{V}_{L,P} \tag{3.4.14}$$

Substitution of (3.4.12) into (3.4.14) leads to the following alternative expression of $\bar{V}_R$:

$$\bar{V}_R = j\omega L_R \bar{I}_{L,P} \tag{3.4.15}$$

The voltage induced in the transmitter coil and the current flowing through it are found from (3.4.12), (3.4.15) and (3.3.1). They are

$$\bar{V}_T = j\omega M \left(\bar{I}_{L,P} + j \frac{\bar{V}_{L,P}}{\omega L_R} \right) \tag{3.4.16}$$

$$\bar{I}_T = -\frac{L_R}{M} \bar{I}_{L,P} \tag{3.4.17}$$

By substituting (3.4.16) and (3.4.17) into (3.4.1), the voltage across the transmitter coil can be expressed as

$$V_{Tt} = j\omega M \left(\frac{k^2 - 1}{k^2} \right) \bar{I}_{L,P} - \frac{M}{L_R} \bar{V}_{L,P} \tag{3.4.18}$$

where

$$k \triangleq \frac{M}{\sqrt{L_T L_R}} \tag{3.4.19}$$

is the coil coupling coefficient.

3.4.4 Load voltage and current

The chopper in Figs. 3.4.2 (a) and (b) adjusts its output voltage to control the current I_B into the EV battery according to the required charging profile. Power P_B drawn from the battery is $V_B I_B$, where V_B is the battery voltage. Being V_{DC} constant, by (3.4.2) and (3.4.10), $V_{L,S}$ and $V_{L,P}$ are constant too. If the losses of the chopper are neglected, the following equalities hold

$$P_B = V_{DC} I_{DC} = V_{L,S} I_{L,S} = V_{L,P} I_{L,P} \tag{3.4.20}$$

The maximum value of P_B defines the nominal power P_N of WBC. In correspondence to P_N, I_{DC} gets its maximum value and, by (3.4.3) and (3.4.11), the same happens for $I_{L,S}$ and $I_{L,P}$. Further to this, it comes out that

$$max\left[I_{L,S}\right] = \frac{P_N}{V_{L,S}} \tag{3.4.21}$$

$$max\left[I_{L,P}\right] = \frac{P_N}{V_{L,P}} \tag{3.4.22}$$

where here and later on the operand max[·] stands for the maximum of its argument along the battery charging process. Eqs. (3.4.21) and (3.4.22) outline that the maximum load current depends on the resonant topology of the receiver whilst it does not depend on that of the transmitter. Something similar occurs for current and voltage of the transmitter coil: (3.4.7)-(3.4.9) and (3.4.16)-(3.4.18) depend on the resonant topology of the receiver through the load current and voltage but do not depend on that of the transmitter.

3.5 Performance indexes

WBC performance is investigated in terms of the following indexes: efficiency vs. power drawn from the EV battery, supply inverter power sizing factor (SIPSF), coil set power sizing factor (CSPSF), and circuitry behavior in extreme WBC operating conditions. Further to the results in the previous Section, the indexes are calculated by accounting only for the fundamental component of the involved AC voltages and currents.

Efficiency is defined as

$$\eta \triangleq \frac{P_B}{P_S} \tag{3.5.1}$$

being P_S the active power delivered by the supply inverter. Eq. (3.5.1) is conveniently rewritten in the form

$$\eta = \frac{P_B}{r_T {I_T}^2 + r_R {I_R}^2 + P_B} \tag{3.5.2}$$

where the Joule losses in parasitic resistances r_T and r_R are made explicit. Power sizing factors of the supply inverter and coil set are defined respectively as

$$SIPSF \triangleq \frac{A_I}{P_N} \tag{3.5.3}$$

$$CCPSF \triangleq \frac{A_T + A_R}{P_N} \tag{3.5.4}$$

where A_I, A_T and A_R are the power sizings of the supply inverter, the transmitter coil and the receiver coil. They are expressed as

$$A_I = max[V_S]max[I_S] \tag{3.5.5}$$

$$A_T = max[V_{Tt}]max[I_T] \tag{3.5.6}$$

$$A_R = max[V_{Rt}]max[I_R] \tag{3.5.7}$$

Note that SIPSF and CSPSF are indicators of both cost and volume of WBC with respect to its nominal power. Extreme operating conditions occurring more frequently in WBC are short-circuit and opening of the receiver terminals, They correspond respectively to impose $V_{L,S}$ and $I_{L,S}$ to 0, and could happen because of i) a fault in either the diode rectifier or the chopper, and ii) a thoughtless disconnection of either the battery or the receiver.

3.6 WBC with series resonant receiver

3.6.1 SS topology

Efficiency

With the SS topology, the Joule losses in (3.5.2) are calculated by substituting I_T and I_R as derived from (3.4.8), and from (3.4.4) and (3.4.20). The resulting efficiency is

$$\eta_{SS} = \frac{P_B}{r_T \left(\frac{V_{L,S}}{\omega M}\right)^2 + r_R \left(\frac{P_B}{V_{L,S}}\right)^2 + P_B} \tag{3.6.1}$$

Maximum of η_{SS} is achieved for P_B in (3.6.2) and is given by (3.6.3)

$$P_{B,SS,max} = \frac{{V_{L,S}}^2}{\omega M} \sqrt{\frac{r_T}{r_R}} \tag{3.6.2}$$

$$\eta_{SS,max} = \frac{1}{1+\frac{2}{\omega M}\sqrt{r_T r_R}} \quad (3.6.3)$$

Power sizing factors

Because of the series-resonant connection of the transmitter, it is

$$\bar{V}_S = \bar{V}_T \quad (3.6.4)$$

$$\bar{I}_S = \bar{I}_T \quad (3.6.5)$$

where $\bar{V}_T$ and $\bar{I}_T$ are given by (3.4.7) and (3.4.8), respectively. Consequently, power sizing term AI in (3.5.5) is equal to

$$A_{I,SS} = P_N \quad (3.6.6)$$

and, by (3.5.3), SIPSF is

$$SIPSF_{SS} = 1 \quad (3.6.7)$$

By (3.4.8) and (3.4.9), power sizing term A_T in (3.5.6) is expressed as

$$A_{T,SS} = P_N\sqrt{1+\left(\frac{L_T}{\omega M^2 P_N}{V_{L,S}}^2\right)^2} \quad (3.6.8)$$

whilst power sizing term A_R in (3.5.7), as derived from (3.4.6) and (3.4.4), is expressed as

$$A_{R,SS} = P_N\sqrt{1+\left(\omega L_R P_N \frac{1}{{V_{L,S}}^2}\right)^2} \quad (3.6.9)$$

By (3.5.4), (3.6.8) and (3.6.9), CSPSF results in

$$CCPSF_{SS} = \sqrt{1+\left(\frac{L_T {V_{L,S}}^2}{\omega M^2 P_N}\right)^2} + \sqrt{1+\left(\frac{\omega L_R P_N}{{V_{L,S}}^2}\right)^2} \quad (3.6.10)$$

Extreme operating conditions

For $VL_{,S}$=0, equations (3.4.8) and (3.6.5) lead to

$$\bar{I}_T = \bar{I}_S = 0 \quad (3.6.11)$$

By the first of (3.3.1) and (3.6.4), $\bar{I}_R$ is given by

$$\bar{I}_R = \frac{\bar{V}_S}{j\omega M} \quad (3.6.12)$$

Eq. (3.6.12) outlines that the receiver short-circuit operation does not subject the WBC elements to excessive e solicitations. For $I_{L,S}$=0, it is I_R=0 because of (3.4.4). By (3.4.7), V_T=0 and the current $\bar{I}_T$, which is equal to $\bar{I}_S$, is limited only by r_T according to

$$\bar{I}_T = \frac{\bar{V}_S}{r_T} \quad (3.6.13)$$

Being r_T small, operation with open receiver requires an adequate protection to avoid an excessive current solicitation of the transmitter elements (inverter, capacitor and coil).

3.6.2 PS topology

Efficiency

Expressions (3.4.4) and (3.4.8) for $\bar{I}_R$ and $\bar{I}_T$ hold also with PS topology so that η_{PS}, $P_{B,PS,max}$ and $\eta_{PS,max}$ are given by (3.6.1), (3.6.2) and (3.6.3), respectively.

Power sizing factors

From Fig. 3.4.1(b), the supply current splits into two terms, namely $\bar{I}_T$ and $\bar{I}_{CT}$; using the identity $\omega C_T = 1/\omega L_T$, current $\bar{I}_{CT}$ is given by

$$\bar{I}_S = \bar{I}_T + \bar{I}_{C_T} = \bar{I}_T + j\frac{\bar{V}_S}{\omega L_T} \tag{3.6.14}$$

By substituting (3.4.8) and (3.4.9) in (3.6.14), the supply current can be expressed as

$$\bar{I}_S = -\frac{M}{L_T}\bar{I}_{L,S} \tag{3.6.15}$$

By (3.4.9) and (3.6.15), the power sizing of the supply inverter is

$$A_{I,PS} = P_N\sqrt{1+\left(\frac{\omega M^2 P_N}{L_T}\frac{1}{{V_{L,S}}^2}\right)^2} \tag{3.6.16}$$

and the relevant SIPSF is

$$SIPSF_{PS} = \sqrt{1+\left(\frac{\omega M^2 P_N}{L_T {V_{L,S}}^2}\right)^2} \tag{3.6.17}$$

Being voltage $\bar{V}_{Tt}$ across and current $\bar{I}_T$ through the transmitter coil equal to those of the SS topology, power sizing $A_{T,PS}$ of the transmitter coil is still given by (38). Since the circuitry at the receiver side is the same as with the SS topology, sizing power $A_{R,PS}$ of the receiver coil can be still found from (3.4.6) and (3.4.4), and is expressed again as (3.6.9). Consequently, $CSPSF_{PS}$ is equal to (3.6.10).

Extreme operating conditions

When $V_{L,S}=0$, it is

$$\bar{I}_T = 0 \tag{3.6.18}$$

similarly to what happens in the SS topology. From Fig. 3.4.1(b), when $\bar{I}_T=0$, it turns out that $\bar{V}_{Tt}$ is equal to $\bar{V}_T$. Then, by (3.6.14) and (3.6.18), voltage $\bar{V}_T$ is

$$\bar{V}_T = -j\omega L_T \bar{I}_S \tag{3.6.19}$$

and, by the first of (3.3.1), current $\bar{I}_R$ is

$$\bar{I}_R = -\frac{L_T}{M}\bar{I}_S \tag{3.6.20}$$

When $I_{L,S}=0$, $\bar{I}_R$ is equal to zero and, by (3.4.7), also $\bar{V}_T$ is equal to zero. Consequently, from the scheme of Fig. 3.4.1(b), voltage $\bar{V}_S$ is given by

$$\bar{V}_S = \frac{\frac{1}{j\omega C_T}(r_T + j\omega L_T)}{r_T}\bar{I}_S \cong \frac{(\omega L_T)^2}{r_T}\bar{I}_S \tag{3.6.21}$$

and gets a very high magnitude due to the small value of r_T. Eq. (3.6.21) shows that the PS topology, like the SS one, needs to be protected against operation with open receiver but, differently from the SS one, the protection is necessary to avoid an excessive voltage solicitation of the transmitter.

3.7 WBC with parallel resonant receiver

3.7.1 SP topology

Efficiency

With PS topology, the Joule losses are expressed using the currents given by (3.4.17) and (3.4.12) and the efficiency η_{SP} results in

$$\eta_{SP} = \frac{P_B}{r_T\left(\frac{L_R}{M}\frac{P_B}{V_{L,P}}\right)^2 + r_R\left[\left(\frac{P_B}{V_{L,P}}\right)^2 + \left(\frac{V_{L,P}}{\omega L_R}\right)^2\right] + P_B} \tag{3.7.1}$$

Maximum of η_{SP} is achieved for P_B in (3.7.2) and is given by (3.7.3)

$$P_{B,SP,max} = \frac{{V_{L,P}}^2}{\omega L_R}\sqrt{\frac{r_R}{r_T\left(\frac{L_R}{M}\right)^2 + r_R}} \tag{3.7.2}$$

$$\eta_{SP,max} = \frac{1}{1+\frac{2}{\omega M}\sqrt{r_R r_T + {r_R}^2\left(\frac{M}{L_R}\right)^2}} \tag{3.7.3}$$

Power sizing factors

The power sizing of the supply inverter in (3.5.5) is obtained by deriving V_S from (3.6.4) and (3.4.16), and I_S from (3.6.5) and (3.4.17). It is

$$A_{I,SP} = P_N\sqrt{1 + \left(\omega L_R P_N \frac{1}{{V_{L,P}}^2}\right)^2} \tag{3.7.4}$$

and the relevant SIPSF is

$$SIPSF_{SP} = \sqrt{1 + \left(\frac{\omega L_R P_N}{{V_{L,P}}^2}\right)^2} \tag{3.7.5}$$

By (3.4.17) and (3.4.18), the power sizing of the transmitter coil is expressed as

$$A_{T,SP} = P_N\sqrt{1 + \left[\omega L_R P_N \frac{1}{{V_{L,P}}^2}\left(\frac{1-k^2}{k^2}\right)\right]^2} \tag{3.7.6}$$

and, by (3.4.12) and (3.4.13), the power sizing of the receiver coil as

$$A_{R,SP} = P_N\sqrt{1 + \left(\frac{1}{\omega L_R P_N}{V_{L,P}}^2\right)^2} \tag{3.7.7}$$

The relevant CSPSF is then

$$CCPSF_{SP} = \sqrt{1 + \left[\frac{\omega L_R P_N}{{V_{L,P}}^2}\left(\frac{1-k^2}{k^2}\right)\right]^2} + \sqrt{1 + \left(\frac{{V_{L,P}}^2}{\omega L_R P_N}\right)^2} \tag{3.7.8}$$

Extreme operating conditions

When $V_{L,P}=0$, equation (3.4.12) points out that $\overline{I}_R$ is equal to $\overline{I}_{L,P}$. From (3.4.16) and (3.6.4), $\overline{I}_R$ is derived as

$$\bar{I}_R = \frac{\bar{V}_S}{j\omega M} \tag{3.7.9}$$

and, from (3.4.17), (3.6.5) and (3.7.9), $\bar{I}_T$ is derived as

$$\bar{I}_T = \frac{jL_R\bar{V}_S}{\omega M^2} \tag{3.7.10}$$

Eq. (3.7.10) emphasizes that, due to the small value of k, the transmitter coil is solicited by an unduly value of current.

When $I_{L,P}$=0, the receiver behaves as in the SS topology under the condition of $V_{L,S}$=0. Then, $\bar{I}_R$ is given by (3.6.12) whilst $\bar{I}_T$ is equal to 0. As a result, in the SP topology both short-circuit and opening of the receiver terminals do not subject the WBC elements to excessive solicitations.

3.7.2 PP topology

Efficiency

Efficiency η_{PP} is obtained by using the current expressions in (3.4.12) and (3.4.17) to calculate the Joule losses; the resulting expression of the efficiency is equal to that of η_{SP} in (3.7.1). The same occurs for the expression of $P_{B,PP,max}$, i.e. of power P_B that makes the efficiency maximum, and that of $\eta_{PP,max}$, i.e. of the maximum efficiency, which are again given by (3.7.2) and (3.7.3), respectively.

Power sizing factors

As for the PS topology, current $\bar{I}_S$ is the sum of the two terms in (3.6.14). The first term is equal to (3.4.17) whilst the second one is derived from (3.4.18) by observing, from the scheme in Fig. 3.4.1(b), that $\bar{V}_S$ is equal to $\bar{V}_{Tt}$. By manipulating (3.4.17), (3.4.18) and (3.6.14), current $\bar{I}_S$ can be expressed as

$$\bar{I}_S = -\frac{M}{L_T}\bar{I}_{L,P} + \frac{k^2}{j\omega M}\bar{V}_{L,P} \tag{3.7.11}$$

To obtain the expression of sizing power $A_{I,PP}$ of the supply inverter, max[V_S] and max [I_S] in (3.5.5) must be calculated. From (3.4.18) and (3.7.11), they are expressed as

$$max[V_S] = \frac{M}{L_R}V_{L,P}\sqrt{1 + \left(\frac{\omega L_R P_N}{{V_{L,P}}^2}\frac{k^2-1}{k^2}\right)^2} \tag{3.7.12}$$

$$max[I_S] = \frac{M}{L_T}\frac{P_N}{V_{L,P}}\sqrt{1 + \left(\frac{{V_{L,P}}^2}{\omega L_R P_N}\right)^2} \tag{3.7.13}$$

Then, $A_{I,PP}$ and the relevant $SIPSF_{PP}$ become

$$A_{I,PP} = k^2 P_N\sqrt{\left[1 + \left(\frac{\omega L_R P_N}{{V_{L,P}}^2}\frac{k^2-1}{k^2}\right)^2\right]\left[1 + \left(\frac{{V_{L,P}}^2}{\omega L_R P_N}\right)^2\right]} \tag{3.7.14}$$

$$SIPSF_{PP} = k^2\sqrt{\left\{1 + \left[\frac{\omega L_R(k^2-1)P_N}{k^2{V_{L,P}}^2}\right]^2\right\}\left[1 + \left(\frac{k^2 L_T {V_{L,P}}^2}{\omega M^2 P_N}\right)^2\right]} \tag{3.7.15}$$

Power sizing $A_{T,PP}$ of the transmitter coil is readily found by observing that $\bar{V}_{Tt}$ and $\bar{I}_T$ are the same as with the SP topology. Then, $A_{T,PP}$ is again expressed as in (3.7.6). On the other hand, power sizing $A_{R,PP}$ of the receiver coil is also again expressed as in (3.7.7). Consequently, $CSPSF_{PP}$ is equal to (3.7.8).

Extreme operating conditions

When $V_{L,P}=0$, $\bar{I}_R$ is equal to $\bar{I}_{L,P}$ as it happened in the SP topology. Current $\bar{I}_R$ can be written as a function of $\bar{I}_S$ by setting $\bar{V}_{L,P}=0$ in (3.7.11), i.e. it is

$$\bar{I}_R = -\frac{L_T}{M}\bar{I}_S \tag{3.7.16}$$

By (3.4.17), (3.4.18) and (3.7.16), $\bar{I}_T$ and $\bar{V}_S$ can be expressed as

$$\bar{I}_T = \frac{1}{k^2}\bar{I}_S \tag{3.7.17}$$

$$\bar{V}_S = j\omega L_T \frac{(1-k^2)}{k^2}\bar{I}_S \tag{3.7.18}$$

where (3.7.18) is obtained by reminding that $\bar{V}_S$ is equal to $\bar{V}_{Tt}$. Eqs. (3.7.17) and (3.7.18) emphasizes that, due to the small value of k, the transmitter is solicited by unduly values of both current and voltage.

When $I_{L,P}=0$, the receiver behaves as in the PS topology under the condition $V_{L,S}=0$. Then, $\bar{I}_R$ and $\bar{I}_T$ are still given by (3.6.20) and (3.6.18), respectively. As a result, the PP topology is self-protected against open-circuit receiver operation..

3.8 Performance comparison

Efficiency

As found in previous section, the efficiency and the sizing power of the coil set depend on the topology of the receiver whilst they are not affect by the topology of the transmitter, as summarized by the following equalities

$$\begin{array}{lll} \eta_{SS} = \eta_{PS} & A_{T,SS} = A_{T,PS} & A_{R,SS} = A_{R,PS} \\ \eta_{SP} = \eta_{PP} & A_{T,SP} = A_{T,PP} & A_{R,SP} = A_{R,PP} \end{array} \tag{3.8.1}$$

TABLE 3.1. BATTERY AND WBC SETUP CHARACTERISTICS

Data	Symbol	Value
DC bus voltages	V_{DC}	65 V
Nominal power	P_N	560 W
Trans. and rec. coils inductances	L_T, L_R	120 μH
Trans. and rec. coils parasitic resistances	r_T, r_R	0.5 Ω
Trans. and rec. resonant capacitances	C_T, C_R	29 nF
Coil mutual inductance	M	30 μH
Coupling coefficient	k	0.254
Supply angular frequency	ω	2π·85000 rad/s

Comparison of (3.6.3) with (3.7.3) underlines that, for given values of r_R and r_T, the SS and PS topologies have a maximum efficiency higher than the SP and PP topologies.

As an example, efficiencies of the four topologies have been computed using the parameters of Tab. 3.1, pertinent to a WBC setup available in the lab. The resultant efficiencies are plotted in Fig. 3.8.1 as a function of power P_B drawn from the battery; their maximum values are listed in the second column of Tab. 3.2. The plots of Fig. 3.8.1 and the data in Tab. 3.2 show that the topologies with the series-resonant receiver i) outperform those with the parallel-resonant receiver as soon as the transferred power exceeds 64 W, and ii) have a higher maximum efficiency even if, for the WBC setup in Tab. 8.1, the difference with respect to the other topologies is quite small.

Power sizing factors

Let the power sizing factors of the inverter supply be examined first. Comparison of (3.6.7) with (3.6.17) reveals that the SS topology has a lower SIPSF than the PS topology. This outcome is confirmed by the values reported in the sixth column of Tab.3.2.

Comparison of (3.6.17) and (3.7.5) reveals that the power sizing factors of the inverter supply of the PS and SP topologies have a similar expression. However, by entering (3.4.2) and (3.4.10) into (3.6.17) and (3.7.5), it descends that $SIPSF_{SP}$ is higher than $SIPSF_{PS}$, provided that

$$k < \frac{8}{\pi^2} \approx 0.81 \tag{3.8.2}$$

Condition (3.6.2) does not depend on the WBC parameters and is commonly satisfied because the coupling coefficient of most WBCs falls in the range of about 0.2-0.3. Then, SIPSF of the PS topology is lower than the corresponding factor of the SP topology.

Comparison of SIPSF between the SP and PP topologies, given in (3.7.5) and (3.7.15), is more involved; to this end, it is convenient to rewrite SIPSF of the PP topology in the form

$$SIPSF_{PP} = SIPSF_{Sp}\sqrt{\left[(k^2-1)^2 + \left(\frac{V_{L,P}^2}{\omega L_R P_N}k^2\right)^2\right]} \tag{3.8.3}$$

After some manipulations, it comes up that $SIPSF_{PP}$ is lower than $SIPSF_{SP}$, provided

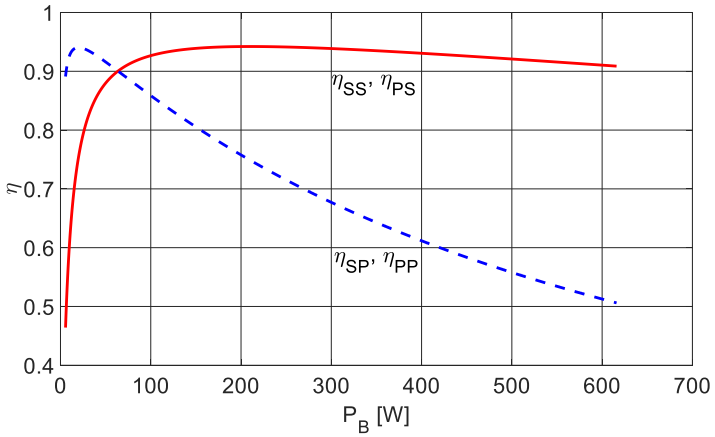

Fig. 3.8.1. Efficiency of the four topologies.

TABLE 3.2. TOPOLOGY PERFORMANCE

	η_{max}	A_I [VA]	A_T [VA]	A_R [VA]	SIPSF	CCPSF
SS	0.94	560	1000	5895	1	12.3
SP	0.94	3896	55913	566	6.9	100.8
PS	0.94	676	1000	5895	1.2	12.3
PP	0.94	3645	55913	566	6.5	100.8

that

$$k < \sqrt{\frac{2}{1+\left(\frac{{V_{L,P}}^2}{\omega L_R P_N}\right)^2}} \triangleq \alpha \qquad (3.8.4)$$

For the WBC setup in Tab. 3.1, α is about 1.4 and, hence, $SIPSF_{PP}$ is lower than $SIPSF_{SP}$.

Comparison of SIPSF between the PP and PS topologies, executed by a numerical analysis on the data in Tab. 3.1, discloses that $SIPSF_{PS}$ is lower than $SIPSF_{PP}$ as long as k is less than about 0.62.

Regarding the power sizing factors of the coil set, it follows directly from (3.8.1) that the SS and PS topologies have an equal CSPSF, and the same happens for the SP and PP topologies. For the data in Tab. 3.1, the factor of the former two topologies is of about eight times lower. A worth-to-note result in Tab. 3.2 is that the power sizing of the receiver coil prevails on that of the transmitter coil for the SS and PS topologies whilst the opposite occurs for the SP and PP topologies.

Regarding the extreme operating conditions, short-circuit of the receiver terminals is not critical for any topology while their opening causes an excessive solicitation in the WBC transmitter, which is of current for the SS topology and of voltage for the PS topology.

3.9 Experimental validation

3.9.1 WBC setup description

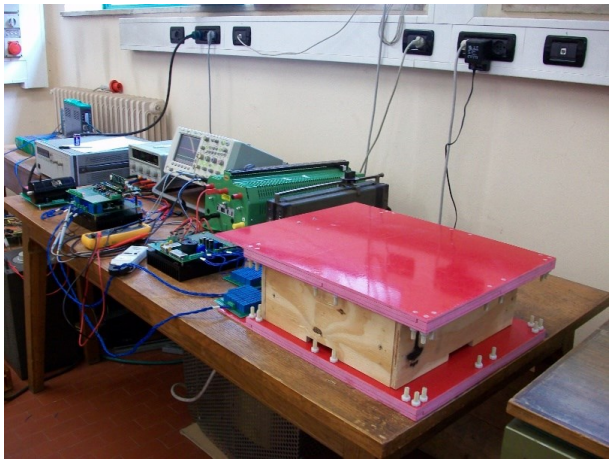

Fig. 3.9.1. Prototypal WBC.

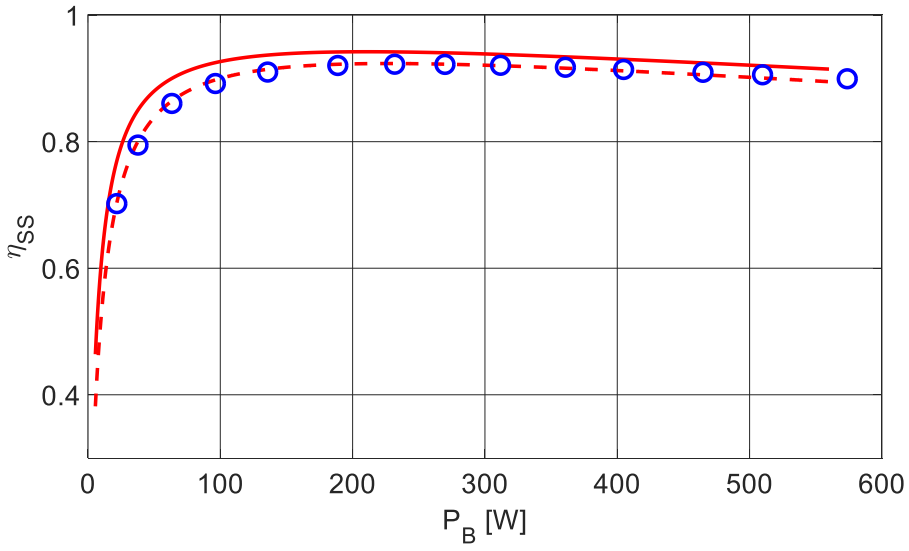

Fig. 3.9.2. Computed and measured efficiency.

The WBC setup with the data in Tab. 3.1 has been used to check the theoretical findings; it implements the SS topology and has been designed to charge the battery of a city-car. The transmitter coil is supplied by a square wave voltage source inverter whose DC input voltage is adjusted in order to control the magnitude of $\bar{V}_S$. The chopper feeding the battery has a buck topology, with VDC fixed at 65 V to comply with the maximum charging battery voltage of 56 V. A picture of the WBC setup is given in Fig. 3.9.1, the coils being enclosed in the two red plates.

3.9.2 Efficiency measurement

In order to expedite the tests, a variable resistor has been connected at the output of the chopper instead of the city-car battery and its value has been adjusted to emulate different charging conditions. Through the experiments, V_{DC} has been kept constant by adjusting the DC input voltage of the supply inverter. The power transferred from the transmitter to the receiver coil and the relevant efficiency have been measured by means of the WT1800 digital wattmeter of Yokogawa Co.

The collected efficiency data are reported with the blue circles in Fig. 3.9.4 as a function of the power drawn from the load resistor. By way of evaluation, efficiency η_{SS} computed using (3.6.1) is plotted with the solid red line. The plots show that the measured efficiency is a bit less than the computed one. The difference is due to the fact that the following resistances have been neglected in (3.6.1): i) the parasitic resistances of the capacitors, and ii) the resistances of the wires connecting coils, capacitors, supply inverter and diode rectifier. Their total contribution has been estimated in about 0.1 Ω and a new plot has been traced in Fig. 3.9.2 by computing η_{SS} with r_T and r_R updated to 0.6 Ω. The obtained plot, distinguished by the red dashed line, lies below the previous one and matches very well with the measurements.

3.9.3 Voltage/current measurement

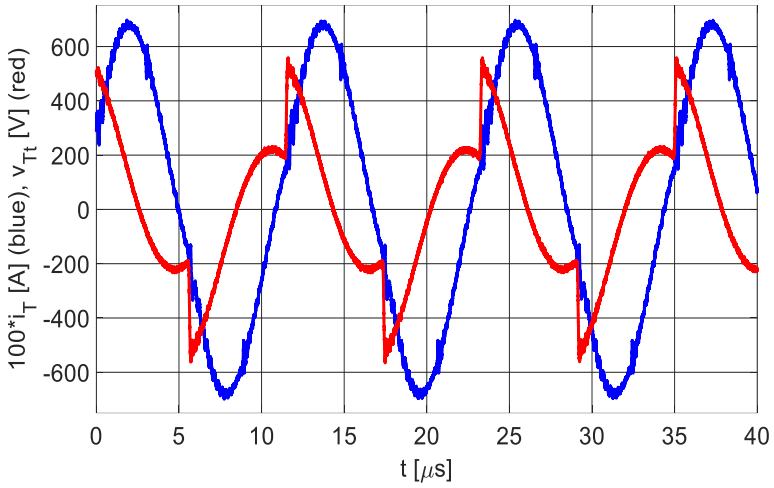

Fig. 3.9.3. Transmitter coil voltage (red) and current (blue).

Voltages and currents of the transmitter and receiver coils have been acquired by the TDS 5034 digital oscilloscope of Tektronix Co. The quantities relevant to transmitter coil are plotted in Fig. 3.9.3 while those relevant to the receiver coil are plotted in Fig. 3.9.4; all the quantities have been acquired with WBC operating at the nominal power. The figures show that, as anticipated above, the currents in the coils are nearly sinusoidal. Instead, the voltages across the coils exhibit a step that is originated by the square waveform respectively of the output voltage of the supply inverter and the input voltage of the diode rectifier. Magnitudes of the fundamental harmonic of voltages digital oscilloscope of Tektronix Co. The quantities relevant to transmitter coil are plotted in Fig. 3.9.3 while those relevant to the receiver coil are plotted in Fig. 3.9.4; all the quantities have been acquired with WBC operating at the nominal power. The figures show that, as anticipated above, the currents in the coils are nearly sinusoidal. Instead, the voltages across the coils exhibit a step that is originated by the square waveform respectively of the output voltage of the supply inverter and the input voltage of the diode rectifier. Magnitudes of the fundamental harmonic of voltages and currents, computed by applying the FFT algorithm to the samples acquired by the oscilloscope, have been used to work out the power sizing of the coils. The resulting values are reported in the first row of

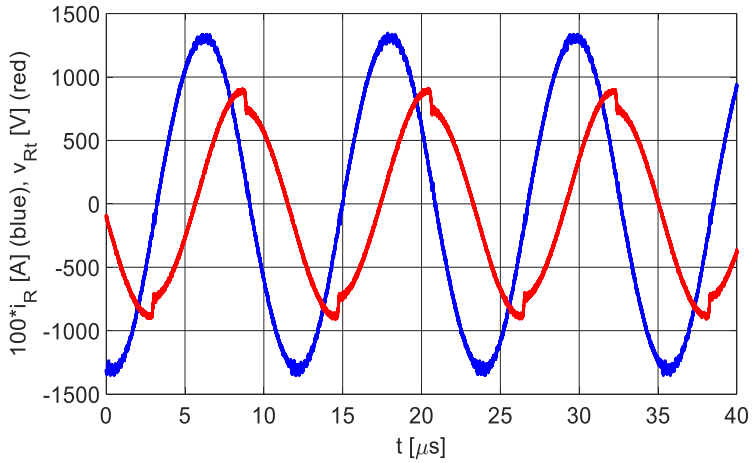

Fig. 3.9.4. Receiver coil voltage (red) and current (blue).

Table 3.3. SS TOPOLOGY COIL POWEER SIZING			
	A_T [VA]	A_R [VA]	CCPSF
From WBC setup	1174	5837	12.5
Recomputed	1147	5896	12.5

Tab. 3.3. Their comparison with the values listed in Tab. 3.2 emphasizes a good agreement for $A_{R,SS}$ and an appreciable deviation of about 17% for $A_{T,SS}$. As a first attempt, the deviation has been ascribed to the resistances of the circuitry. The hypothesis has been validated by means of a Matlab program, expressly drafted to compute the power sizing of the coils by taking into accounts the effects of the resistances. The recomputed values of the power sizing are reported in the second row of Tab. 3.3, and point out a good agreement also for $A_{T,SS}$. Moreover, the recomputed value of $A_{R,SS}$ changes very little with respect to that in Tab. 3.2. An explanation of these two outcomes is as follows: the analysis above has been executed with fixed values of the voltage across the DC bus of the receiver and the power drawn from the battery, which means for fixed magnitudes of both $\overline{V}_L$ and $\overline{I}_L$. Then, the resistances have a negligible effect on the power sizing of the receiver coil whilst their effect builds up going towards the transmitter coil.

3.10 Conclusions

The chapter has carried out a thorough analysis of the four one-element resonant topologies of WBCs. A number of significant findings has been derived; first of all, it has been shown that the WBC performance is substantially determined by the type of resonance of the receiver. Therefore, two classes of WBC topologies can be recognized, one with series-resonant receiver (SRR) and the other one with parallel-resonant receiver (PRR).

Drilling down and highlighting the merits of the two classes, the efficiency of the SRR class outperforms the efficiency of the PRR class over almost all the range of power drawn from the battery, being the efficiency of the SS topology a little higher. Also the power sizing factors of the supply inverter and of the coil set are broad in favor of the SRR class, being the power sizing factor of the supply inverter of the SS topology a little lower. Instead, the PRR class is robust against short-circuit and open operation of the receiver terminals whereas the SS topology sustains only their short-circuit operation, being the transmitter of the SS and PS topologies subjected respectively to overcurrent and to overvoltage under their open operation. Theoretical findings on the SS topology have been checked against measurements taken from a WBC setup, getting a close agreement between them.

3.11 References

[1] K.N.Mude, M.Bertoluzzo and G.Buja, “Design of contactless battery charger for electrical vehicle,” Proc. of IEEE International Conference of AFRICON 2013, 2013, pp.1091-1096.

[2] D.Ali and P.G.Khorasani “Design & simulation of a contactless power transmission system with maximum efficiency & soft switching realization of related inverter,” Proc. of. IEEE Int. Conference on Energy and Electrical Drives, 2009, pp. 43-48.

[3] B. Ni, C.Y. Chung, and H.L. Chan, “Design and comparison of parallel and series resonant topology in wireless power transfer,” in Proc. IEEE 8th Conference on Industrial Electronics and Applications (ICIEA), 2013, pp. 1832-1837.

[4] V. J. Brusamarello, Y. B. Blauth, R. Azambuja, and I. Muller, “A study on inductive power transfer with wireless tuning,” in Proc. IEEE IIMT, Graz, Austria, 2012, pp. 1098–1103.

[5] G. A. Covic and J. T. Boys, “Modern trends in inductive power transfer for transportation applications,” *IEEE J. Emerging Sel. Topics Power Electron*., vol. 1, no. 1, pp. 28–41, Mar. 2013.

[6] Z. Huang, S.C. Wong, and C.K. Tse, “Design methodology of a series-series inductive power transfer system for electric vehicle battery charger application,” in Proc. IEEE Energy Conversion Congress and Exposition (ECCE), 2014, pp. 1778-1782.

[7] W.Zhou and H.Ma, “Design considerations of compensation topologies in ICPT system,” Proc. of. IEEE Conf. on Applied Power Electronics, 2007, pp. 985-990.

[8] W. Zhou and H. Ma, “Design Considerations of Compensation Topologies in ICPT System,” in Proc. IEEE Applied Power Electronics Conference and Exposition, 2007, pp. 985-990.

[9] Chwei-Sen Wang, O.H. Stielau, and G.A. Covic, “Design considerations for a contactless electric vehicle battery charger,” IEEE Transactions on Industrial Electronics, vol. 52, no. 5, pp. 1308-1314, Oct. 2005.

[10] Y.H. Chao, J.J. Shieh, C.T. Pan, and W.C. Shen, “A Closed-form Oriented Compensator Analysis for Series-parallel Loosely Coupled Inductive Power Transfer Systems,” in Proc. of IEEE Power Electronics Specialists Conference, Orlando, FL, 2007, pp. 1215-1220.

[11] J. Sallan, J.L. Villa, A. Llombart, and J.F. Sanz, “Optimal Design of ICPT Systems Applied to Electric Vehicle Battery Charge,” IEEE Transactions on Industrial Electronics, vol. 56, no. 6, pp. 2140-2149, June 2009.

[12] J. L. Villa, J. Sallan, J. F. Sanz Osorio, and A. Llombart, “High-Misalignment Tolerant Compensation Topology For ICPT Systems,” IEEE Transactions on Industrial Electronics, vol. 59, no. 2, pp. 945-951, Feb. 2012.

[13] S. Li and C.C. Mi, “Wireless Power Transfer for Electric Vehicle Applications,” IEEE Journal of Emerging and Selected Topics in Power Electronics, vol. 3, no. 1, pp. 4-17, March 2015.

[14] K. Aditya and S.S. Williamson, “Comparative study of series-series and series-parallel compensation topologies for electric vehicle charging,” in Proc. of IEEE ISIE, 2014, pp. 426-430.

[15] R.K. Jha, S. Giacomuzzi, G. Buja, M. Bertoluzzo, and M. K. Naik, “Efficiency and power sizing of SS vs. SP topology for wireless battery chargers,” in Proc. of IEEE International Power Electronics and Motion Control Conference (PEMC), Varna, 2016, pp. 1014-1019.

Chapter 4

SS topology with and without chopper

4.1 Introduction

Based on the discussion of the last chapter, SS resonant topology it is found to be very promising for WBC. Schematic of WBC consists of transmitting and receiving stages where power conversion circuitry of receiver includes a diode rectifier to supply the load with a direct voltage and resorts to different solutions for the adjustment of the voltage amplitude: in [1] the series resonant coil is connected to a switch that controls the magnitude of the AC voltage before applying it to the diode rectifier; in [2] this approach is extended to a parallel resonant coil; in [3] the loading capability of the circuitry in [1] and [2] is improved by an additional resonant section, in [4] the diode rectifier is substituted for by a controlled rectifier. The most popular technique for WBC receiver charges the battery in a straightforward manner with the diode rectifier or through a chopper, and controls the voltage of the power source in the transmitter to adjust the power absorbed by the battery [5]. The two ways of charging the battery give rise to two WBC arrangements, hereafter denoted with #1 and #2 respectively. The first arrangement directly charges the EV battery by controlling the rectified current/voltage. The second arrangement charges the EV battery through a chopper whose input voltage is kept constant. This chapter compares these two charging arrangement in terms of efficiency, power transfer ratio and power sizing factor of both the supply inverter and the transmitter/receiver coils.

4.2 Battery charging

Battery charging profile as drawn in Fig. 3.2.1 is redrawn here as in Fig. 4.2.1where voltage, current, power and resistance profiles are normalized respectively to V_M, I_{CC}, P_N, and R_N, where V_M is the maximum battery voltage, I_{CC} is the charging current in CC mode, P_N is the nominal charging power, reached at point N and given by the product of V_M by I_{CC}, and R_N is the battery resistance at point N, given by V_M/I_{CC}.

As a function of P_B, resistance R_B is expressed in CC and CV zones respectively as

$$R_B = \frac{1}{I_{CC}^2} P_B,\ R_B = V_M^2 \frac{1}{P_B} \tag{4.2.1}$$

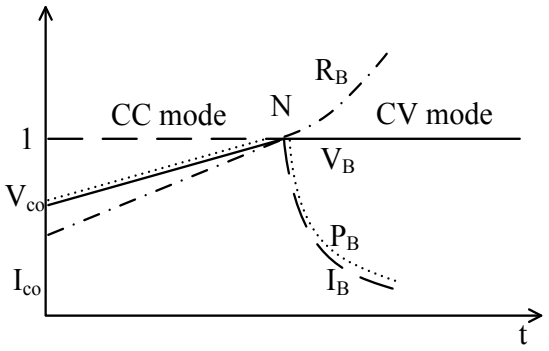

Fig. 4.2.1. Battery charging: normalized profiles of voltage (solid line), current (dashed line), power (dotted line) and resistance (dashed-dotted line).

4.3 WBC FOMs and their calculation

FOMs and their calculations are already done in the previous chapter and explained here very briefly to make explanation easier. Circuit diagram of WBC with the resonant SS topology is redrawn in Fig. 4.3.1 with predefined values. The induced voltages are rewritten as

$$\begin{cases} \bar{V}_T = j\omega M \bar{I}_R \\ \bar{V}_R = -j\omega M \bar{I}_T \end{cases} \tag{4.3.1}$$

Five FOMs are defined for WBC, namely overall efficiency (or simply, efficiency) η, power transfer ratio (PTR), receiver efficiency (RE), supply inverter power sizing factor (SIPSF) and receiver coil power sizing factor (RCPSF). They are defined as

$$\eta \triangleq \frac{P_B}{P_S} \tag{4.3.2}$$

$$PTR \triangleq \frac{P_R}{P_S} \tag{4.3.3}$$

$$RE \triangleq \frac{P_B}{P_R} \tag{4.3.4}$$

$$\text{SIPSF} \triangleq \frac{A_S}{P_N} \tag{4.3.5}$$

$$\text{RCPSF} \triangleq \frac{A_R}{P_N} \tag{4.3.6}$$

where P_N is nominal power given as the product of battery voltage in CV mode and battery current in CC mode. As it can be readily seen, PTR represents the transmitter efficiency and the product of PTR by RE gives the efficiency. Power sizing such as A_I, A_R and A_T are already explained in the previous chapter. Considering circuit of Fig. 4.3.1 in resonance, the impedance seen by $\bar{V}_R$ as well as by $\bar{V}_S$ is resistive. Then, the currents $\bar{I}_R$ and $\bar{I}_T$ are in phase with $\bar{V}_R$ and $\bar{V}_S$, respectively, and the voltage equations for the two meshes are

$$V_S = r_T I_T + \omega M I_R \tag{4.3.7}$$

$$V_R = r_R I_R + V_L \tag{4.3.8}$$

Moreover, the relationship between the two currents, as calculated on the receiver side by help of (4.3.1), is

$$\frac{\omega M}{r_R + R_L} I_T = I_R \tag{4.3.9}$$

From the circuit diagram of Fig. 4.3.1, efficiency, PTR and RE can be expressed as

$$\eta = \frac{P_B}{P_{JT} + P_{JR} + P_B} \tag{4.3.10}$$

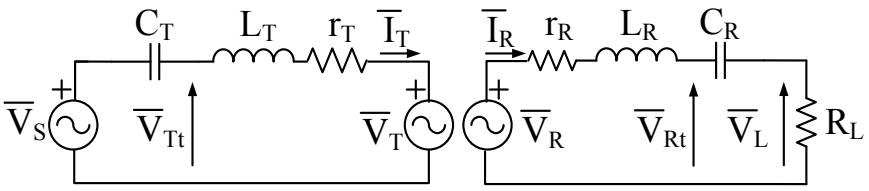

Fig. 4.3.1. SS resonant WBC circuit diagram.

$$PTR = \frac{P_{JR}+P_B}{P_{JT}+P_{JR}+P_B} \tag{4.3.11}$$

$$RE = \frac{P_B}{P_{JR}+P_B} \tag{4.3.12}$$

where $P_{JT} = r_T I_T^2$ and $P_{JR} = r_R I_R^2$ are the power losses in the transmitter and receiver, respectively, and $P_B = R_L I_R^2$. By substituting these power expressions in (4.3.10)-(4.3.12) and the help of (4.3.9), one obtains

$$\eta = \frac{R_L}{\frac{r_T}{(\omega M)^2}R_L^2+\left[1+\frac{2r_T r_R}{(\omega M)^2}\right]R_L+r_R\left[1+\frac{r_T r_R}{(\omega M)^2}\right]} \tag{4.3.13}$$

$$PTR = \frac{1}{\frac{r_T}{(\omega M)^2}R_L+\left[1+\frac{r_T r_R}{(\omega M)^2}\right]} \tag{4.3.14}$$

$$RE = \frac{R_L}{r_R+R_L} \tag{4.3.15}$$

Power sizing factor of the supply inverter and the receiving coil can be simplified without impairing significantly the results by neglecting the parasitic resistances of the coils. By (4.3.7) and (4.3.9), V_S and I_T can be simplified as

$$V_S \cong \omega M I_R \tag{4.3.16}$$

$$I_T \cong \frac{R_L}{\omega M} I_R = \frac{V_L}{\omega M} \tag{4.3.17}$$

From (4.3.5), (4.3.7), (4.3.16) and (4.3.17) SIPSF is given as

$$SIPSF = \frac{max[I_R]\,max[V_L]}{P_N} \tag{4.3.18}$$

From the circuit diagram of Fig. 4.3.1, the voltage across the receiving coil terminals is

$$\bar{\bar{V}}_{Rt} = \bar{V}_R - j\omega L_R \bar{I}_R \tag{4.3.19}$$

Since $\bar{I}_R$ is in phase with $\bar{V}_R$, the two voltage terms on the right hand side of (4.3.19) are in quadrature, and $\bar{V}_{Rt}$ is equal to

$$V_{Rt} = \sqrt{(\omega M I_T)^2 + (\omega L_R I_R)^2} \tag{4.3.20}$$

By (4.3.1), eq. (4.3.20) becomes

$$V_{Rt} = \sqrt{V_R^2 + (\omega L_R I_R)^2} \tag{4.3.21}$$

Using (4.3.6), (4.3.8) and (4.3.21) RCPSF is expressed as

$$RCPSF = \frac{max\left[\sqrt{V_R^2+(\omega L_R I_R)^2}\right] max[I_R]}{P_N} \tag{4.3.22}$$

4.4 WBC arrangement operation

4.4.1 WBC arrangement #1

Circuitry of WBC arrangement #1 is drawn in Fig. 4.4.1, where capacitor C_{DC} and inductor L_F act as low-pass filters of the rectifier output voltage and current, respectively. By assuming ideal low-pass filtering, the voltage across capacitor C_{DC} is direct as well as the current through inductor L_F. According to the circuitry operation, the sinusoidal current $\bar{I}_R$ is rectified and its average value coincides with I_B. Therefore, the capacitor voltage is equal to V_B and the

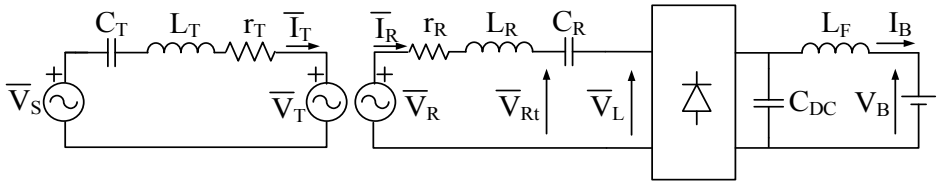

Fig. 4.4.1. WBC arrangement #1 circuitry.

voltage at the rectifier input has a square-waveform of magnitude V_B. It is worth to note that $\bar{V}_L$ is in phase with $\bar{I}_R$ so that the receiver sees a resistance at the input terminals of the rectifier. Such a resistance, previously termed as load resistance, is given by

$$R_L = \frac{V_L}{I_R} \tag{4.4.1}$$

where the rms values of $\bar{V}_L$ and $\bar{I}_R$, as a function of V_B and I_B, are

$$V_L = \frac{1}{\sqrt{2}}\frac{4}{\pi}V_B \tag{4.4.2}$$

$$I_R = \frac{1}{\sqrt{2}}\frac{\pi}{2}I_B \tag{4.4.3}$$

By (4.4.1)-(4.4.3), the load resistance is

$$R_L = \frac{8}{\pi^2}R_B \tag{4.4.4}$$

Eqn. (4.4.4) shows that, apart from a coefficient, the load resistance is proportional to the battery resistance.

4.4.2 WBC arrangement #2

Circuitry of WBC arrangement #2 is already discussed in the previous chapter. Operation of arrangement #2 differs from arrangement #1 as follows. Let the voltage across C_{DC} be kept constant at $V_{DC} \geq V_M$ in any charging condition. Then, the chopper adapts its input voltage V_{DC} to the battery voltage V_B with a duty-cycle δ equal to

$$\delta = \left(\frac{V_B}{V_{DC}}\right) \tag{4.4.5}$$

The duty-cycle along CC mode varies from V_{co}/V_{DC} to V_M/V_{DC}. Afterwards, in CV mode, the duty-cycle remains constant and equal to V_M/V_{DC}. Due to the duty-cycle, the resistance seen by capacitor C_{DC} is

$$R_{DC,B} = V_{DC}^2\frac{R_B}{V_B^2} \tag{4.4.6}$$

By replacing R_B in (4.4.1) with $R_{DC,B}$ the load resistance becomes

$$R_L = \frac{8V_{DC}^2}{\pi^2}\frac{R_B}{V_B^2} \tag{4.4.7}$$

Eq. (4.4.7) shows that the load resistance is proportional to the battery resistance, and inversely proportional to the square of the battery voltage

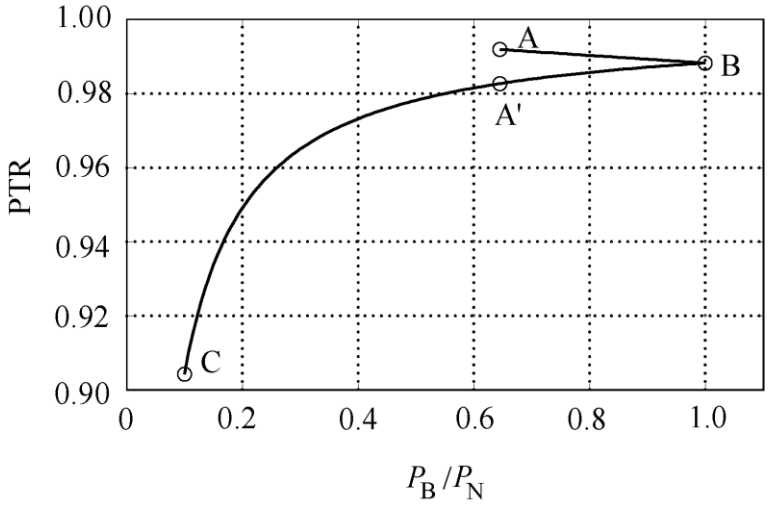

Fig. 4.5.1. PTR for WBC arrangement #1 and #2

4.5 Arrangement comparison

4.5.1 Study case

The study case considered here is the porotype of a resonant WBC for electric city-car developed in [6].

4.5.2 PTR, RE and efficiency

PTR, RE and efficiency along the battery charging process for the two arrangements are traced in Figs. 4.5.1-4.5.3 as a function of power P_B normalized to P_N. The curves ABC belong to arrangement #1 and those A'BC to arrangement #2. The curves in Figs. 4.5.1-4.5.3 are discussed in the subsequent Subsections for the battery charging process starting in CC mode at voltage V_{co}

For arrangement #1, the load resistance in (4.3.13)- (4.3.15) is expressed in terms of P_B by means of (4.2.1) and (4.4.4) whereas, for arrangement #2, it is expressed in terms of P_B by means of (4.2.1) and (4.4.7). Analysis of arrangement #2 is carried out by setting V_{DC} at V_M. Then, according to (4.4.6), $R_{DC,B}$ decreases from 8.7 to 5.6 Ω (i.e. the value of R_N) in CC mode and coincides with R_B in CV mode. Note that, for arrangement #1, R_B increases from 3.6 to 5.6 Ω in CC mode.

WBC arrangement #1

PTR: at V_{co}, PTR is calculated as 0.99 and is indicated with point A in Fig.4.5.1. By (4.3.11) and (4.4.2), while the battery charging process goes on in CC mode, the voltage V_R increases linearly with V_B. By (4.3.1), this involves a proportional increase of I_T and a power-of-two increase of the power losses in r_T. In turn, the active power transferred to the receiver increases proportionally to V_B. In the aggregate, PTR decreases a bit at the CC mode completion (point B). In CV mode, the voltage V_R is nearly constant and the same occurs for the power losses in r_T while power P_B decreases. Therefore, PTR decreases, moving from point B to C, where PTR gets the minimum value of 0.90. In the PTR curve as well in RE and efficiency curves, it should be noted that point A' along the CV mode curve has the same power P_B of point A.

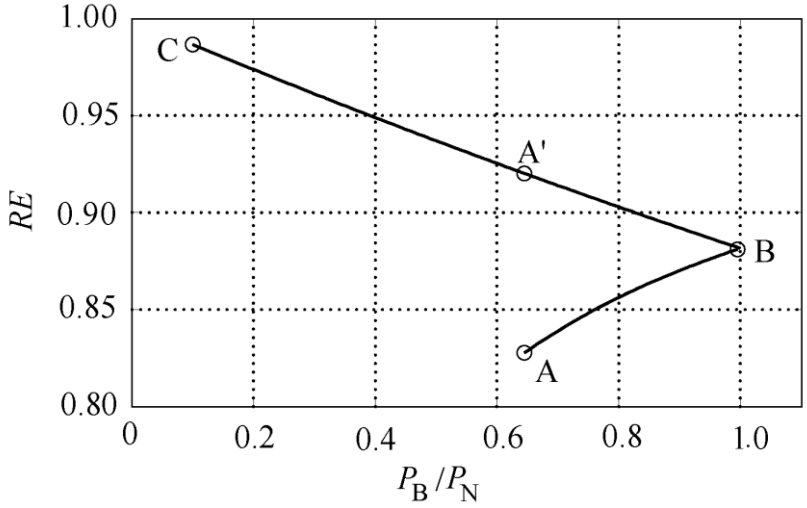

Fig. 4.5.2. RE for WBC arrangements #1 and #2

RE: at V_{co}, RE is calculated as 0.83 and is indicated with point A in Fig.4.5.2. While the battery charging process goes on in CC mode, the power losses in r_R remain constant while power P_B increases. Correspondingly, RE increases to 0.88 at the CC mode completion (point B). In CV mode, the power losses in r_R decrease with the square of the current while power P_B decreases proportionally to the current. In the aggregate, RE increases up to 0.98 (point C).

Efficiency: at V_{co}, power P_B is 360W. The relevant efficiency is calculated to be 0.82 and is indicated with point A in Fig.4.5.3. While the battery charging process goes on in CC mode, the increase in RE prevails on the decreases of PTR. Indeed, the power losses in r_R are constant while those in r_T increase but remain lower. This because in CC mode it is $\omega M > R_L + r_R$ and hence, by (4.3.9), current I_T is less than current I_R. Correspondingly, the efficiency increases from point A to B, which is reached at the CC mode completion point and has coordinates of P_B=560W, h=0.87.

In CV mode there is an increase of RE concurrently with a decrease of PTR. Efficiency continues to increase until the power losses in r_R are greater than in r_T; afterwards, the decrease in PTR prevails on the increase of RE and the efficiency decreases. The efficiency

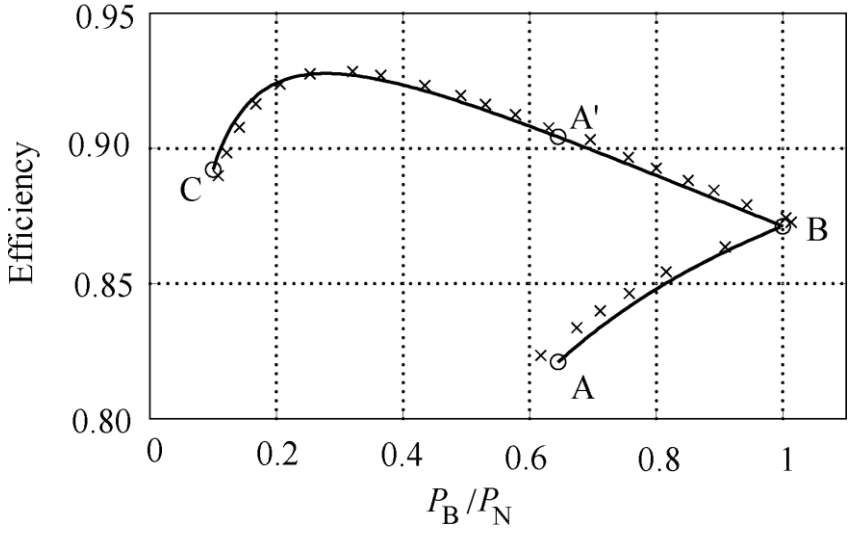

Fig. 4.5.3. Efficiency for arrangements #1 and #2 and experimental results

curve is BA'C, with efficiencies of 0.9 and 0.89 at points A' and C, respectively. The curve exhibits a maximum of 0.93 for a value of P_B, denoted as $P_{B,max}$, equal to 156W.

WBC arrangement #2 efficiency

The main feature of arrangement #2 is operation at constant chopper input voltage, which means that voltage V_L remains constant all along the charging process at the value given by (4.4.2), provided that V_B is substituted for by V_M. Therefore, the PTR, RE and efficiency curves differ from those of arrangement #1 only in CC mode.

Power P_B absorbed in CC mode by the battery is equal to the power absorbed in the interval of CV mode extending from P_{co} (abscissa of point A' of the curves) to P_N (abscissa of point B of the curves), where P_{co} is the power value absorbed in CC mode at V_{co}. On the other hand, resistance $R_{DC,B}$ in CC mode mirrors R_B in the interval of CV mode. Therefore, the PTR, RE and efficiency curves in CC mode are given by that portion of the curves in CV mode departing from A' and arriving at B.

A short explanation of the curve profiles in CC mode is given below. Instrumental in the explanation is the following equation that equates the power absorbed by the battery to that absorbed by the chopper:

$$I_{DC} = \frac{I_{CC}}{V_M} V_B \qquad (4.5.1)$$

By replacing I_B in (4.4.3) with I_{DC}, current I_R is obtained. Eqn. (4.5.1) puts in evidence that here, differently from arrangement #1, it is current I_R and not voltage V_R that increases in CC mode on account of the increase of voltage V_B.

PTR: at V_{co}, PTR is given by point A' in Fig.4.5.1. While the battery charging process goes on in CC mode, the power losses in r_T are nearly constant while the power transferred to the receiver increases. Then, PTR increases up to point B, which is reached at the CC mode completion.

RE: at V_{co}, RE is given by point A' in Fig.4.5.2. While the battery charging process goes on in CC mode, the power losses in r_R increase at the square of I_R while power P_B increases linearly with it. Then, PTR decreases to point B, which is reached at the CC mode completion.

Efficiency: at V_{co}, efficiency is given by point A' in Fig.4.5.3. While the battery charging process goes on in CC mode, the decrease in RE prevails on the increase of PTR because, by (4.3.9), the change of the power losses in r_R is much greater than in r_T. Then, the efficiency decreases to point B, which is reached at the CC mode completion.

Efficiency comparison

The curves of Fig.4.5.3 indicate that the efficiency in CC mode is higher for arrangement #2. This is because, along the CC mode, the following occurs: i) current I_R is lower than with arrangement #1; then, compared to arrangement #1, the power losses in r_R are lower, ii) voltage V_L stays constant at its maximum value, reached only at the CC mode completion for arrangement #1; then, compared to arrangement #1, the power losses in r_T are greater, and iii)

current I_R is greater than I_T and the influence on the efficiency of the power losses in r_R overcomes that of the power losses in r_T.

SIPSF and RCPSF

By (4.3.18), calculation of SIPSF needs to find the maximum of I_R and V_L. For both the arrangements, the maximum of I_R is $I_R = \frac{1}{\sqrt{2}}\frac{\pi}{2} I_{CC}$ and the maximum of V_L is $V_L = \frac{1}{\sqrt{2}}\frac{4}{\pi} V_M$. = $\frac{1}{\sqrt{2}}\frac{4}{\pi} V_M$. Therefore, SIPSF is equal to 1. Accounting for parasitic resistances, the calculation of SIPSF would result in 1.14, due to excess in voltage V_S to face with the voltage drops across the parasitic resistances.

By (4.3.22), calculation of RCPSF needs to find the maximum of $\sqrt{V_R^2 + (\omega L_R I_R)^2}$ and I_R. For both arrangements, the maximum of $\sqrt{V_R^2 + (\omega L_R I_R)^2}$ is achieved at point N of the charging profile, where V_R and I_R get their maximum values concomitantly. Regarding the maximum of I_R, the same applies as for SIPSF. By (4.4.7), RCPSF results in 14.15. If the parasitic resistances are accounted for, the calculation of RCPSF would result in 14.16, which is evidence of the fact that the parasitic resistances have little impact on RCPSF.

By (4.3.20) and (4.3.1), V_R is somewhat less than $\omega L_R I_R$ since both the following inequalities apply: $M < L_R$ and $I_T < I_R$. Thus, RCPSF can be approximated as

$$RCPSF \cong \frac{\pi^2}{8}\frac{\omega L_R}{R_N} \qquad (4.5.2)$$

Eq. (4.5.2) shows that RCPSF is about equal to the quality factor of the receiving coil loaded with the battery resistance at point N of the charging resistance profile. By (4.5.2), RCPSF results in 14.11. If the parasitic resistances are accounted for, calculation of RCPSF would result in 14.16.

4.6 Chopper input voltage selection

The issue can arise about the selection of the chopper input voltage V_{DC} for WBC arrangement #2. To investigate the issue, efficiency have been calculated, besides for $V_{DC}=V_M$, for other two values of V_{DC}, namely 1.2 V_M and 1.4 V_M. The resultant efficiency curve is drawn in Fig. 4.6.1

First of all, it emerges from Fig.4.6.1 that the efficiency curves retain the same profile as for $V_{DC}=V_M$. However, the efficiency increases with voltage V_{DC} for high values of power P_B, while the opposite occurs for low values of power P_B. This behavior arises from the opposite effects of voltage V_{DC} on the power losses in r_R and r_T; actually, against an increase of voltage V_{DC}, the power losses in r_R decrease because of the lower values of I_R while those in r_T increase because of the higher values of I_T. Therefore, effect of the power losses in r_R predominates at higher values of power P_B, when I_R approaches its maximum value, while effect of the power losses in r_T predominates at the lower values of power P_B. Moreover, the efficiency curves exhibit i) an equal maximum, and ii) a shift of the abscissa $P_{B,max}$ of the maximum towards the higher values of power with the increase of voltage V_{DC}.

By (4.3.13), the maximum of efficiency is obtained for

$$R_{L,max} = \sqrt{\frac{r_R(\omega^2 M^2 + r_T r_R)}{r_T}} \tag{4.6.1}$$

and its value results in

$$\eta_{max} = \frac{1}{\frac{2r_T r_R}{(\omega M)^2} + 2\frac{r_T}{(\omega M)^2}\sqrt{\frac{r_R(\omega^2 M^2 + r_T r_R)}{r_T}} + 1} \tag{4.6.2}$$

Expression (4.6.2) proves that η_{max} depends on the mutual inductances of the coil, in addition to the coil parasitic resistances. Therefore it is independent of V_{DC}. Incidentally, it can be noted that also $R_{L,max}$ is independent of V_{DC}. For the study case, it is $R_{L,max} = 16.28\,\Omega$, and $\eta_{max} = 0.94$.

With the selected values of V_{DC}, along CC mode R_L is lower than $R_{L,max}$ and η_{max} is not reached; instead, along CV mode R_L increases substantially and operation at maximum efficiency is achieved. From (4.2.1) and (4.4.6), the power P_B in correspondence of η_{max}, expressed in terms of V_{DC}, is equal to

$$P_{B,max} = \frac{8}{\pi^2}\frac{V_{DC}^2}{R_{L,max}} \tag{4.6.3}$$

Eq. (4.6.3) underlines that the position of the maximum increases with V_{DC} at the power of two. SIPSFs calculated for the three values of V_{DC} by accounting for the parasitic resistances are: 1.14 for V_{DC}=V_M, 1.11 for V_{DC}=1.2V_M and 1.09 for V_{DC}=1.4V_M, underlining a small decrease of SIPSF at higher values of V_{DC}. RCPSFs, in turn, are 14.16, 9.86 and 7.28, underlining an appreciable decrease of RCPSF at the higher values of V_{DC}. For both the factors, the reduction in their values is due to the reduction in I_R that, in turn, decreases the voltage drop across L_R.

The results of Fig.4.6.1 suggest that the most convenient selection for V_{DC} is to set $P_{B,max}$ in the middle of the interval of power P_B with extremes P_{co} and P_N. There are two reasons at the basis of this selection: (1) Most of the charge of the battery is done in CC mode and in the

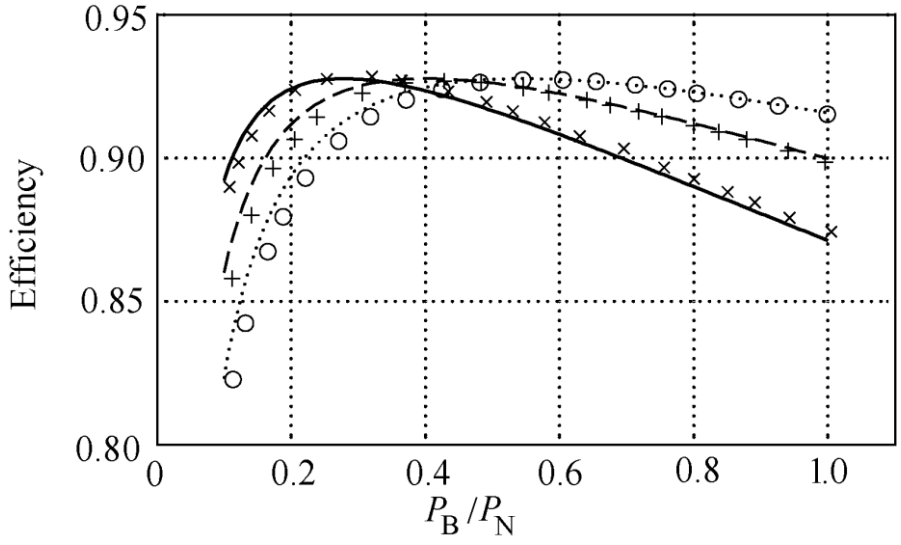

Fig. 4.6.1. Efficiency for WBC arrangement #2 with V_{DC}=V_M (solid line), V_{DC}=1.2 V_M (dashed line) and V_{DC}=1.4 V_M (dotted line) and experimental results

successive interval of CV with equal values of power P_B. (2) Most of the energy flows through WBC with power levels comprised between P_{co} and P_N. For the case study, such a value of $P_{B,max}$ is 460 W and it is obtained for V_{DC} equal to 1.7 V_M.

4.7 Power sizing of the transmitting and receiving coils

The power sizing of the receiving coil is given by (3.5.5), where $max(V_{Rt})$ is the maximum of (4.3.21). The power sizing of the transmitting coil is expressed as in (3.5.7) and from the circuit diagram of Fig. 4.3.1, the voltage across the transmitting coil terminals is

$$\bar{V}_{Tt} = \bar{V}_T + j\omega L_T \bar{I}_T \tag{4.7.1}$$

Since $\bar{I}_T$ is in phase $\bar{V}_T$, the magnitude of $\bar{V}_{Tt}$ is

$$V_{Tt} = \sqrt{(\omega M I_R)^2 + (\omega L_T I_T)^2} \tag{4.7.2}$$

The maximum of V_{Tt} is again achieved at point N of the charging profile, where both I_R and I_T get the maximum values. By (4.3.20), the relationship between A_T and A_R can be written as

$$A_T = \frac{\sqrt{(M)^2 + \left[L_T \frac{max(I_T)}{max(I_R)}\right]^2}}{\sqrt{(M)^2 + \left[L_R \frac{max(I_R)}{max(I_T)}\right]^2}} A_R \tag{4.7.3}$$

Eq. (4.7.3) shows that the relationship between the power sizing of the transmitting and receiving coils depend on the inductive parameters of the coils and the load resistance.

4.8 Conclusions

The chapter has examined two different WBC arrangements for EVs, one with the receiver that charges the battery directly and the other one with the receiver cascaded by a chopper. FOMs (efficiency, power transfer ratio, receiver efficiency, power sizing factor of both the supply inverter and the receiving coil) of the two WBC arrangements have been formulated as a function of the power absorbed by the battery, and calculated for the study case of WBC for an electric city-car. Comparisons of the FOMs have shown the convenience of using the WBC arrangement with the chopper. Afterwards, FOMs of this arrangement have been evaluated for different chopper input voltages, revealing that a higher voltage is beneficial for all the FOMs, except for the efficiency when the transferred power is low.

4.9 References

[1] H.H. Wu, G.A. Covic, J.T. Boys, and D.J. Robertson, "A Series-Tuned Inductive-Power-Transfer Pickup With a Controllable AC-Voltage Output," *IEEE Transactions on Power Electronics*, vol. 26, no. 1, pp. 98-109, 2011.

[2] H. H. Wu, J.T. Boys, and G.A. Covic, "An AC Processing Pickup for IPT Systems," *IEEE Transactions on Power Electronics*, vol. 25, no. 5, pp. 1275-1284, 2010.

[3] J.E. James, D.J. Robertson, and G.A. Covic, "Improved AC Pickups for IPT Systems," *IEEE Transactions on Power Electronics*, vol. 29, no. 12, pp. 6361-6374, 2014.

[4] L.J. Zou, A.P. Hu, D.Robertson, and B.Wang, "A new rectifier with combined power flow control capability for a series-tuned inductive-power-transfer receiver," Proc.

IEEE International Conference on Power System Technology (POWERCON), 2012, pp. 1-6.

[5] K.Colak, M.Bojarski, E.Asa, and D.Czarkowski, "A constant resistance analysis and control of cascaded buck and boost converter for wireless EV chargers," Proc. IEEE Applied Power Electronics Conference and Exposition (APEC), 2015, pp. 3157-3161.

[6] G.Buja, M.Bertoluzzo and K.N.Mude, "Design and experimentation of WPT charger for electric city-car", *IEEE Transactions on Industrial Electronics*, vol. 62, no. 62, pp. 7436-7447, 2015.

Chapter 5

Mismatch analysis and tuning of frequency

5.1 Introduction

Need of resonance in transmitting and receiving stages of WBC system is well known and urge for its better performance [1]-[5]. Full compensation or resonance in the both stages is possible for equal values of L by C product. And so, change in any of the reactive parameter from its nominal value deviates the belonging stage from resonance [6]. Parameter can change either during installation or during life span of EV. Deviation caused during installation can be compensated by proper selection of supply frequency while later situation can occur due to thermal and aging actions. Such deviation can be overcome by, either adding extra reactive element in the system or updating the supply frequency [7],[8]. Adding extra reactive element in the WBC system makes it bulky and expensive which obviously is not convenient for EVs. Update of supply frequency in order to bring affected stage back to resonance can deviate other stage from resonance or can deviate both the stages from resonance if update is done to make input impedance pure resistive. Study of supply frequency mismatch on efficiency and supply inverter power sizing factor and a comparative study of three different types of supply frequency update is presented in this chapter.

5.2 SS resonant WBC system

Equivalent circuit of SS topology considering source resistance r_S is shown in Fig. 5.2.1 where all the variables has the same meaning as explained in the previous chapter. Expressions for efficiency and supply inverter power sizing factor (SIPSF) from eqns. (2.3.8) and (2.3.9) taking r_S into account are given as

$$\eta_{SS} = \frac{\omega^2 M^2 R_L}{|\dot{Z_R}|^2 r_{ST} + \omega^2 M^2 r_{RL}} \tag{5.2.1}$$

$$SIPSF = \frac{|\dot{Z_R}||\dot{Z_R}\dot{Z_T} + \omega^2 M^2|}{\omega^2 M^2 R_L} \tag{5.2.2}$$

Considering r_S+r_T as the total resistance of transmitting stage as r_{ST} and r_R+R_L as r_{RL} expression of impedances $\dot{Z_T}$ and $\dot{Z_R}$ are

$$\begin{cases} \dot{Z_T} = r_{ST} + j\omega L_T + \frac{1}{j\omega C_T} \\ \dot{Z_R} = r_{RL} + j\omega L_R + \frac{1}{j\omega C_R} \end{cases} \tag{5.2.3}$$

It is clear from (5.2.1) that resonance in receiving stage improves efficiency while in the case of SIPSF it is necessary to have resonance in both the stages as seen by (5.2.2) for the

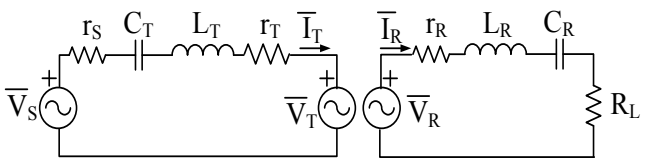

Fig. 5.2.1 Equivalent circuit of SS topology

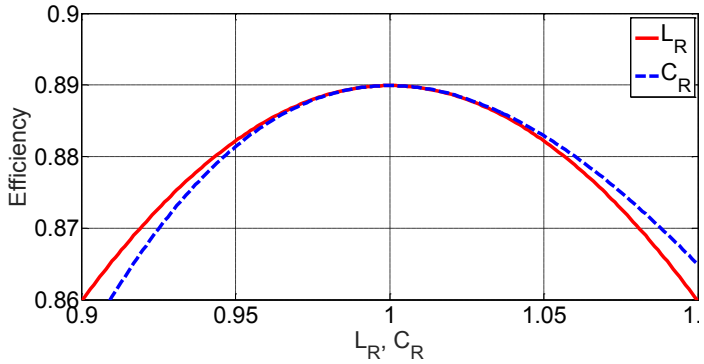

Fig. 5.3.1. Efficiency vs. L_R and C_R.

sake of its minimization. Minimization of $\dot{Z}_T$ and $\dot{Z}_R$ can be reached by having resonance in pairs L_T, C_T and L_R, C_R, which can be achieved by proper selection of resonating capacitor of both stages.

At resonance (5.2.3) turns into

$$\begin{cases} \dot{Z}_T = r_{ST} \\ \dot{Z}_R = r_{RL} \end{cases} \tag{5.2.4}$$

Substituting (5.2.4) into (5.2.1) and (5.2.2) it gives

$$\eta_{SS,res} = \frac{\omega^2 M^2 R_L}{r_{RL}(r_{RL} r_{ST} + \omega^2 M^2)} \tag{5.2.5}$$

$$SIPSF_{res} = \frac{r_{RL}(r_{RL} r_{ST} + \omega^2 M^2)}{\omega^2 M^2 R_L} \tag{5.2.6}$$

It is clear from (5.2.5) and (5.2.6) that; at resonance, efficiency is inverse of SIPSF which is due to the fact that WBC system becomes pure resistive during resonance and hence total power supplied by power source is the active power absorbed by r_{ST} and r_{RL}.

5.3 Frequency mismatch analysis under nominal supply frequency

It is clear that variation of reactive parameters from their nominal value deviate WBC system from resonance and in this case system is no more resistive and become reactive.

Further discussion on mismatch analysis is carried out for R_L correspondence to the nominal charging power i.e. 6.1 Ω, with an assumption that only one reactive parameter

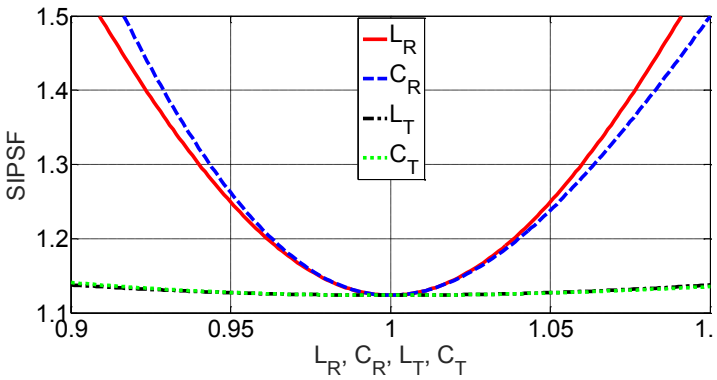

Fig. 5.3.2. SIPSF vs. L_R, C_R, L_T and C_T.

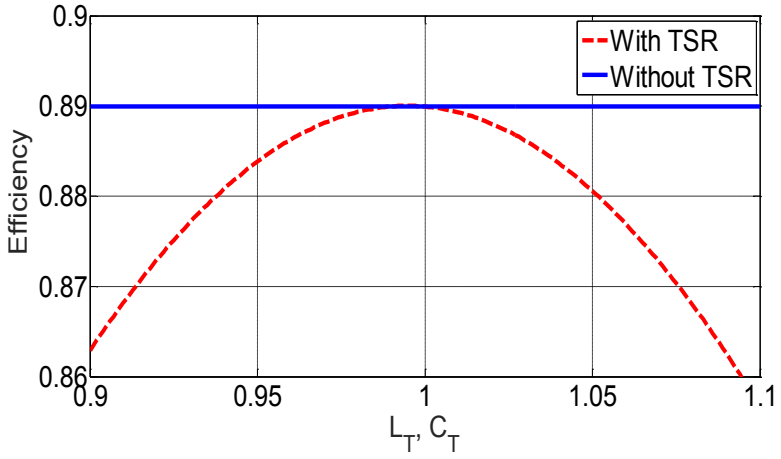

Fig. 5.4.1. Efficiency vs. L_T and C_T with and without TSR.

changes at a time within ±10% of their nominal value. Deviation of the parameter reported in the graphs are normalized to their respective nominal values. Variation of L_R or C_R from its nominal value diverge $|\dot{Z}_R|$ from resonance and deviate it from its minimum, which results into decrease of efficiency. As shown in Fig. (5.3.1) Variation of L_R or C_R from its nominal value effect efficiency in the same way and reduces it about 3% at the extremities of the parameter deviation range.

According to (5.2.2) it is clear that reactive parameter of both transmitting and receiving section effect SIPSF and hence deviation in any of them deviate SIPSF from its minimum value. Effect of deviation of L_R, C_R, L_T and C_T from its nominal value is shown in Fig. 5.3.2 where it can be observed that deviation of L_R and C_R increases SIPSF of about 35% and 1% in case of L_T and C_T in the same parabolic like behavior.

Based on the objective of supply frequency update in order to maximize efficiency and minimize SIPSF three updates are possible termed as transmitting stage resonance (TSR), receiving stage resonance (RSR) and input impedance resonance (IIR) which is discussed in the next sections.

5.4 Frequency mismatch analysis under transmitting stage resonance

Transmitting stage resonance i.e. TSR is achieved by updating supply frequency in such a way that transmitting stage is always in resonance when one of parameter from L_T, C_T pair changes. From above discussion, it is assumed that L_R, C_R is at their nominal value and does not change. TSR does not depend on the presence of receiver i.e. EV and its objective is to resonate transmitting stage so will deviate receiving stage from resonance during its presence in the case of variation of L_T and C_T.

Effect on efficiency due to TSR can be understood from (5.2.8) where update of supply frequency in order to achieve TSR will deviate $|\dot{Z}_R|$ from its resonance and results into reduction of efficiency. Fig. 5.4.1 plots efficiency in this case with and without TSR and is found that efficiency decreases of about 3% at the extremities of the parameter deviation range. Presence of only one curve with TSR is due to the fact that L_T and C_T have the same normalized value and same effect on efficiency due to their change. Slight variation in efficiency in the case of without TSR is explained above and present here just for comparison.

Since SIPSF depends upon L_T and C_T and so it will be interesting to see whether TSR affect it in a positive or negative way. Fig. 5.4.2 plots SIPSF in this case with and without TSR, which shows that with TSR, SIPSF increases more than 33% at the extremities of parameter deviation range which is higher than the case of without TSR. Presence of one curve with TSR is due to the same reason as given in the case of efficiency.

Based upon above discussion it is clear that TSR is neither beneficial for efficiency nor SIPSF as it affect these twos in the adverse manner. So such update of supply frequency is not favorable for WBC system and should be avoided.

5.5 Frequency mismatch analysis under receiving stage resonance

Receiving stage resonance i.e. RSR is achieved by updating supply frequency in such a way that receiving stage is always in resonance when one of parameter of L_R, C_R pair changes. From above discussion it is assumed that L_T, C_T are at their nominal value and does not change. RSR depends on the presence of receiver i.e. EV, and its objective is to resonate receiving stage so will deviate transmitting stage from resonance in the case of variation of L_R and C_R.

Relation between transmitter and receiver stage current is

$$\bar{I_T} = j\frac{\dot{Z_R}}{\omega M}\bar{I_R} \tag{5.5.1}$$

Replacing $\dot{Z_R}$ from (5.2.4), (5.5.1) takes the form

$$\bar{I_T} = j\frac{r_{RL}}{\omega M}\bar{I_R} \tag{5.5.2}$$

Which shows that during RSR phase displacement between the currents of the transmitter and receiver stage is π/2. According to (5.2.1) it is clear that efficiency dependents upon $\dot{Z_R}$ in inverse way, since RSR keeps $\dot{Z_R}$ always minimum by maintaining receiving stage in resonance so, RSR will be beneficial for efficiency as shown in Fig. 5.5.1. Efficiency in the region less than nominal value of L_R, C_R is higher due to the fact that in this region supply frequency is more than resonance frequency in order to have RSR. While for the region higher value of L_R, C_R than its nominal value, efficiency is less because supply frequency is less than resonance frequency. However, variation of efficiency is found to be of about 0.1%.

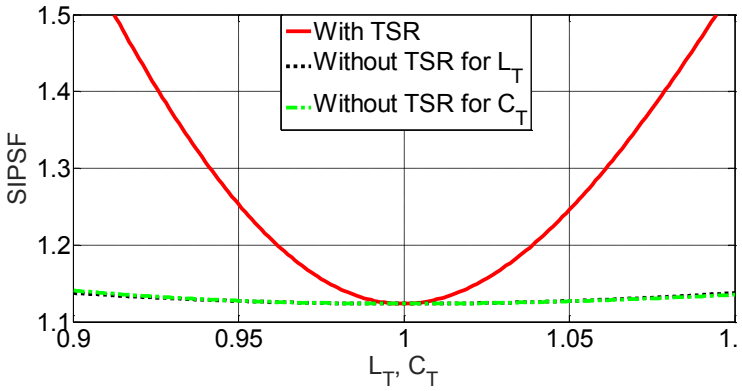

Fig. 5.4.2. SIPSF vs. L_T and C_T with and without TSR.

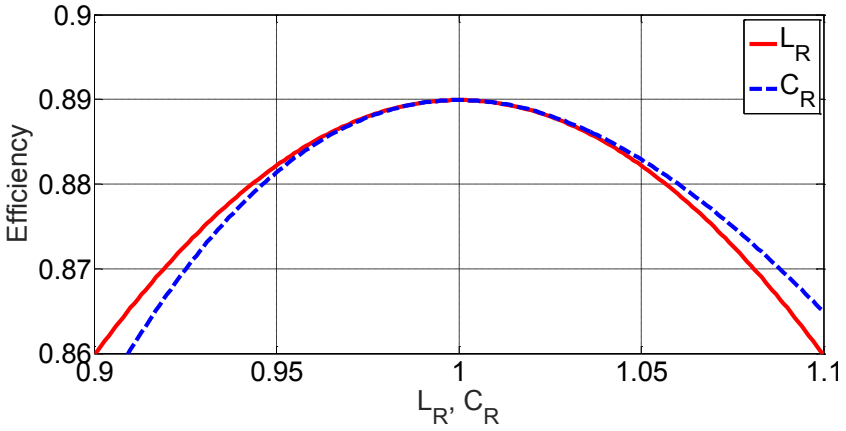

Fig. 5.5.1. Efficiency vs. L_R and C_R with and without RSR.

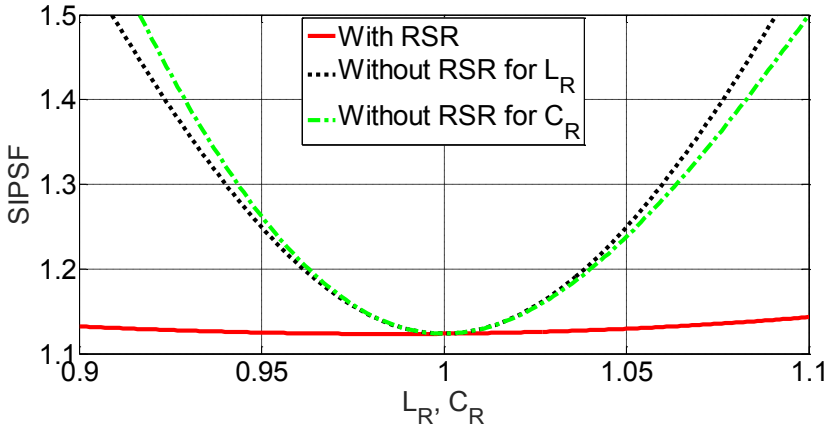

Fig. 5.5.2. SIPSF vs. L_R and C_R with and without RSR.

Presence of plots for the case of without RSR is in Fig. 5.5.1 is just for comparison. As for RSR, there is no difference in the variations of efficiency due to the deviations of L_R or of C_R, provided that the deviations have the same normalized value; for this reason there is only one curve with RSR in Fig. 5.5.1. Eqn. (5.3.10) clarify that RSR will be in favor of a minimal increase of SIPSF since it keeps $\dot{Z}_R$ minimum.

But case of SIPSF is different from efficiency because SIPSF depends on both $\dot{Z}_T$ and $\dot{Z}_R$. So, variation of supply frequency in order to achieve RSR deviates $\dot{Z}_T$ from its resonance and introduces reactive parameter in the system which increases $\dot{Z}_T$ and so SIPSF. Fig. 5.5.2 plots SIPSF as a function of L_R, C_R where SIPSF increases from its nominal value during variation of L_R, C_R due to the fact that $\dot{Z}_T$ is no more in resonance. The traces for without RSR is kept here just for comparison and for RSR, there is no difference in the variations of SIPSF due to the deviations of L_R or of C_R, provided that the deviations have the same normalized value; for this reason there is only one curve with RSR in Fig. 5.5.2.

5.6 Frequency mismatch analysis under input impedance resonance

Input impedance for WBC system is defined as the impedance seen from supply inverter terminals as shown in Fig. 5.6.1 where $\dot{Z}_i$ represent input impedance and its expression can be obtained as (5.6.1), in the case when both the stages are coupled as

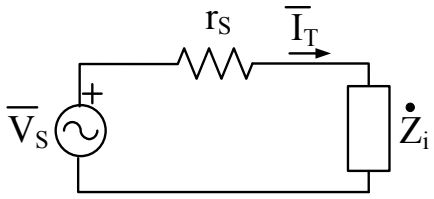

Fig. 5.6.1 Equivalent circuit for Input impedance

$$\dot{Z}_\iota = \frac{\dot{Z_T}\dot{Z_R}+\omega^2M^2}{\dot{Z_R}} \tag{5.6.1}$$

Having reactive component as

$$X_i = \omega L_T - \frac{1}{\omega C_T} - \frac{\omega^2M^2\left(\omega L_R - \frac{1}{\omega C_R}\right)}{r_{RL}^2+\left(\omega L_R - \frac{1}{\omega C_R}\right)^2} \tag{5.6.2}$$

in order to achieve IIR it is mandatory to make X_i zero by updating supply frequency which in this case may be different from the resonance frequencies of both the transmitter and receiver stages during charging or coupled condition. It is clear from above discussion that zero value of X_i results into zero phase displacement between $\overline{V_S}$ and $\overline{I_T}$.

5.6.1 Supply frequency update

Supply frequency which zeros X_i can be obtained by solving (5.6.2) which is a third order equation given as

$$A\Omega^3 + B\Omega^2 + C\Omega + D = 0 \tag{5.6.3}$$

here

$$\begin{cases} \Omega = \omega^2 \\ A = L_T C_T L_R^2 C_R^2 - C_T C_R^2 L_R M^2 = L_R C_T C_R^2 (L_T L_R - M^2) \\ B = L_T C_T C_R^2 R_R^2 - 2L_T C_T L_R C_R - L_R^2 C_R^2 + C_T C_R M^2 \\ C = 2L_R C_R + L_T C_T - C_R^2 R_R^2 \\ D = -1 \end{cases} \tag{5.6.4}$$

Solving (5.6.3) three possible roots are found as

$$\Omega_1 = 2\left(\sqrt{-\frac{p}{3}}\right) cos\left(\frac{\alpha}{3}\right) - \frac{b}{3a} \tag{5.6.4a}$$

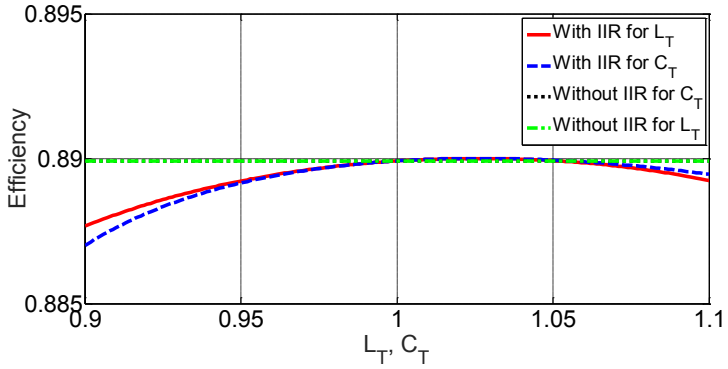

Fig. 5.6.2. Efficiency vs. L_T and C_T with and without IIR.

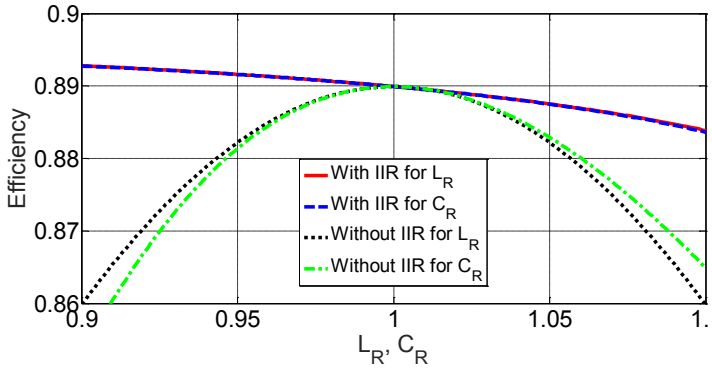

Fig. 5.6.3. Efficiency vs. L_R and C_R with and without IIR.

$$\Omega_{2,3} = -2\left(\sqrt{-\frac{p}{3}}\right)cos\left(\frac{\alpha \pm \pi}{3}\right) - \frac{b}{3a} \tag{5.6.4b}$$

Where

$$\alpha = cos^{-1}\left(\frac{-q}{2\left(\frac{-p}{3}\right)^{\frac{3}{2}}}\right) \tag{5.6.4c}$$

And

$$p = -\frac{1}{3}\left(\frac{B}{A}\right)^3 + \left(\frac{C}{A}\right) \tag{5.6.4d}$$

$$q = \frac{2}{27}\left(\frac{B}{A}\right)^3 - \left(\frac{BC}{3A^2}\right) + \left(\frac{D}{A}\right) \tag{5.6.4e}$$

$$D = \left(\frac{A^3}{27} + \frac{B^2}{4}\right) \tag{5.6.4f}$$

Based on the co-efficient of (5.6.3) it is possible to have at least one real solution. In the case when A>0 and D<0 there will have at least one real and positive solution and in the case when it has three real solution it will have at least one positive solution. In any case it has one positive solution which will give $\Omega > 0$. in the case of three positive solution, that value of

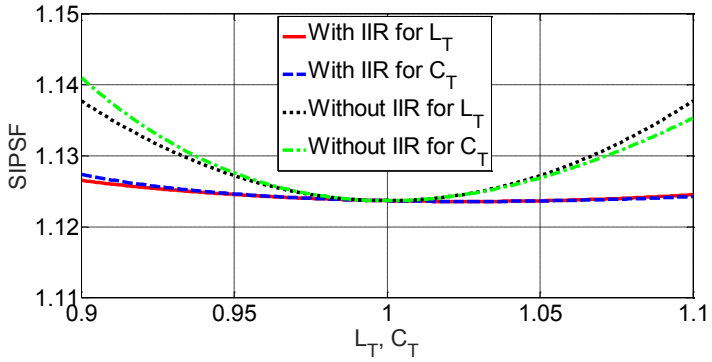

Fig. 5.6.4. SIPSF vs. L_T and C_T with and without IIR.

Ω is taken in account which is close to the nominal supply frequency.

5.6.2 Frequency mismatch impact

Let us consider the impact of a frequency mismatch on the efficiency and SIPSF of the WBC system when one of the reactive parameters L_R, C_R, L_T and C_T changes and the supply frequency is updated so as to make resonant the input impedance.

Since efficiency of the WBC system is not affected by the parameters of the transmitting stage, so supply frequency update in order to achieve IIR has an adverse effect on efficiency due to deviation of $\dot{Z}_R$ from resonance. Fig. 5.6.2 plots the efficiency as a function of the deviations of L_T and C_T both with IIR and without IIR. Here, the efficiency is slightly deteriorated by IIR, with a maximum drop of about 0.2% at the lowest values of L_T and C_T. Supply frequency update in order to achieve IIR in the case of variation of L_R and C_R enhance efficiency as it brings $\dot{Z}_R$ back into resonance.

Fig. 5.6.3 plots efficiency as a function of the deviations of L_R and C_R both with IIR and without IIR. As expected, the efficiency is kept at a maximum with IIR. Moreover, the traces show that the efficiency

i). Does not vary too much around the nominal value, the variations in the parameter deviation range being of about 0.1%.

ii). Increases for values of the reactive parameters less than the nominal ones whilst decreases in the opposite case. Which is due to the fact that supply frequency is higher w.r.t. resonance frequency in the case when parameter is less than the nominal value and contrary happens in the case of higher value of parameter from nominal one.

iii). Moreover, the traces show that the difference in the variations of efficiency produced by the same normalized deviations of LR or CR is negligible when the deviations are above the nominal values and barely appreciable when they are below

With regard to SIPSF, substitution of (5.2.10) in (5.6.1) reveals that α is proportional to $|\dot{Z}_\iota|$ according to

$$SIPSF = \frac{|\dot{Z}_R|^2 |\dot{Z}_\iota|}{\omega^2 M^2 R_L} \tag{5.6.5}$$

from (5.6.5) it is clear that IIR keeps low the change of α produced by the frequency mismatch in the receiver stage.

Fig. 5.6.4 plots SIPSF as a function of the deviations of L_T and C_T both with IIR and without IIR. Here, SIPSF is slightly better with IIR, the increase at the extremities of the parameter deviation range being less than 0.2%. The traces confirm the effectiveness of IIR in reducing SIPSF. Akin to the efficiency, the difference in the variations of SIPSF due to the same normalized deviations of L_R or C_R is very small.

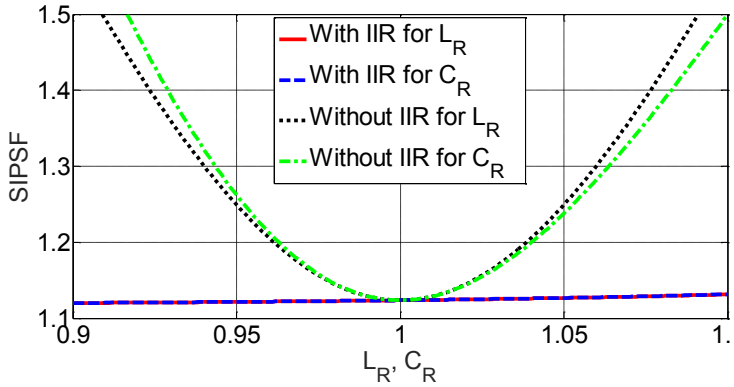

Fig. 5.6.5. SIPSF vs. L_R and C_R with and without IIR.

5.7. Frequency update convenience

Based upon above discussion on different supply frequency update technique and taking account their effect on efficiency and SIPSF it comes to know that TSR is the worst supply frequency update among all. One important matter of concern in case of wireless charging of EV is the allowable supply frequency range by taking account safety of pedestrian and driver of vehicle, for this reason SAE International Task Force has agreed on the frequency range of 81.38 – 90 kHz. Fig. 5.7.1 plots the range of frequency suggested by SAE and supply frequency update for RSR and IIR taking account the case of variation of L_R. It can be reported from Fig. 5.7.1 that; in case of RSR range of supply frequency lays within the SAE limit along most of the deviation range of L_R from its nominal value while it goes beyond the SAE limit for large part of L_R deviation in the case of IIR.

5.8. Practical implementation

From the above discussion it is clear that, the adjustment of the supply frequency in order to maintain resonance in the receiver, allows to achieve the best performance for the WBC system during reactive parameter change. The tuning procedure can be set as follows: a) the signal s_{iT} and s_{iR} can be obtained by transducing the current flowing in the transmitter and receiver stages respectively, b) the signal s_{iT} can be compared with s_{iR} to control the relative phase shift between the two signals i.e. $\pi/2$ during resonance, c) in presence of phase

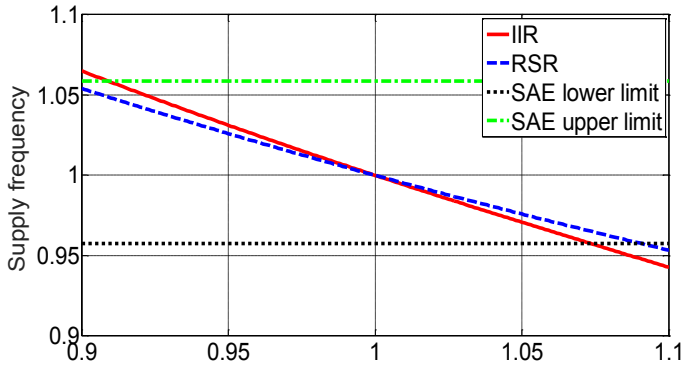

Fig. 5.7.1. Supply frequency update and SAE limit

error, an error signal which acts on the inverter frequency will be elaborated. In fact, the implementation of this adjustment is not practical because it requires the transmission of s_{iR} signal, which has a frequency of 85 kHz, via a wireless network with a not adequate bit rate.

Practical implementation can be done by keeping in resonance the reactance seen from the power supply i.e. IIR, accepting that the performance of IIR is not as good as the RSR, but being able to operate with signals relating to the transmitter stage only. The s_{iT} and the s_{vT} signals can be obtained by transducing the transmitter current and fundamental component of the inverter output voltage. The IIR requires that the relative phase shift between the two signals s_{iT} and s_{vT} becomes zero. The determination of the phase shift between the signals s_{vT} and s_{iT} is carried out by using the circuit as shown in Fig. 5.8.1. The heart of the circuit is the XOR gate. When two square wave signals having same frequency are applied at the input of XOR gate, the output is a square wave of double the frequency of the input signal and duty-cycle that is a linear function of the "phase difference" between the input signals. To recognize the sign of the “phase shift” , one of the two signals is kept “out of phase” of 90° , hence the “zero phase” condition corresponds to an average value of the output voltage of the XOR gate equal to half the supply voltage of the same door. In the circuit developed for the determination of the phase shift between the signals s_{vT} and s_{iT}, the bottom input of the XOR gate is a square wave signal with a duty cycle of 50%, obtained by “leading” the output voltage of inverter by 90°. It corresponds to the signal that would be obtained “leading” by 90° the fundamental component of the inverter output voltage and subsequently making it square. The second input is obtained by conditioning the s_{iT} signal. The conditioning consists of adding to the signal a continuous component in order to make it unipolar and to be able to acquire it by the A/D converter integrated in DSP of transmitter stage. Furthermore, to avoid the overloading of the output of the current transducer, the signal is sent to an operational amplifier configured as voltage follower and subsequently squared by means of a comparator. Since the signal is unipolar, the zero crossings of the current signal are detected by comparing the signal itself with its average value, obtained by means of a low-pass filter. In resonance condition, the “phase shift” between the input signals of XOR gate is 90°, duty-cycle of the signal at the output of the XOR gate is equal to 50% and its average value is equal to let us say V_m. In non-resonance condition, the “phase shift” is different from 90°, duty-cycle of the XOR output signal is different from 50%, and its average value is different from V_m. The

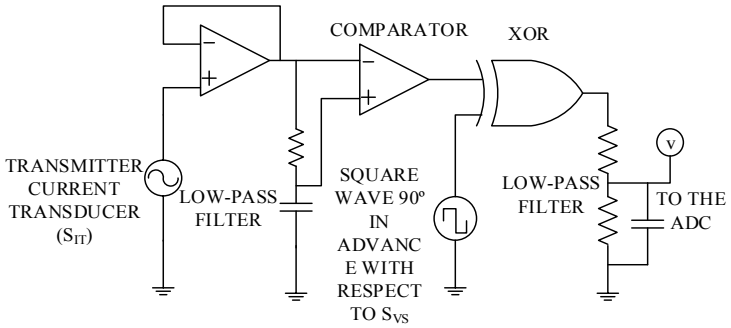

Fig. 5.8.1. Circuit for the determination of the phase displacement between $\overline{V_S}$ and $\overline{I_T}$

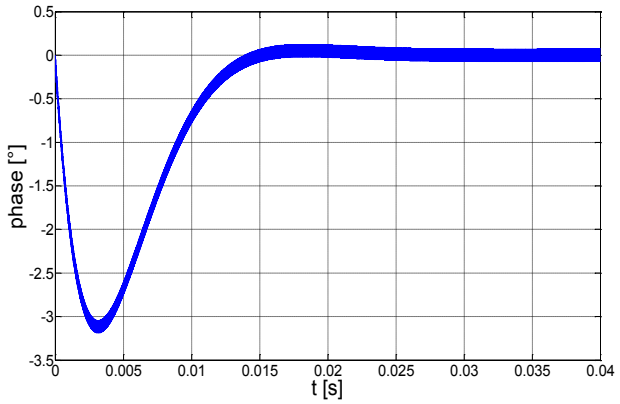

Fig. 5.8.2. Phase shift during the power supply frequency tuning..

difference between the average value and V_m gives the phase shift between $_{SiT}$ and $_{SvT}$.

The two low-pass filters used in the scheme have the function of extracting the continuous component (in steady-state condition) or variable low frequency (during transients) signal at their input, and removing the harmonic components at high frequency. The filters design is the result of a compromise between the need on one hand to minimize the harmonic components and on the other hand to follow rapidly its variable component at low frequency. The validity of the system described has been tested with simulations carried out in MATLAB/Simulink environment. Fig. 5.8.2 shows the evolution of the phase shift during the first 40ms of operation of the battery charger in response to a deviation of 10%, between the actual value of L_R and the nominal one. The plot shows that the tuning system is able to reset the phase shift between $_{SvT}$ and $_{SiT}$. The ripple superimposed on the signal is due to the high frequency components which remain in the output of low-pass filter in cascade to the XOR gate. The plot of the frequency of the power supply in response to this deviation is reported in Fig. 5.8.3 and shows that, for IIR, the supply frequency increases at steady-state of about 0.35%.

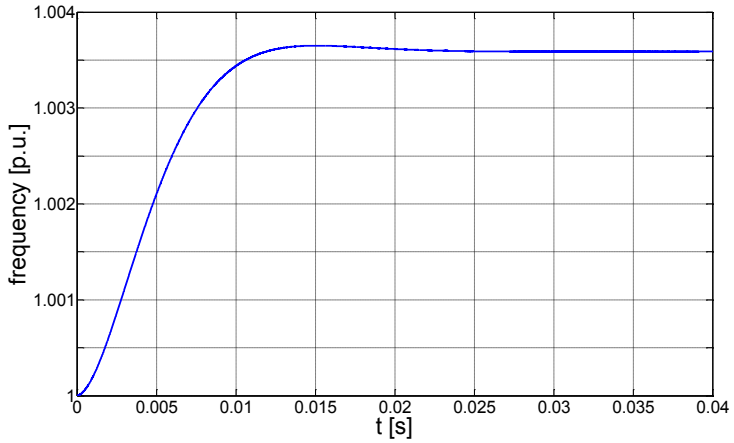

Fig. 5.8.3. Power source frequency during its tuning.

5.9. Conclusions

Based on the study of SS resonant WBC system and affect on efficiency and SIPSF due the deviation of reactive component three supply frequency update techniques are developed. Impact of these supply frequency update on efficiency and SIPSF is studied which outlines that

i). TSR is the worst supply frequency update among all.

ii). As far as efficiency is concern, RSR dominates over IIR under deviation of any reactive parameter.

iii). Regarding SIPSF factor, RSR performs slightly better under L_R and C_R deviations and a little worse under L_T and C_T deviations.

iv). considering practical implementation ease of RSR and IIR, IIR is found to be practically possible frequency update.

5.10 References

[1] Chih-Jung Chen, Tah-Hsiung Chu, Chih-Lung Lin, and Zeui-Chown Jou, "A Study of Loosely Coupled Coils for Wireless Power Transfer" *IEEE Transactions on Circuits and Systems - IT: Express Briefs*, vol. 57, no. 7, pp. 536-540, 2010.

[2] P. Li and R. Bashirullah, "A wireless power interface for rechargeable battery operated medical implants," *IEEE Trans. Circuits Syst. II, Exp. Briefs*, vol. 54, no. 10, pp. 912–916, Oct. 2007.

[3] R. R. Harrison, "Designing efficient inductive power links for implantable devices," in Proc. IEEE ISCAS, New Orleans, LA, USA, 2007, pp. 2080–2083.

[4] J. de Boeij, E. Lomonova, J. L. Duarte, and A. J. A. Vandenput, "Contactless power supply for moving sensors and actuators in highprecision mechatronic systems with long-stroke power transfer capability in x-y plane," *Sens. Actuators A, Phys*., vol. 148, no. 1, pp. 319–328, Nov.

[5] T. Bieler, M. Perrottet, V. Nguyen, and Y. Perriard, "Contactless power and information transmission," *in Conf. Rec. IEEE IAS Annu. Meeting*, 2001, vol. 1, pp. 83–88.

[6] C.Fernandez, O.Garcia, R.Prieto, J.Cobos, S.Gabriels, and G.Van Der Borght, "Design issues of a core-less transformer for a contact-less application," Proc. of. IEEE Applied Power Electronics Conference and Exposition, 2002, pp. 339-345.

[7] J. James, J. T. Boys, and G. A. Covic, "A variable inductor based tuning method for ICPT pickups," in Proc. IPEC, Nov. 29–Dec. 2, 2005, pp. 1142–1146

[8] G. A. Covic, J. T. Boys, A. M. W. Tam, and J. C. H. Peng, "Self tuning pick-ups for inductive power transfer," in Proc. Power Electronics Specialists Conference ,Rhoder , 2008 ,pp.3489-3494.

Chapter 6

Power supply for high power WBC system

6.1 Introduction

The past studies have mainly been focused on the low-medium power WBC system. While for public transport and quick charging, high power system is the recent demand in the WBC field. However, there are little investigations on high power applications and their implementation [1]-[5]. There are some literature, which deals with high power WPT system. A group of researchers from USA and Turkey has presented a 25 kW power supply system which convert three phase supply to single phase by means of two stage power conversion technique [6]. Single stage AC-AC power conversion technique eliminates the need of an additional AC-DC converter stage and hence reduces the size and cost of system [7]. A single-phase matrix converter based WBC system has been presented in [8]. However, a single-phase WBC system restricts the amount of power transfer due to the limitations of available input power consequently making the system less suitable for rapid charging/discharging of EVs. However, for high power applications, matrix conversion technique is used in [9] and [10] where low frequency three phase supply voltage is directly converted into high frequency single-phase output voltage.

Another solution for high power WBC is proposed in [11], [12], which present a novel parallel topology for WBC system. A parallel-connected system based on an LCL-T resonant converter module with soft-switching characteristics as described in [11] requires no additional reactive components for the parallelization and guarantees correct power sharing under normal operation conditions. However, due to a common DC link and full-bridge rectifier shared amongst all modules, a fault in one of the parallel units requires the whole system to shut down to prevent power backflow into the faulty unit. This effectively reduces the availability of the parallel supply by the number of parallel units, because connecting multiple power supplies in parallel increases the chance of potential system failure. One attractive feature of the proposed parallel topology in [12] is that it can operate continuously against a switch failure in one of the parallel units, thus maximizing the availability of the parallel power supply. The various solutions are investigated below.

6.2 Two stage power supply

In the conventional WBC system, power conversion at the transmitter stage takes place mainly in two stages. AC/DC converter is used as a first stage rectifier. DC obtained from this rectifier is further converted into desired amplitude and frequency. Diode or phase-controlled rectifiers (PCRs) are widely utilized in the front-end converter for the uncontrollable or controllable DC-bus voltage. This is mainly due to their simple topology and low cost. However, non-sinusoidal line currents are drawn from the AC source owing to a large electrolytic capacitor used on the DC link and low input power factor at low conduction angle which does not comply with IEEE-519 standard of low input current harmonics. Large size low frequency input filters are required in PCR to improve its power factor. This results in both, increased cost and large size of the PCR. PWM rectifiers have replaced the conventional

PCR due to their high efficiency, good voltage regulation, nearly unity power factor and small input/output filter size depending upon switching frequency. PWM rectifiers are normally operated at high switching frequency where low frequency harmonics are easily suppressed. PWM rectifiers are increasingly becoming popular due to the availability of high voltage, high current fast switching. Three phase PWM regenerative boost rectifier is shown in Figure 6.2.1. Output voltage is greater than the peak of the line to line RMS voltage in this rectifier. This is a four quadrant rectifier capable of bidirectional power flow. Operation of this rectifier is similar to boost switched-mode power supply (SMPS). When S_{1L} is turned on, voltage is applied across the inductor and it gets energized. When S_{1L} is turned off, inductor de-energizes through the diode of S_{1H} charging the capacitor. Unity power factor is achieved by controlling the current in the inductor. For the second stage of power supply, a conventional H-bridge inverter is used. In order to control the magnitude of the output voltage, either phase shift control or Pulse Width Modulation (PWM) technique is used. Due to high frequency operation of PWM inverter the parasitic elements establish an enormous stress on the circuit elements associated with a noticeable electromagnetic interference (EMI) emission. Use of phase shift control in H-bridge eliminates this issue associated with PWM technique. However, for high power application, use of a single H-bridge is very expensive due to its high power rating components. Resonant inverters, known to have distinct advantages of higher efficiency, higher power density, reduced EMI and lower component stresses, are a good choice in solving the abovementioned problem. Due to elimination of switching losses and stress in the power switches using natural commutation of the resonant converter, the operating frequency of the resonant converter can be made high, resulting in smaller values for the circuit elements and, hence, improving the power density of the power supply system.

As shown in Fig. 6.2.1 the supply system consists of input AC voltage source, three phase PFC boost converter, phase controlled three Class D inverters with a common series resonant circuits, three intercell transformers (ICTs), a wireless power link, impedance matching auto-transformer, full bridge current driven rectifier, and a battery [6]. Together with the operation of the circuitry in Fig. 6.2.1 the main focus of this section is to size the coupling coils and the inverter.

The impedance matching auto-transformer allows to optimize for the particular load and coupling factor without redesigning the wireless power link. The inductances of the PFC help to boost the input AC voltage and filter the input current, thus reducing the harmonic contents. The top and bottom set of switches are switched in a complementary fashion with a fixed dead band. Three class D inverters are connected in parallel to supply power to inductive link through three intercell transformers. Intercell transformers are designed to allow phase control and limit the circulating currents among switching legs. The output voltage of each class D inverter is a square wave due to its DC input voltage. Resonant currents $\overline{I}_1$, $\overline{I}_2$ and $\overline{I}_3$ at the switching legs outputs are sinusoidal due to the filtering action of resonant circuit. Since power is transferred only by the fundamental component of each input voltage so each input voltage sources can be replaced by a sinusoidal voltage sources v_1, v_2 and v_3 which represent the fundamental component.

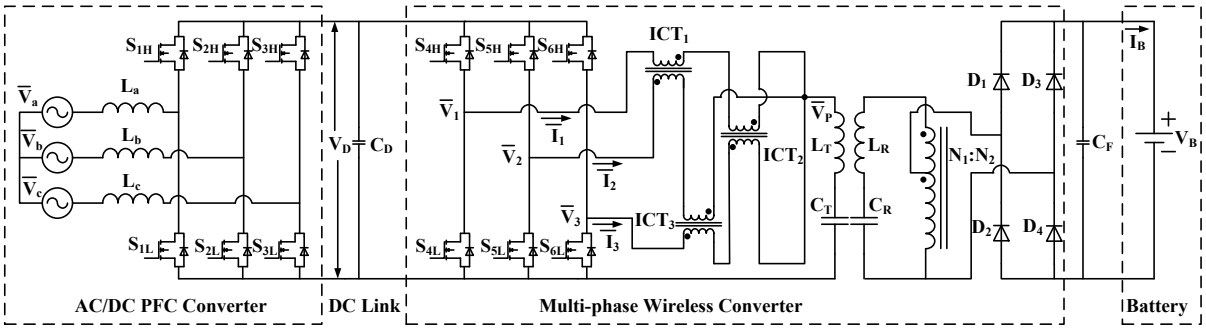

Fig. 6.2.1 Two stage high power WBC model.

The three ICTs are connected as shown in Fig. 6.2.2 where the secondary stage transformer and rectifier are replaced by the resistance R_L connected in series with receiver inductor. The intercell transformer in the transmitting stage provides equal current sharing between paralleled inverter legs. The fundamental components of the voltage sources in the circuit are

$$v_1 = V_m \sin(\omega t - \emptyset_1) \tag{6.2.1}$$

$$v_2 = V_m \sin(\omega t) \tag{6.2.2}$$

$$v_3 = V_m \sin(\omega t + \emptyset_2) \tag{6.2.3}$$

Here the amplitude V_m is given by

$$V_m = \frac{2}{\pi} V_D \tag{6.2.4}$$

and $\emptyset_1$ and $\emptyset_2$ are the phase shifts ranges from 0 to π. In the phasor domain the voltages at the input of intercell transformers can be expressed as

$$\overline{V}_1 = \frac{V_m}{\sqrt{2}} \mathrm{e}^{-j\emptyset_1} \tag{6.2.5}$$

$$\overline{V}_2 = \frac{V_m}{\sqrt{2}} \tag{6.2.6}$$

$$\overline{V}_3 = \frac{V_m}{\sqrt{2}} \mathrm{e}^{j\emptyset_2} \tag{6.2.7}$$

Equivalent circuit of ICTs from 6.2.2 is drawn in Fig. 6.2.3 where each ICT's self-inductances at primary and secondary sides are L_{1P} through L_{3P} and L_{1S} through L_{3S}, respectively. Assuming that all the windings have same self, leakage and mutual inductance represented as L_{self}, L_{leak} and L_M, equations for each phase can be written as

$$\begin{cases} \overline{V}_1 - j\omega L_{self}\overline{I}_1 + j\omega L_M \overline{I}_2 - j\omega L_{self}\overline{I}_1 + j\omega L_M \overline{I}_3 = \overline{V}_P \\ \overline{V}_2 - j\omega L_{self}\overline{I}_2 + j\omega L_M \overline{I}_1 - j\omega L_{self}\overline{I}_2 + j\omega L_M \overline{I}_3 = \overline{V}_P \\ \overline{V}_3 - j\omega L_{self}\overline{I}_3 + j\omega L_M \overline{I}_2 - j\omega L_{self}\overline{I}_3 + j\omega L_M \overline{I}_1 = \overline{V}_P \end{cases} \tag{6.2.8}$$

From (6.2.8) one can obtain the equation as in (6.2.9)

$$\frac{\overline{V}_1 + \overline{V}_2 + \overline{V}_3}{3} - \frac{2}{3} j\omega L_{leak}\left(\overline{I}_1 + \overline{I}_2 + \overline{I}_3\right) = \overline{V}_P \tag{6.2.9}$$

Expression for each phase current using (6.2.8) and (6.2.9) can be derived from as

$$\overline{I}_1 = \frac{1}{3}\left(\overline{I}_T + \frac{2\overline{V}_1 - \overline{V}_2 - \overline{V}_3}{2j\omega L_{leak}}\right) \tag{6.2.10}$$

$$\overline{I}_2 = \frac{1}{3}\left(\overline{I}_T + \frac{2\overline{V}_2 - \overline{V}_1 - \overline{V}_3}{2j\omega L_{leak}}\right) \quad (6.2.11)$$

$$\overline{I}_3 = \frac{1}{3}\left(\overline{I}_T + \frac{2\overline{V}_3 - \overline{V}_1 - \overline{V}_2}{2j\omega L_{leak}}\right) \quad (6.2.12)$$

Substituting $\frac{\overline{V}_1+\overline{V}_2+\overline{V}_3}{3}$ as $\overline{V}_S$, $\frac{2}{3}L_{leak}$ as L, and $\overline{I}_1 + \overline{I}_2 + \overline{I}_3$ as $\overline{I}_T$ the equivalent circuit of wireless power link is redrawn here again in Fig. 6.2.4.

Calculation of sizing power

Using the expressions developed in chapter three, Power source sizing power (PSSP), Receiving coil sizing power (RCSP) and Transmitting coil sizing power (TCSP) can be given as in (6.2.13), (6.2.14) and (6.2.15)

$$PSSP = \frac{V_L}{\omega M}\sqrt{(\omega M I_R)^2 + \left(\frac{L}{M}V_L\right)^2} \quad (6.2.13)$$

$$TCSP = \frac{V_L}{\omega M}\sqrt{(\omega M I_R)^2 + \left(\frac{L_T}{M}V_L\right)^2} \quad (6.2.14)$$

$$RCSP = I_R\sqrt{(\omega L_R I_R)^2 + V_L^2} \quad (6.2.15)$$

Sizing power of inverter (SPI):

$$SPI = \overline{V}_1\overline{I}_1^* + \overline{V}_2\overline{I}_2^* + \overline{V}_3\overline{I}_3^* \quad (6.2.16)$$

Substituting (6.2.10), (6.2.11) and (6.2.12) into (6.2.9) SPI can obtain as

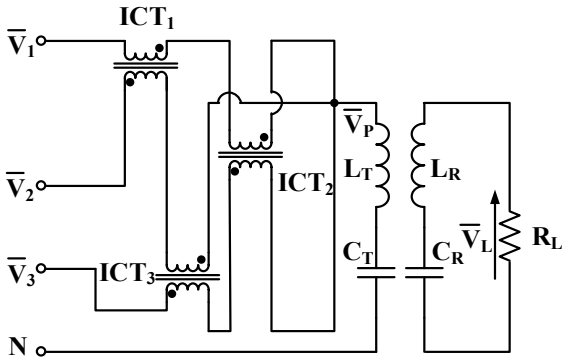

Fig. 6.2.2 Circuit diagram of wireless power link with series resonant circuit Compensations on both sides.

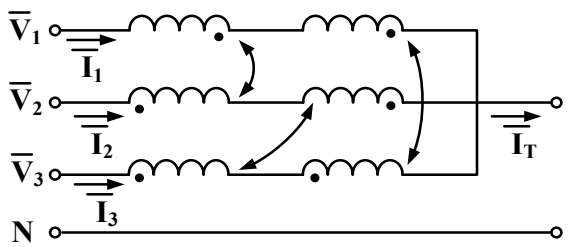

Fig. 6.2.3 Equivalent circuit of the intercell transformer

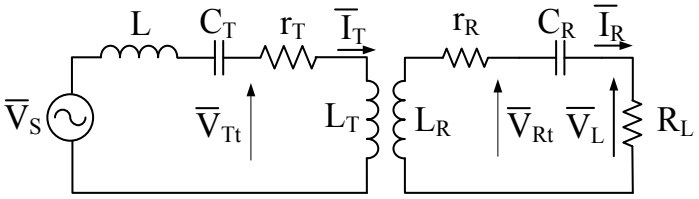

Fig. 6.2.4 The equivalent circuit of wireless power link.

$$SPI = \overline{V}_S \overline{I}_T^* + j\frac{V_M^2}{\omega L_{leak}} + \frac{4}{3}\frac{V_M^2}{\omega L_{leak}} cos\frac{\emptyset_1}{2} cos\frac{\emptyset_2}{2} sin\frac{\emptyset_1+\emptyset_2}{2} \qquad (6.2.17)$$

6.3 Single stage power supply

The development of new methods and circuits for electrical energy conversion with improved characteristics is a basic way for increasing of the energy efficiency of power electronic converters with respect to mains network. The single stage or matrix converters realize a direct conversion of alternating current-to-alternating current. The matrix converter is an AC-AC power converter topology based mainly on semiconductor switches with minimal requirements for passive components. It consists of a matrix of bi-directional switches arranged such that any input phase can be connected to any output phase. The matrix converter offers many potential benefits to the conventional power converter. It will not be the best solution for all uses but it offers significant advantages for many different applications. Indeed, matrix converter is a key technology when high efficiency and reliability are required. The main building block of the matrix converter is the bidirectional semiconductor switch. Single device that can both conduct current in each direction and block voltage in both directions.

In general, the desirable characteristics of AC to AC converters are

1) Sinusoidal input and output wave forms with minimal higher order harmonics and no sub-harmonics.

2) Bidirectional energy flow capability,

3) Minimal energy storage requirements (minimal size reactive component),

4) A controllable power factor,

5) Operations in all four quadrants of the torque–speed plane due to the regenerative capability,

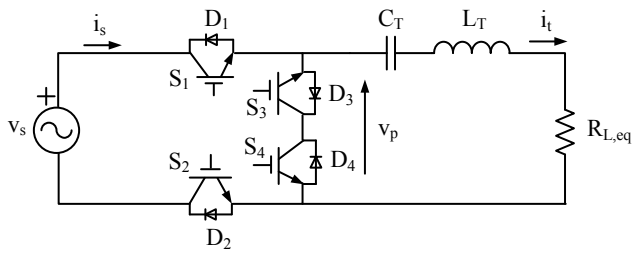

Fig. 6.3.1 Proposed single phase AC-AC converter

6) High reliability and long life due to the absence of bulky electrolytic capacitors,

7) Smaller and lighter design than other regeneration inverter with equivalent power ratings.

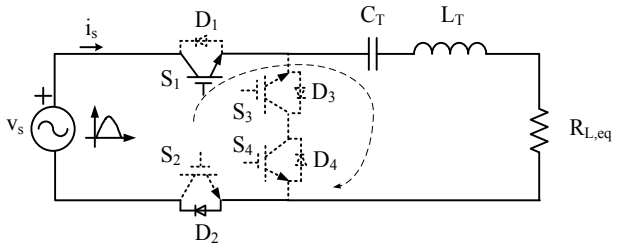

(a) Mode I

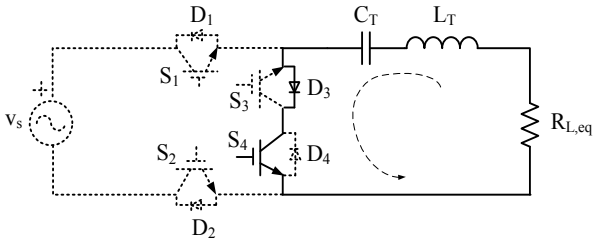

(b) Mode II

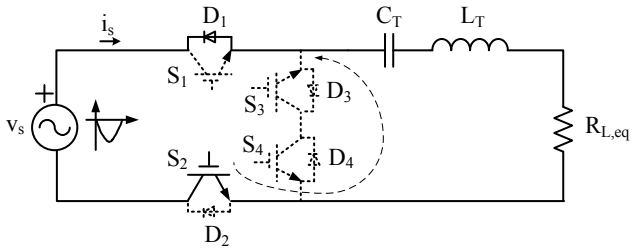

(c) Mode III

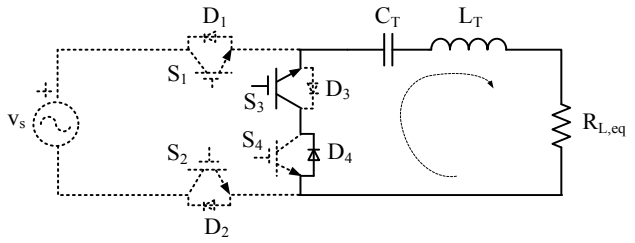

(d) Mode IV

Fig. 6.3.2 Switching operation of the AC-AC converter

The input filter designs should guarantee the near unity power factor operation at the power source side, to improve the main input current quality which has the sinusoidal waveforms with containing high harmonic components and to reduce the input voltage distortion which supplies to matrix converter module. Power factor improvement is an attractive challenge for the matrix converter which has been studied in detail in [13].

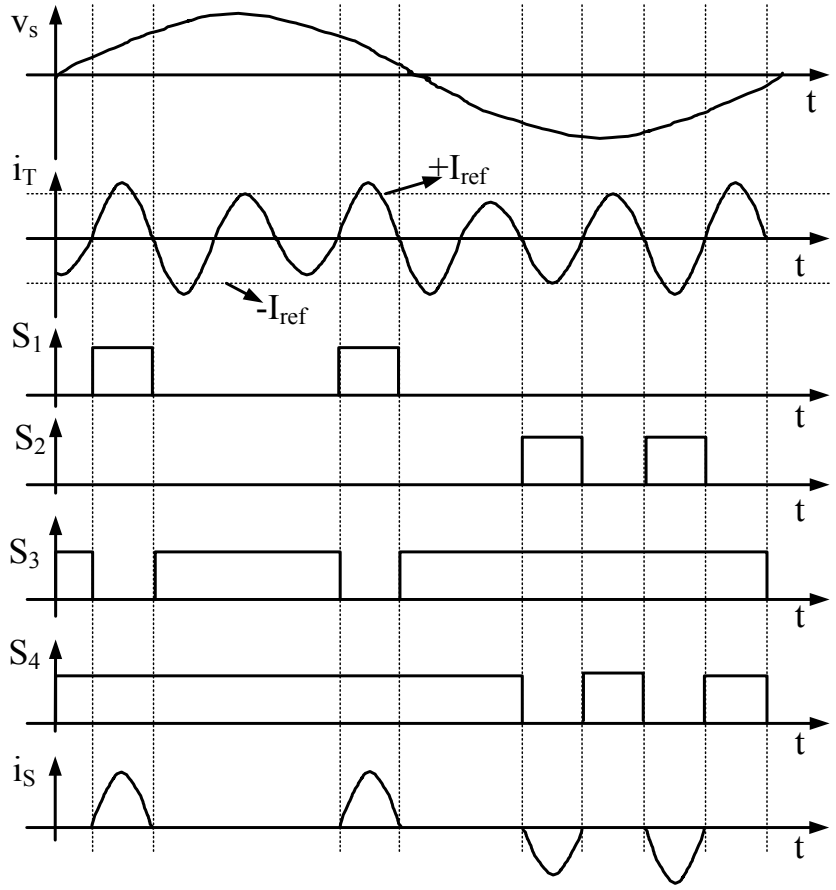

Fig. 6.3.3 Switching operation of direct AC-AC converter

6.3.1 Single phase AC-AC converter

Direct AC-AC power converter for a WBC system is shown in Fig. 6.3.1 [8]. It consists of an AC power supply, four semiconductor switches, and a series resonant circuit. Operation of the AC-AC converter is divided into four operating modes as shown in Fig. 6.3.2. The detailed operation status of all switches are shown in Table 6.1. A simplified current waveform of the converter with an AC input is shown in Fig. 6.3.3. It can be seen that if the peak value of the resonant current i_T is smaller than the designed reference value, switch S_1 is turned ON when $v_S > 0$ as shown in Fig. 6.3.2 (a), or S_2 is turned ON when $v_S < 0$ as shown in Fig. 6.3.2 (c), while S_3 and S_4 remain OFF. Consequently, the source voltage is applied to the resonant loop and the energy injected in each half-cycle of the resonant current. This results in a boost in the transmitting current. If current is larger than the reference value, switches S_3 or S_4 are turned ON depending on the positive or negative half cycle of current i_t while S_1 and S_2 are turned OFF as shown in Fig. 6.3.2 (b) and (c), such that the L_T–C_T–R_{eq} form a free oscillation circuit enabling the energy to cycle between the capacitor C_T and inductor L_T. In principle, if there are no power losses in the resonant tank ($R_{eq} = 0$), the circuit can oscillate infinitely without need of energy injection. However, in practice, power consumption always exists because of equivalent series resistors (ESRs) and the presence of any coupled load. When more energy is required, the resonant tank is connected to the power supply by the converting network.

Such an operation based on the discrete quantum energy injection and free oscillation is very different from normal converters. In consequence, the current is sensitive to the load condition and the polarity and phase of the input AC voltage. The line current (i_S) as can be seen from the Fig. 6.3.3, conducts only if either switch S1 or S2 is ON depending on the polarity of supply voltage. Current is not continuous and endures for a short duration. Due to which, line current has significant displacement factor as well as large harmonic content which as a result will lower the input power factor.

6.3.2 Single stage three phase AC-AC matrix converter

The single stage three phase AC-AC matrix converter is shown in Fig. 6.3.4 [9]. It consists of six reverse blocking switches and one regular switch (IGBT or MOSFET) in parallel with the resonant tank. Series connection of an IGBT or a MOSFET with diode can be used to build a reverse blocking switch, although reverse blocking switch is available in the market these days. Control strategy is based on the energy injection and free oscillation of the resonant circuit as already explained in section 6.3.1 for single phase AC-AC matrix converter. When resonant current is lower than the reference current, one switch among upper switches S_{A1}, S_{B1}, S_{C1} and one switch among lower switches S_{A2}, S_{B2}, S_{C2} are turned on in order to connect most positive and most negative input lines to the resonant tank. When resonant current is higher than the reference current all the reverse blocking switches are kept turned off and current freewheel through switch S_F or D_F during negative and positive half cycle of current i_T respectively.

6.3.3 Four switch matrix converter

Fig. 6.3.5 shows the WBC system which is driven by the four switch matrix converter-based topology [10]. Series compensation is provided for both stages of the WBC system. The proposed topology transforms 50-Hz three phase utility supply to a single-phase high-

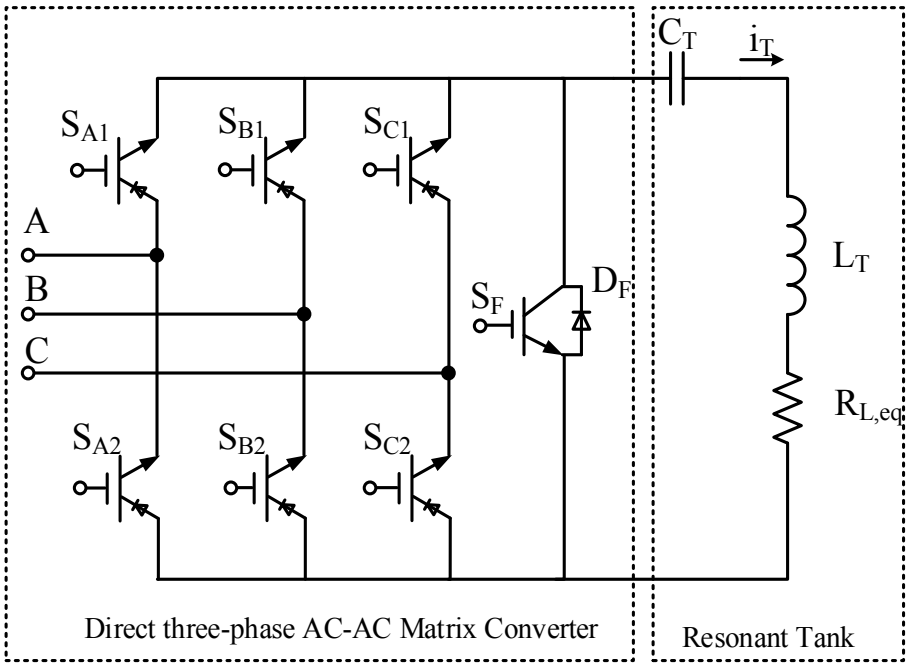

Fig. 6.3.4 Three phase to single phase matrix converter

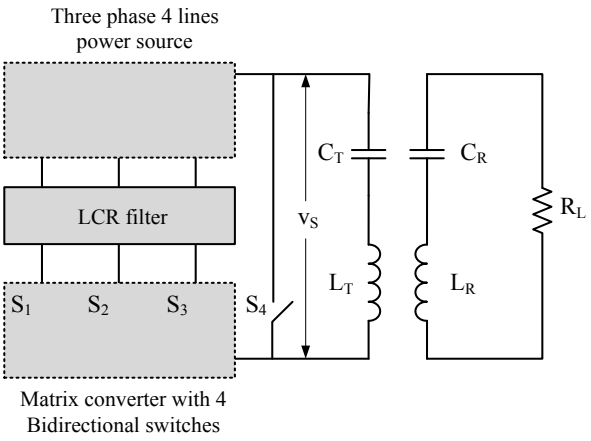

Fig. 6.3.5 Four switch matrix converter

frequency supply which in turn can be used to directly excite the transmitting stage resonant network of WBC system. In the proposed topology, a three-phase to single-phase matrix converter with only four bidirectional switches are employed to produce a high-frequency current in the transmitting stage series resonant tank. Switches S_1, S_2 and S_3 are used to connect either most positive or most negative voltage of the

three phase supply to the transmitting stage and fourth switch is added to control the resonant energy through a zero-voltage state across the resonant tank or v_S. The switching strategy is described in Fig. 6.3.6 where f^+ and f^- are the switching signals for most positive and most negative phase voltage. The basic switching rule is that only one bidirectional switch is switched on at any instant. The output voltage will be either equal to zero, or equal to one of three-phase voltages based on the switch selection among S1 to S4. In case the output voltage is equal to the phase voltage, it should be switched to the phase which is on the boundary of upper and lower voltage.

6.3.4 Three phase AC to three phase AC WBC system

As this converter converts three phase low frequency input voltage to three phase high frequency output voltage, it is called the three phase to three phase matrix converter. The working principle and detail investigation of this matrix converter can be found in [13], while this section focuses on its utility for single phase WBC system. The general scheme for this is shown in Fig. 6.3.7 which has three phase 60 Hz grid voltage as main supply, PFC circuit, matric converter, X-network and a SS resonant WBC system connected with two output phases of matrix converter. Use of only two phase while keeping the third phase open results into unbalance of the system. The stated problem of unbalance can be solved by using Steinmetz circuit [14] by using an X network as shown in Fig. 6.3.7. The X-network should not produce changes in the total active power absorbed from the load (which would mean further losses) and hence contains only reactive elements.

In further explanation, SS resonant system has been considered as a resistive load with the value of $\frac{(\omega M)^2}{R_{L,eq}}$. For the network shown in the Fig. 6.3.7 there are following set of equations for the admittance

$$\begin{cases} \dot{Y}_{RS} = G_{RS} - jB_{RS}^{\Delta} \\ \dot{Y}_{ST} = -jB_{ST}^{\Delta} \\ \dot{Y}_{TR} = -jB_{TR}^{\Delta} \end{cases} \tag{6.3.1}$$

where $G_{RS} = {1}\Big/{\frac{(\omega M)^2}{R_{L,eq}}}$ and B_{RS}^{Δ}, B_{ST}^{Δ} and B_{TR}^{Δ} are the susceptance of the delta connected X-network.

Phase voltages are

$$\begin{cases} \overline{V}_R = V \\ \overline{V}_S = Ve^{-j\frac{2\pi}{3}} = a^2V \\ \overline{V}_T = Ve^{j\frac{2\pi}{3}} = aV \end{cases} \tag{6.3.2}$$

where $a = e^{j\frac{2\pi}{3}}$ and V is the rms quantity. Expressions of Line voltages and currents can be obtained as in (6.3.3) and (6.3.4)

$$\begin{aligned} \overline{V}_{RS} &= \overline{V}_R - \overline{V}_S = V(1 - a^2) \\ \overline{V}_{ST} &= \overline{V}_S - \overline{V}_T = V(a^2 - a) \\ \overline{V}_{TR} &= \overline{V}_T - \overline{V}_R = V(a - 1) \end{aligned} \tag{6.3.3}$$

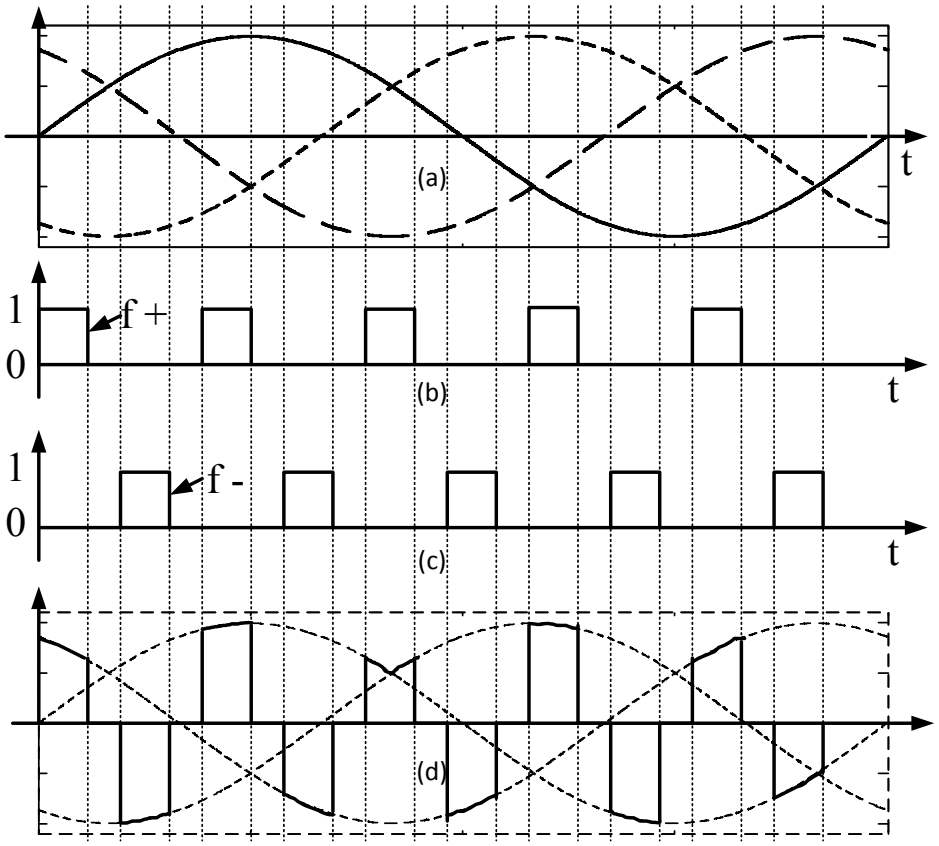

Fig. 6.3.6 Commutation strategy (a) three phase input voltage, (b) and (c) positive and negative side control signals (d) voltage v_p

$$\begin{aligned}\bar{I}_R &= \bar{I}_{RS} - \bar{I}_{TR} = \bar{V}_{RS}\dot{Y}_{RS} - \bar{V}_{TR}\dot{Y}_{TR}\\ \bar{I}_S &= \bar{I}_{ST} - \bar{I}_{RS} = \bar{V}_{ST}\dot{Y}_{ST} - \bar{V}_{RS}\dot{Y}_{RS}\\ \bar{I}_T &= \bar{I}_{TR} - \bar{I}_{ST} = \bar{V}_{TR}\dot{Y}_{TR} - \bar{V}_{ST}\dot{Y}_{ST}\end{aligned} \quad (6.3.4)$$

Substituting (6.3.1) and (6.3.3) in (6.3.4) gives line currents as in (6.3.5)-(6.3.7)

$$\bar{I}_R = V\left\{\left(\tfrac{3}{2}G_{RS} + \tfrac{\sqrt{3}}{2}B^{\Delta}_{RS} - \tfrac{\sqrt{3}}{2}B^{\Delta}_{TR}\right) + j\left(\tfrac{\sqrt{3}}{2}G_{RS} - \tfrac{3}{2}B^{\Delta}_{RS} - \tfrac{3}{2}B^{\Delta}_{TR}\right)\right\} \quad (6.3.5)$$

$$\bar{I}_S = V\left\{\left(-\tfrac{3}{2}G_{RS} - \tfrac{\sqrt{3}}{2}B^{\Delta}_{RS} - \sqrt{3}B^{\Delta}_{ST}\right) + j\left(-\tfrac{\sqrt{3}}{2}G_{RS} + \tfrac{3}{2}B^{\Delta}_{RS}\right)\right\} \quad (6.3.6)$$

$$\bar{I}_T = V\left\{\left(\tfrac{\sqrt{3}}{2}B^{\Delta}_{TR} + \sqrt{3}B^{\Delta}_{ST}\right) + j\left(\tfrac{3}{2}B^{\Delta}_{TR}\right)\right\} \quad (6.3.7)$$

Necessary and sufficient condition for the three phase currents to form a balanced set is the cancellation of the negative sequence current component given as

$$\bar{I}^{-} = \tfrac{1}{3}(I_R + a^2 I_S + aI_T) \quad (6.3.8)$$

Putting the cancellation conditions for the real and imaginary parts of $\bar{I}^{-}$ obtained by substituting (6.3.5)-(6.3.7) in (6.3.8) we obtain the conditions as

$$B^{\Delta}_{TR} - B^{\Delta}_{RS} = \tfrac{G_{RS}}{\sqrt{3}} \quad (6.3.9)$$

$$B^{\Delta}_{RS} - 2B^{\Delta}_{ST} + B^{\Delta}_{TR} = \sqrt{3}G_{RS} \quad (6.3.10)$$

According to a criterion, in addition to load balancing, X-network should also lead to cancellation of the reactive power absorbed from the network on the positive sequence. This is equivalent to the additional condition as

$$Im(\bar{I}^{+}) = 0 \quad (6.3.11)$$

where $\bar{I}^{+}$ is the positive sequence component corresponding to the load current of the ensemble load and X network. $\bar{I}^{+}$ can be given as

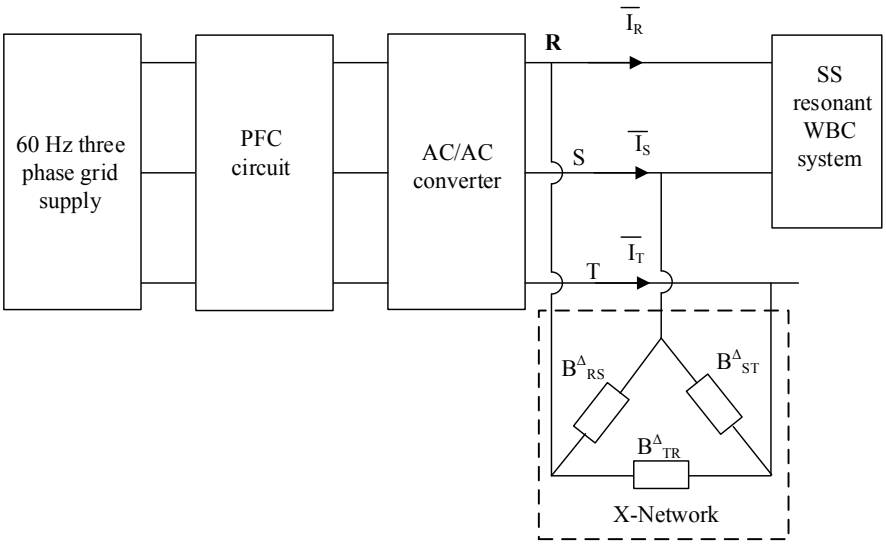

Fig. 6.3.7 Three phase to three phase WBC system

$$\overline{I}^{+} = \frac{1}{3}\left(\overline{I}_R + a^2\overline{I}_T + a\overline{I}_S\right) \tag{6.3.12}$$

Substituting (6.3.5)-(6.3.7) to (6.3.12) gives

$$\overline{I}^{+} = \overline{I}_R \tag{6.3.13}$$

Putting the imaginary part of (6.3.5) equal to zero gives

$$B_{RS}^{\Delta} + B_{TR}^{\Delta} = \frac{1}{\sqrt{3}}G_{RS} \tag{6.3.14}$$

Solving equations (6.3.9), (6.3.10) and (6.3.14) gives

$$\begin{cases} B_{RS}^{\Delta} = 0 \\ B_{TR}^{\Delta} = \frac{1}{\sqrt{3}}G_{RS} \\ B_{ST}^{\Delta} = -\frac{1}{\sqrt{3}}G_{RS} \end{cases} \tag{6.3.15}$$

It is clear from (6.3.15) that branches ST and TR of X-network are capacitor and inductor respectively, where values of capacitance and inductance are $G_{RS}/\sqrt{3}\omega$ and $\sqrt{3}/\omega G_{RS}$ respectively.

The supply power of converter (SPC) can be evaluated as

$$SPC = \overline{V}_{RS}\overline{I}_{RS}^{*} + \overline{V}_{ST}\overline{I}_{ST}^{*} + \overline{V}_{TR}\overline{I}_{TR}^{*} \tag{6.3.16}$$

Substituting (6.3.3)-(6.3.7) and (6.3.15) to (6.3.16) gives

$$SPC = 3V^2G_{RS} \tag{6.3.17}$$

which is real power supplied by a three phase system.

6.4 Parallel topology of power supply

Another solution for high power WBC supply scheme is the parallel connection of more than one power supplies. Parallel power supply has following characteristics:

i) Equal power sharing among parallel-connected inverters.

ii) In order to make high power supply system without using parallel topology it is needed to redesign the complete power supply, which is a time consuming and expensive process. In contrast connecting different numbers of power supply module in parallel reduces the design time and cost.

iii) Since heat generated is more distributed in parallel topology it simplify the thermal design of power supply.

iv). Compared to single power supply, a parallel power supply of the same power level need low power rating component which are normally lower cost and easier to realize.

A detailed view of single transmitter stage power supply system is shown in Fig. 6.4.1. It comprises a full-bridge rectifier, a DC-bus capacitor, a full H-bridge, and an LCL-T resonant tank. The LCL-T resonant tank consists of a DC blocking capacitor C_b, a parallel capacitor C_T, a track inductor L_T, a transformer T, and its leakage inductance L_b. It acts as a

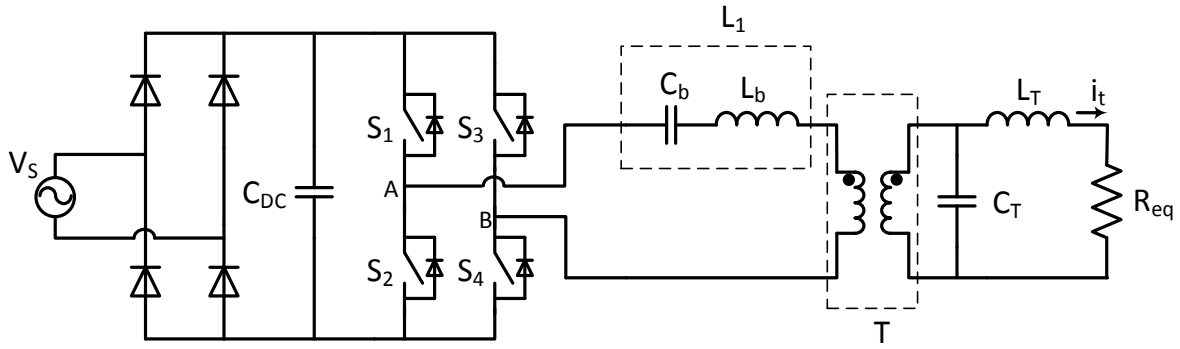

Fig. 6.4.1 Single transmitter stage power supply system

bandpass filter, passing only the fundamental component of the H-bridge voltage to the track inductor; all the higher order harmonics are trapped in a loop consisting of the H-bridge, L_1, T, and C_T. For safety reasons, transformer T is desired to isolate the mains input voltage from the LCL-T resonant tank in the case of failure. Its turns ratio can also be used advantageously for adjusting the magnitude of the H-bridge output voltage and the track current for a given H-bridge output voltage. The receiver for the considered power supply is assumed to be series resonating and referred here as R_{eq}.

The first inductor L_1 of the LCL-T network is formed by L_b and C_b. The leakage inductance L_b of the transformer T is deliberately designed to be larger than the required value of L_1, and the extra inductance is tuned out by C_b. C_b eliminates any DC component in the H-bridge output voltage, preventing transformer saturation. Therefore, the value of L_1 can be expressed as

$$L_1 = \left(j\omega L_b + \frac{1}{j\omega C_b}\right)/j\omega \tag{6.4.1}$$

The track current $\overline{I}_T$ can be expressed in phasor notation as

$$\overline{I}_T = \frac{\overline{V}_{AB}}{j\omega L_1 + \left(R'_{eq} + j\omega L'_T\right) \times \left(1 - \omega^2 L_1 C'_T\right)} \tag{6.4.2}$$

Here, R'_{eq}, L'_T and C'_T are the reflected values of R_{eq}, L_T, and C_T looking into the primary side of T. If the reactance of L_1 is made equal to that of C'_T at the resonant frequency, the track current in (6.4.2) can be simplified as

$$\overline{I}_T = \frac{\overline{V}_{AB}}{j\omega L_1} \tag{6.4.3}$$

This result indicates that, the track current of a tuned LCL-T network is independent of variations in R_{eq} and L_T, and is only controlled by the values of V_{AB} and L_1 [12]. This property significantly simplifies the control and regulation of the track current and power.

The impedance seen from terminal AB is

$$Z_{AB} = \frac{j\omega L_1\left(1 - \omega^2 L'_T C'_T\right) + R'_{eq}}{\left(1 - \omega^2 L'_T C'_T\right)^2 + \left(\omega C'_T R'_{eq}\right)^2} \tag{6.4.4}$$

An LCL-T network is tuned if the reactance of L_1, C'_T, and L'_T are all identical at the resonant frequency

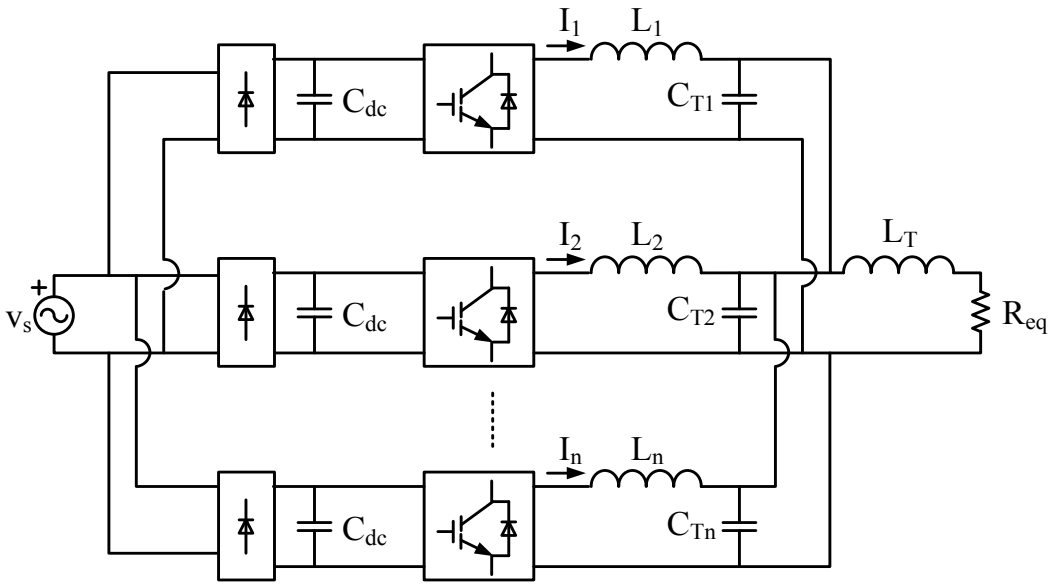

Fig. 6.4.2 Parallel connection of parallel LCL-T inverters

$$\omega L_1 = \frac{1}{\omega C_T'} = \omega L_T' \tag{6.4.5}$$

Under this condition, the H-bridge impedance becomes purely resistive

$$Z_{AB} = \frac{(\omega L_1)^2}{R_L'} \tag{6.4.6}$$

This is the most efficient operating point for the power supply, as the H-bridge does not need to supply any reactive power.

A parallel power supply using existing power supplies is shown in Fig. 6.4.2. The parallel connection is made across the power supply on the AC side. It uses a low energy DC bus and operates at the resonant frequency of the LCL network. In addition, each parallel unit has its own input full bridge rectifier. One attractive feature of the proposed parallel topology is that it can operate continuously against a switch failure in one of the parallel units, thus maximizing the availability of the parallel power supply.

The parallel connection is made across the transmitting inductor L_T. With this configuration, all parallel units share a common transmitting inductor, parallel capacitor, reflected load and input power supply. The value of the DC bus capacitor for each parallel unit is unchanged in order to retain unity input power factor. To preserve the desirable characteristics of the LCL-T network the value of L_T in an N parallel system is N times smaller than that of a single unit this is equivalent to placing N transmitting inductor in parallel.

6.5 Conclusions

In this chapter different high power supply systems are reviewed which are categorized as two stage power supply, single stage power supply and parallel topology for power supply. Advantages and disadvantages associated with all the power supply systems are discussed and explained briefly along with their operating principle.

6.6 References:

[1] M. Bojarski, E. Asa, and D. Czarkowski, “Three Phase Resonant Inverter for Wireless Power Transfer,” IEEE Wireless Power Transfer Conference (WPTC), May 2015, pp.1-4.

[2] J.F. Sanz, J.L. Villa, J. Sallan, J.M. Perie, and L.G. Duarte, “UNPLUGGED Project: Development of a 50 kW Inductive Electric Vehicle Battery Charge System,” EVS27 Electric Vehicle Symposium and Exhibition, pp.1-7, Nov. 2013.

[3] I. Fujita, T. Yamanaka, Y. Kaneko, S. Abe, and T. Yasuda, “A 10kW Transformer with A Novel Cooling Structure of A Contactless Power Transfer System for Electric Vehicles,” IEEE Energy Conversion Congress and Exposition, Sep. 2013, pp.3643-3650.

[4] J.H. Kim, B.S. Lee, J.H. Lee, S.H. Lee, C.B. Park, S.M. Jung, S.G. Lee, K.P. Yi, and J. Baek, “Development of 1-MW Inductive Power Transfer System for a High-Speed Train,” *IEEE Transactions on Industrial Electronics*, vol. 62, no. 10, pp.6242-6250, Oct. 2015

[5] M. Jurjevich, “Large-Scale, Commercial Wireless Inductive Power Transfer (WPT) for Fixed Route Bus Rapid Transportation”, IEEE Transportation and Electrification Newsletter, Oct. 2014.

[6] M. Bojarski, E. Asa, K. Colak, and D. Czarkowski, “A 25 kW Industrial Prototype Wireless Electric Vehicle Charger,” Proc. of IEEE Applied Power Electronics Conference and Exposition (APEC), 2016, pp. 1756-1761.

[7] P.W. Wheeler, J. Rodríguez, J.C. Clare, L. Empringham, and A. Weinstein, “Matrix Converters: A Technology Review,” *IEEE Transaction on Industrial Electronics*, Vol. 49, no. 2, pp. 276-288, April 2002.

[8] H.L. Li, A.P. Hu, and G.A. Covic, “A Direct AC–AC Converter for Inductive Power-Transfer Systems,” *IEEE Transaction on Power Electrocics*, vol. 27, no. 2, pp. 661-668, Feb. 2012.

[9] M. Moghaddami, A. Anzalchi, and A.I. Sarwat, “Single-Stage Three-Phase AC-AC Matrix Converter for Inductive Power Transfer Systems,” IEEE Transaction on Industrial Electronics, Vol. no. 99, pp. 1-1.

[10] N.X. Bac, M. Vilathgamuwa, and U.K. Madawala, “A SiC-Based Matrix Converter Topology for Inductive Power Transfer System,” IEEE Transaction on Power Electronics, vol. 29, no. 8, pp. 4029-4038, August 2014.

[11] A. Schonknecht and R.W.A.A.De Doncker, “Novel Topology for Parallel Connection of Soft-Switching High-Power High-Frequency Inverters,” IEEE Transaction on Industry Application, Vol. 39, no. 2, pp. 550-555, Mar/Apr. 2003.

[12] H. Hao, G. Covic, M. Kissin, and J. Boys, “A parallel topology for inductive power transfer power supplies,” Proc. of IEEE Applied Power Electronics Conference (APEC), 2011, pp. 2027-2034.

[13] Huu-Nhan Nguyen, Tuyen D. Nguyen, and Hong-Hee Lee, “A Modulation Strategy to Eliminate CMV for Matrix Converters with Input Power Factor Compensation,” Proc. of IEEE Industrial Electronics Society (IECON), 2016, pp. 6237-6242.

[14] A. Pană, „Active Load Balancing in a Three-Phase Network by Reactive Power Compensation”, Chapter 11 in "Power Quality Monitoring, Analysis and

Enhancement", edited by A. Zobaa, M.M. Canteli and R. Bansal, InTech Europa, open access publisher, Rijeka, Croatia, 2011.

Chapter 7

Coil for WBC systems

7.1 Introduction

Coils for the WBC system need to fulfil several requirements to enable practical application on the EVs. They should have good characteristics like, ground clearance and fitting, able to operate with a large air gap (~150-200mm), thermal stability, lightweight to minimize vehicle energy requirements and have good tolerance to misalignment to allow easier parking. It is of great importance to shape coil that will maximize power transfer over the desired range of air gap and misalignment, while at the same time complying with all the safety standards and regulations. A large number of design options have been proposed for the WBC coil geometry. An intuitive classification based on the polarized and non-polarized coil along with the concept of DD coil is presented in this chapter. Later on, a track of DD coils has been analyzed with the help of FEM tool.

7.2 Types of Coil structure

The lumped magnetic coil designs used in WBC are generally categorized on their ability to generate or couple only the parallel, perpendicular or both components of flux entering or leaving the coil surface. In addition, some publications highlight the polarized or non-polarized nature of flux generated by a coil design as well. A non-polarized coil design ideally generates and couples a flux pattern that is symmetric around the center of the coil, but the term is still used for the coil designs where the fields are directionally symmetric around the coil center though the strength of the field might be different along different angles around the center. On the other hand a polarized coil generates and couples a flux pattern in which the flux flows dominantly along one dimension of the coil only, i.e., either length or width of the coil. As per these definitions the lumped coil topologies found in the literature that are designed to generate and couple only the perpendicular component of flux are generally non-polarized [1] in nature while the ones designed to couple only the parallel component of flux are polarized [2] in nature.

7.2.1 Non- polarized Coils

Typical shapes of non-polarized coil includes circular, square, and rectangular structures. In order to compare the magnetic coupling obtained from the different coil shapes, a 3-D FE tool was used to construct models of a circular, a square, and a rectangular coil geometry in different sizes [3], [4]. A circular coil geometry offers higher magnetic coupling for a given coil area, which results in higher transmission efficiency with the same area related power density of the WBC coil. This is due to the distortion of the field around the corners of the square and the rectangular coil shape. However, in the practical application, depending on the aspect ratio of the available space a rectangular coil might be preferable over a circular shape to enclose a significantly larger area. Earlier in the 2000, non-polarized magnets normally in the shape of a circular design were the most common topology used for EV charging. New designs use ferrite spokes as shown in Fig. 7.2.1 (a) [5], where a circular

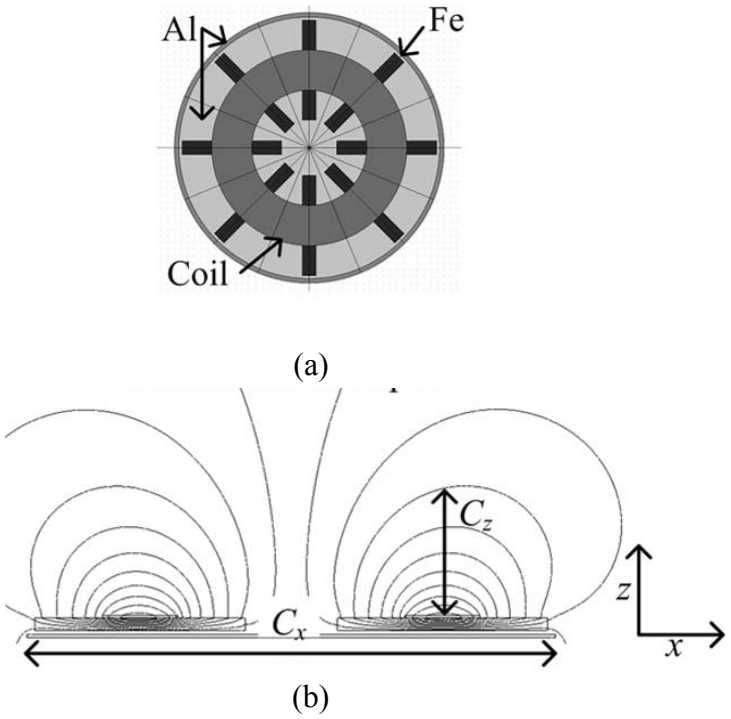

Fig. 7.2.1. (a) Layout of a circular coil and (b) Flux line on a cross section of a circular coil

coil laying on the ferrite core bar with aluminum sheet placing beneath the coil and core is drawn.

In order to obtain a desirable coupling coefficient of ~0.2 with air gaps in the range of 150–250 mm, the diameter of a circular coil needs to be increased significantly. The relationship between the size of a coil and its ability to lob flux to a receiver coil placed above it can be explained using the concept of fundamental flux path height as shown in Fig. 7.2.1.(b), where C_z and C_x are the fundamental flux path height and coil diameter respectively. It is found that C_z is roughly proportional to one quarter of the coil diameter (C_x/4) which result into large diameter of coil for good coupling with a large air gap. For an example, if the 700-mm coil is required to have a k of 0.2 at 200 mm instead of 175 mm, the diameter must be increased by an amount proportional to four times the increase in vertical height. This makes the system based on circular coils impractical with large air gaps or higher power levels that are necessary for shorter charge times.

7.2.2 Polarized Coils

Solenoidal coil

Polarized coils were first developed and used for monorail automatic guided vehicle (AGV) applications in the 90's and also used for EV charging application in Whakarewarewa (New Zealand). Subsequently, several polarized solenoidal coils were investigated and developed with the improvements in the mid 2000's based on shaped bar ferrites. Such coils have a well-defined north and South Pole created by wrapping a flat coil around a flat ferrite structure as such these coils are essentially flattened solenoids. The distance between the end north and south poles and the size of the poles are each carefully designed based on application. An example of this is shown in Fig. 7.2.2 (a) where the two coils are connected magnetically in series (flux from one coil passes through the other) and electrically in parallel,

to lower the inductance seen by the power supply. The portion of ferrite through which main flux (Φ_{ip}) passes is the flux pipe. An advantage of using flux pipe is that the fundamental flux path height F_{Pz} in Fig. 7.2.2 (b) is approximately half the length of the coil ($F_{Px}/2$). The wings on a flux pipe as shown in Fig. 7.2.2 (b) helps to launch the flux to the receiver coil, improving tolerance to horizontal misalignment. Coils based on flux pipes with length F_{Px} have improved coupling over circular designs of the same size ($C_x = F_{Px}$).

An issue with the designs, as presented in [6], [7] is that the flux pipe produces a two-sided flux path, as shown in the cross section of Fig. 7.2.2 (b). The amount of flux coming out of the front of the coil is similar to that coming out of the back, resulting in a significant drop in efficiency when aluminum is used to block the flux behind the coils.

7.3 Double D or DD coil

An upgraded new polarized single-sided flux coil [4], [8] is shown in Fig. 7.3.1. The shaded portion is considered to be a flux pipe between coils a and b because the coils are magnetically in series (shown by Φ_{ip}) and electrically in parallel. The coils are positioned on the ferrite base, which reflect the flux upward, giving no way to flow the flux through the back of coil. This allows magnetic material to be placed underneath with little impact on quality factor Q, creating a truly single-sided flux coil. The height of the intra-coil flux (Φ_{ip}) can be controlled by adjusting the width of the flux pipe. Therefore, section of coils forming the flux pipe should be made as long as possible. Conversely, the remaining length of the coil should be minimized to save copper and lower the coil resistance. Doing so results in coils shaped like a “D” and since there are two of such coils placed back to back, the coil is

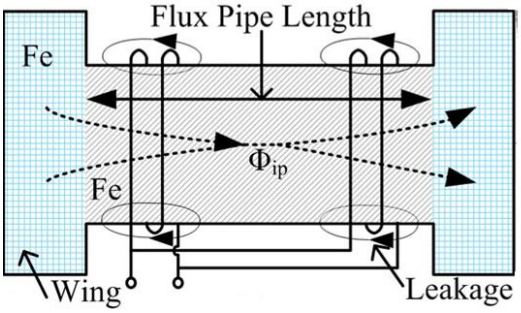

(a)

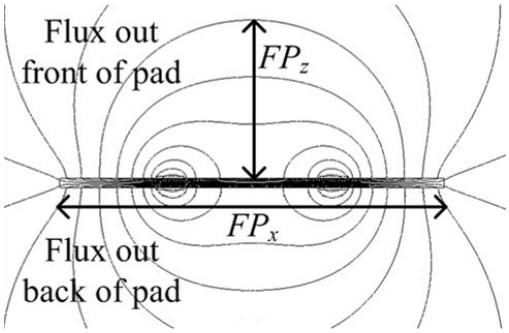

(b)

Fig. 7.2.2. (a) Flux pipe schematic. (b) Flux lines about a flux pipe.

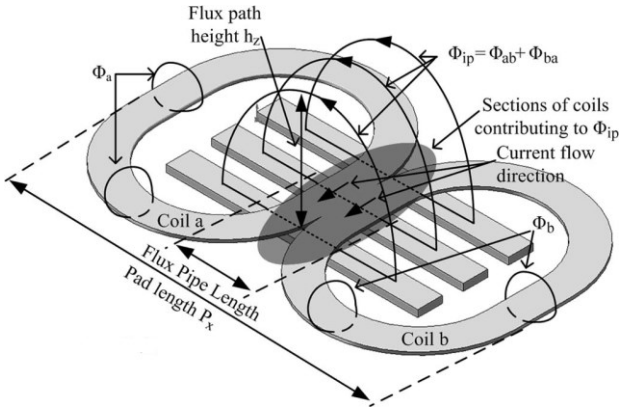

Fig. 7.3.1. Simplified model of a DD coil with flux components Φa, Φb, and Φip, produced by coils a and b and mutual coupling between coils, respectively.

referred to as a double D or DD. The current flow within the flux pipe must be in the direction to ensure that Φ_{ip} has a height that is proportional to half a coil length. The DD topology has highly desirable characteristics for a large air gap inductive coil.

Advantages of DD coil are: single-sided flux paths, an average flux path height that is proportional to half of the length of the coil, insensitivity to aluminum shielding, and a low leakage flux out of the back.

7.4 Multi-coil Polarized coils

As a receiver (vehicle) coil, DD coil can only couple horizontal flux components when centered on a primary, whereas circular or rectangular pads can only couple vertical flux components when centrally aligned. A new class of multi-coil pads were constructed which are sensitive to both vertical and horizontal flux components at any point in space (although because of their design they are also polarized). Two of the most commonly known Multi-coil designs called the DD quadrature (DDQ) and Bipolar are shown in Figs. 7.4.1 and 7.4.2. Such coils have been successfully used to increase power transfer and tolerance to lateral offset in track-based systems with either travelling or stationary magnetic fields. Excepting the truth that multi-coil has better misalignment performance than the DD one they have their own limitation such as DDQ need separate power supply for extra quadrature coil while Bipolar coil has low voltage gain due to lower value of *M*. Without going into the deep investigation

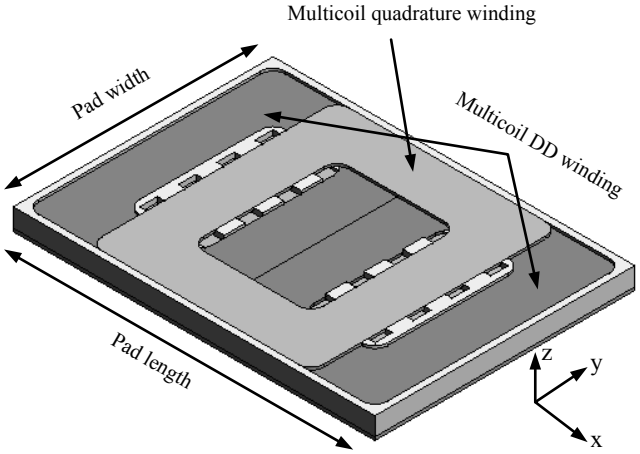

Fig. 7.4.1. Multi-coil with independent windings DDQ

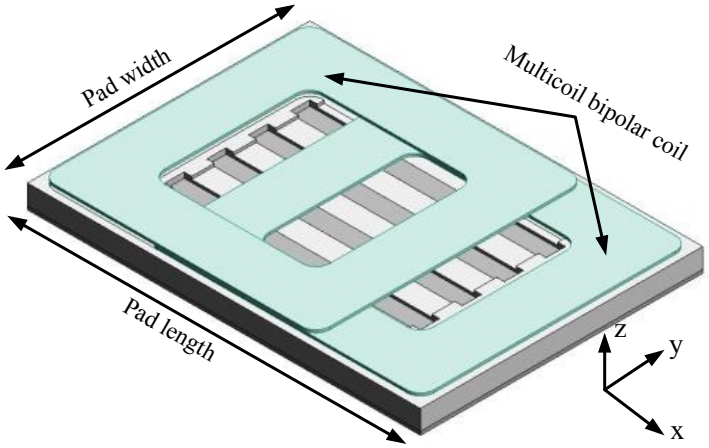

Fig. 7.4.2. Multi-coil with independent bipolar windings

of DDQ and Bipolar coils this chapter has proceeded with DD coil.

7.5 FEM Simulation tool

The finite element method (FEM) is a numerical technique for finding accurate solutions to boundary value problems for partial differential equations. It is also referred to as finite element analysis (FEA). It subdivides a large problem into smaller, simpler parts that are called finite elements. The simple equations that model these finite elements are then assembled into a larger system of equations that models the entire problem. FEM then uses variational methods from the calculus of variations to approximate a solution by minimizing an associated error function.

A typical work out of the method involves two steps. First step is to divide the domain of the problem into a collection of subdomains, with each subdomain represented by a set of element equations to the original problem. Second step comprises systematically recombining all sets of element equations into a global system of equations for the final calculation. The global system of equations has known solution techniques, and can be calculated from the initial values of the original problem to obtain a numerical solution.

FEM Tools

There are numerous software packages available that implement the finite element method for solving partial differential equations. These software are dedicated to perform various kinds of analysis like electromagnetic, thermal, material structures, flued-dynamic analysis etc.; amongst them our interest is electromagnetic analysis. In this way JMAG-Designer tool has been used in the research work of this thesis. To create a geometry, an additional tool ‘Geometry Editor’ is used which can be launched from the JMAG-Designer window. Fig. 7.5.1 show the track of three transmitter DD coils design made in JMAG editor tool.

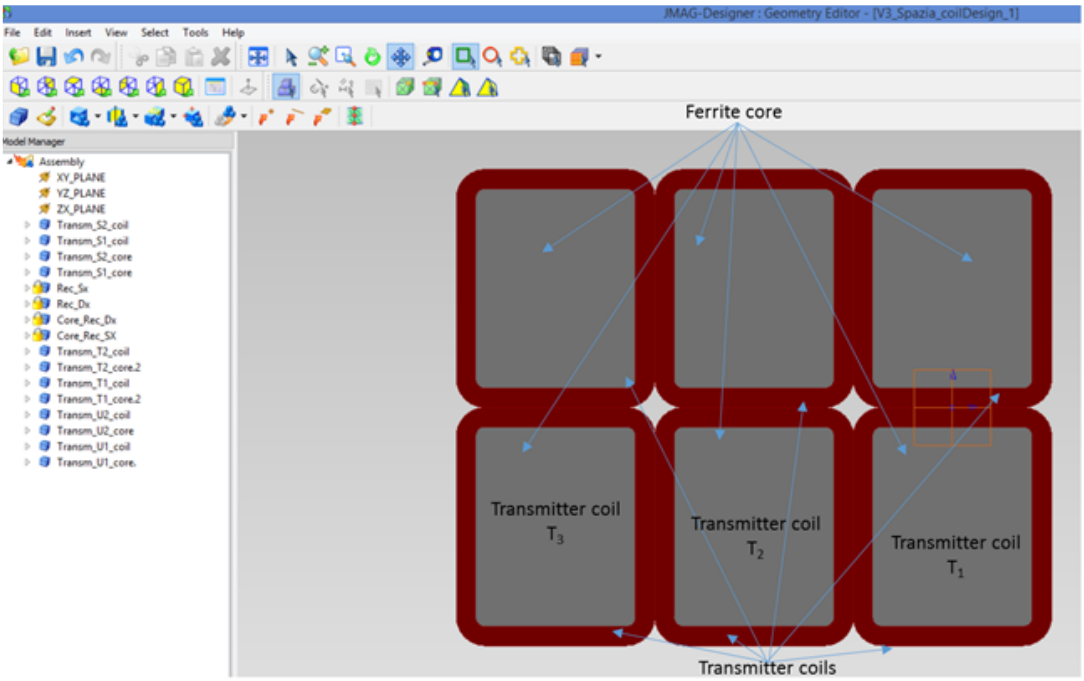

Fig. 7.5.1. JMAG Model of WBCP coil model.

In second stage, the geometry is imported into the project manager of JMAG-Designer as shown in Fig. 7.5.2, and FEM study is allotted. Various types of FEM studies can be performed on the imported model like magnetic, electric, thermal, structural etc., however, as for this thesis, the magnetic study of a WBC system is of interest.

An electrical circuit can be created or imported as an important input to carry out the FEM analysis, because the defined conditions to the electrical components need supply, connections and ground. The circuit components need to be linked with the test conditions. There are some passive components available in the circuit editor which makes JMAG independent simulation environment. Fig. 7.5.3 shows an electrical scheme in circuit editor.

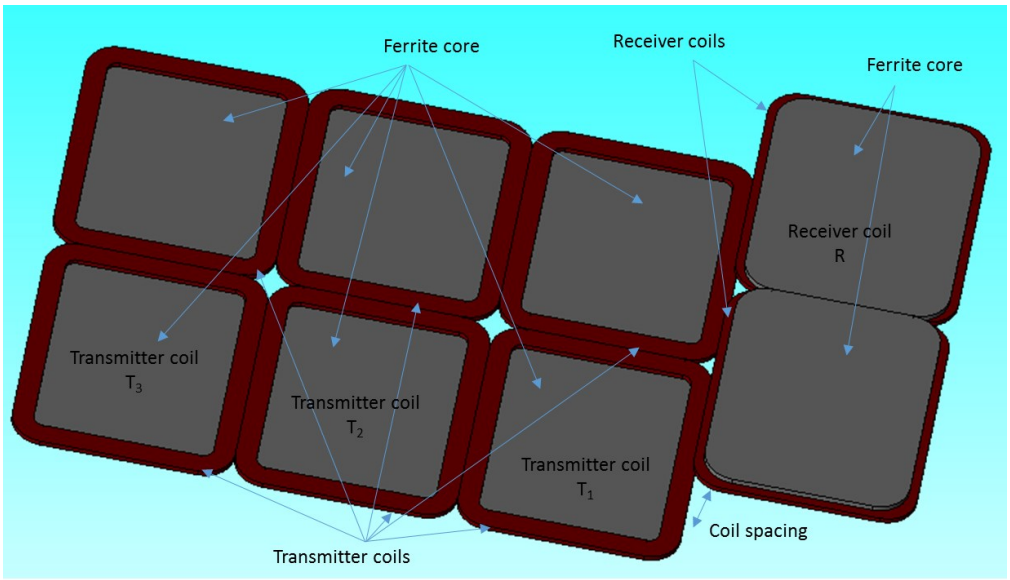

Fig. 7.5.2. JMAG Model of DD coil.

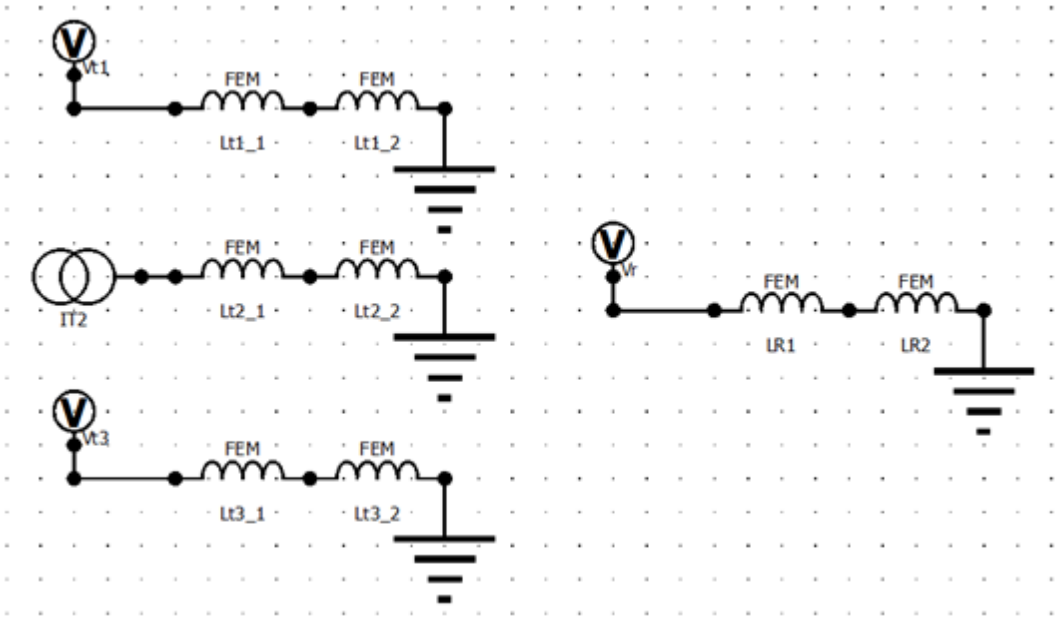

Fig. 7.5.3. Electrical schematic in JMAG Circuit Editor.

In this way, a set of DD coil is created in JMAG. In JMAG magnetic study, there are three types of analysis options available: static, transient and frequency analysis. In order to evaluate the magnetic properties of a coupler like self and mutual inductances (*L* and *M*), flux density, current density etc., the frequency analysis is employed. In this example, the circuit is supplied by a current source of 10 A, 85 kHz, and voltage across the coils are measured. L and M are computed using the obtained data.

7.6 Results

This section is mainly dedicated for dynamic wireless charging (DWC). In DWC system, more than one transmitter coil constitute a track. Basically, track has two types: stretched and lumped. A stretched track is constituted by a coil whose dimension in the EV-moving direction is much longer than the pickup coil while lumped track is built up with a

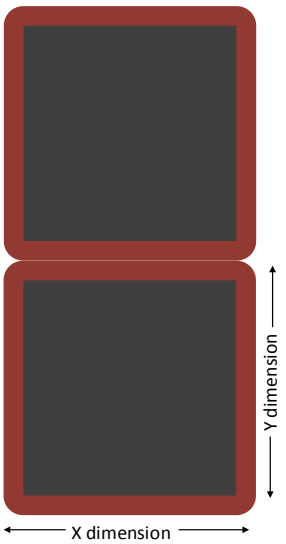

Table 7.1

Parameters	Value (in mm)
Core thickness	10
Core X dimension	375
Core Y dimension	435
Coil X dimension	375
Coil Y dimension	450
Coil distance	190
Wire radius	4.5
Turn No	4

string of coils having dimensions comparable to the pickup coil. For our case of study, three DD coils are considered as a track while receiver or pick up has only one DD coil.

Design of track has been done with some assumption such as

1) The track coils are supplied with the same sinusoidal current i_t having constant peak magnitude I_t and angular frequency ω_s.
2) EV moves along the line passing through the track coil centers.
3) The EV speed is constant.
4) Track and pickup coils are equal as well as their core.

JMAG simulation is executed with track and pickup having parameters listed in Table 7.1. All the coils are DD where T_1, T_2 and T_3 represent three transmitter coils while R the receiver or pick up coil as can be seen in Fig. 7.5.2. Mutual inductance between each track and receiver coil is 15 μH when they are perfectly aligned. Variation of Mutual inductance w.r.t. movement of coil R from coil T_1 to T_3 (shown in Fig. 7.5.2) has been studied here.

Plot of mutual inductance between T_2 and R is shown in Fig. 7.6.1 which increases from zero up to the maximum value of 15μH and then starts decreasing. X axis of this plot represents displacement of R which ranges from 1 to 73 where single increment represents a displacement of 20mm of receiver. Reason for this behavior is the fact that, during beginning and completion, coil R is very far fromT_2 while at a certain time it is totally aligned with it giving maximum mutual inductance.

Fig. 7.6.2 plots the mutual inductance among all the transmitter coils. X axis of this plot represents displacement of R which ranges from 1 to 73 where single increment represents a displacement of 20mm of receiver. There are three pairs of coils such as (T_1 & T_2), (T_2 & T_3)

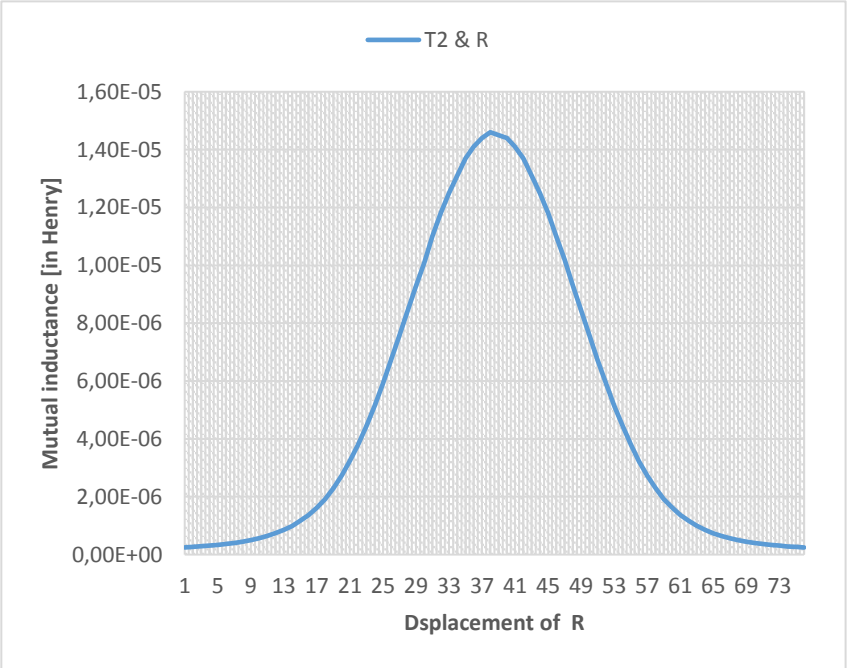

Fig. 7.6.1. Mutual inductance between T_2 and R when R is moving.

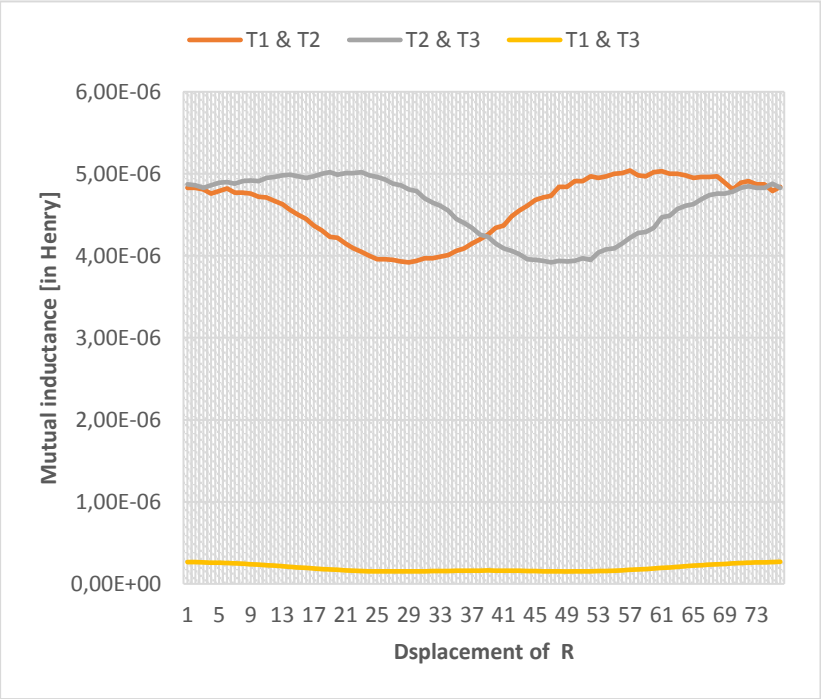

Fig. 7.6.2. Mutual inductance among all the transmitter coil when R is moving.

and (T_1 & T_3) .Mutual inductance between (T_1 & T_2) and (T_2 & T_3) are higher than that of pair (T_1 & T_3). The obvious reason is that there is separation between (T_1 & T_3) while in the case of (T_1 & T_2) and (T_2 & T_3) separation is zero. Then mutual flux between the two coils with no separation will always be higher than that of one with some separation. Reluctance of magnetic path between (T_1 & T_2) is lower than that of between (T_2 & T_3) as receiver approaches to T_2 and hence, mutual inductance between (T_1 & T_2) is higher than that of between (T_2 & T_3) in the first half of Fig. 7.6.2. Similar explanation can be given for the second half of Fig. 7.6.1. While in the center, receiver is perfectly aligned to T_2, reluctance between (T_1 & T_2) and (T_2 & T_3) are the same. So, mutual inductance between (T_1 & T_2) is equal to that of between (T_2 & T_3).

7.6 Conclusions

The chapter has investigated different coil arrangements for WBC application. Classification of coil geometry is done mainly on the basis of their ability to couple or generate only the parallel, perpendicular or both components of flux. Two different types of coil such as polarized, non-polarized along with DD coil have been discussed in detail. Suitable DD coil for high power WBC application has been studied further. For simulation purpose, JMAG FEM tool has been used in this chapter. A transmitter track with three DD coils and receiver with one DD coil have been studied using JMAG while receiver moving.

7.7 References

[1] M. Budhia, G.A Covic, and J.T Boys, "Design and optimization of circular magnetic structures for lumped inductive power transfer systems," *IEEE Transaction on Power Electronics*, vol. 26, no. 11, pp. 3096-3108, November 2011.

[2] H. Takanashi, Y. Sato, Y. Kaneko, S. Abe, and T. Yasuda, "A large air gap 3 kW wireless power transfer system for electric vehicles," in Proc. of IEEE energy Conversion Congress and Exposition, 2012, pp. 269-274.

[3] R. Bosshard, J.W. Kolar, J. Muhlethaler, I. Stevanovic, B. Wunsch, and F. Canales, "Modeling and η-α-Pareto Optimization of Inductive Power Transfer Coils for Electric Vehicles," *IEEE Journal of Emerging and Selected Topics in Power Electronics*, vol. 3, no. 1, pp. 50-64, March 2015.

[4] F. Turki, R. Wiengarten, V. Reising, and A. Kratser, "Impact of the working frequency on wireless power transfer systems," in Proc. of Conf. for Power Conversion and Intelligent Motion (PCIM Europe), Nuremberg, DE, May 2014, pp. 1–6.

[5] M Budhia, G. A Covic, and J. T. Boys, "Design and Optimization of Circular Magnetic Structures for Lumped Inductive Power Transfer Systems" IEEE Trans. on Power Electronics, vol. 26, No. 11,pp. 3096-3108, Nov. 2011

[6] R. Bosshard, U. Iruretagoyena and J. W. Kolar, "Comprehensive Evaluation of Rectangular and Double-D Coil Geometry for 50 kW/85 kHz IPT System," *IEEE Journal of Emerging and Selected Topics in Power Electronics*, vol. 4, no. 4, pp. 1406-1415, Dec. 2016.

[7] F. Pellitteri, A.O. Di Tommaso, and R. Miceli, "Investigation of inductive coupling solutions for E-bike wireless charging," in Proc. of Power Engineering Conference (UPEC) 2015, pp. 1-6, 2015.

[8] G. A. Covic, M.L. G. Kissin, D. Kacprzak, N. Clausen, and H. Hao, "A bipolar primary coil topology for EV stationary charging and highway power by inductive coupling," in Proc. of IEEE Energy Conversion Congress and Exposition, 2011, pp. 1832-1838.

Chapter 8

Magnetic core material

8.1 Introduction

It is always expected that there could be a kind of "perfect" magnetic material with high permeability, low loss, and high flux density saturation which confers small core size and high efficiency to the inductive system of WBCS. But in reality, there is no such a "perfect" material, and hence it is needed to select the suitable one among the existing materials. One of the fundamental problem faced by the designers is, the power density in the core. High power levels require more core volume per unit of power which is typical for lower power levels. Ferrite, typically have the best cost/size/performance tradeoff along with low loss characteristics than other core materials. However, with a saturation limit of 0.3T, ferrites are not widely available in sizes that can deliver 10 kW and higher power levels. Even assuming its availability at this high power level, there is always a concern with the mechanical properties of the core. Many high power applications such as WBC, takes place in an environment exposed to shock and vibration, while, ferrite being a brittle material may undergo to fracture, particularly in large sizes. Due to inadequate quality of ferrite, powder magnetic materials have been considered for WBC applications.

This chapter starts with an overall introduction of magnetic materials, which includes, brief descriptions of ferrites and detail investigation of powder magnetic material. Approach to development of powder magnetic materials and their manufacturing process are depicted. Later on, classification of magnetic materials and their detailed investigations are presented. The chapter concludes with the comparison of all powder materials based on their magnetic properties like dependency of their permeability on temperature, magnetic field strength and frequency along with core loss and the cost of each material.

8.2 Magnetic material introduction

Magnetic materials have been so extensively used in a diverse range of applications, that the advancement and optimal utilization of magnetic materials would significantly improve our lives. Magnetic materials are classified in terms of their magnetic properties and their uses. If a material is easily magnetized and demagnetized, it is referred to a soft magnetic material, whereas, if it is difficult to demagnetize, it is referred to a hard (or permanent) magnetic material. The materials in between hard and soft are almost exclusively used as recording media and have no other general term to describe them.

Most of pure elements in the periodic table are either diamagnetic or paramagnetic at room temperature. Since they present very small magnetism under the influence of an applied field, they normally are termed as non-magnetic material. Another type of magnetism is called anti ferromagnetism, and the only pure element presenting this characteristic is Cr in natural environment. Fe, Co, and Ni are called ferromagnetic because, very high levels of magnetism can be observed if we apply a field to these materials. Actually, pure single element ferromagnetic materials are seldom seen as magnets or cores in practical applications, whereas alloys composed of these elements and other ingredients are more widely used.

Therefore, all of these alloys are also categorized as ferromagnetic. The last type of magnetic material is classified as ferrimagnetic. Although they cannot be observed in any pure element, they can be found in compounds, such as the mixed oxides, known as ferrites [1, 2].

In general, ferrimagnetic exhibit better loss performance but lower saturation flux density, compared with ferromagnetic one. Therefore, material researchers are trying to improve both types of materials, such as, ferrimagnetic and ferromagnetic. Meanwhile, the efforts to discover new materials are also ongoing.

Among all electrical, magnetic, and mechanical properties, the following characteristics of soft magnetics are of interests and can help to select a suitable one for certain application:

a) Relative permeability

b) Core loss

c) Saturation flux density

d) Temperature characteristics

8.3 Characteristics of conventional ferrite materials

Since the 1950's, ferrite materials have been developed for high-frequency applications because of their high electrical resistivity and low eddy current losses. The breadth of application of ferrites in electronic circuitry continues to grow. The wide range of possible geometries, the continuing improvements in the material characteristics and their relative cost-effectiveness make ferrite components the choice for both conventional and innovative applications.

Ferrite is a class of ceramic material with a cubic crystalline structure; and the chemical formula of $MOFe_2O_3$, where Fe_2O_3 is iron oxide and MO refers to a combination of two or more divalent metal (i.e. Zinc, Nickel, Manganese and Copper) oxides. The addition of such metal oxides in various amounts allows the creation of many different materials whose properties can be tailored for a variety of uses. Ferrite components are pressed from a powdered precursor and then sintered (fired) in a kiln. The mechanical and electromagnetic properties of the ferrite are heavily affected by the sintering process which is time-temperature-atmosphere dependent.

The saturation flux density ranges from 0.3~0.5 Tesla normally, and permeability varies from thousands to several tens of thousands. Typically, NiZn ferrites have lower saturation flux density and better loss performance compared to the MnZn ones. Therefore, NiZn ferrites have been used for ultra-high frequency applications.

Ferrite materials are located on the lower end for Curie temperatures and it has its highest permeability just before Curie temperature (T_c). Even though the magnetization is lost above the Curie temperature no permanent damage will be found in the ferrite material. The change is only in the magnetic properties and not in the physical structure of the material. However, the physical structure may crack if the material is exposed for rapid change of its temperatures, at above 4°C per minute [3].

8.4 Powder Cores

Powder material can consist of different chemical elements in order to obtain the properties required by the core. With powder material, the air gap in the core will be distributed evenly across the whole core instead of a gapped part, which is the case in a standard ferrite core [4]. The distributed air gap will give the material a better temperature stability as well as lower flux leakage. They also have a smoother reduction of permeability which starts much earlier than ferrites. The permeability of the core depends on the size of the powder particles, the smaller the particle the lower the permeability becomes.

8.4.1 Approach of Powder magnetic material development

Figure 8.4.1 summarizes the controlling factors that affect iron loss in powder magnetic core materials [5]. Iron loss is the sum of hysteresis loss (W_h) and eddy-current loss (W_e). The hysteresis loss (W_h) is equivalent to the conversion loss (loop area) in a static magnetic field, and serves as the minimum energy required to change the magnetic field direction in the material. Then, the lower the coercive force (H_c) (i.e. the threshold value for the magnetic field change) of a material, the lower the loss. At high frequencies, the loss increases in proportion to the frequency of the magnetic field change (operation frequency) per unit time ($W_h \propto H_c \times f$). Meanwhile, the eddy current loss (W_e) increases significantly during high frequency operation. The eddy current loss (W_e) is the joule loss of the induced current due to the electromotive force generated by electromagnetic induction in response to the magnetic field change. The higher the electrical resistance (ρ) of a material, or the smaller the size of the area where the eddy current is generated (d) (equivalent to the particle diameter of insulated soft magnetic powder in the case of soft magnetic composite core materials), the lower the loss. The electromotive force increases in proportion to the magnetic field change speed (i.e. frequency), and therefore is in proportion to the square of the frequency per unit time ($W_e \propto d \times f^2 / \rho$.). The eddy current loss (W_e) increases in proportion to the powder particle diameter, because the increase in the particle diameter increases the area where the eddy current is generated. Meanwhile, the larger the powder particle diameter, the lower the hysteresis loss (W_h). This is because the increase in the particle diameter reduces the percentage of the particle surface area (i.e. magnetic gap) in relative terms. While W_h is proportional to the frequency, W_e is proportional to the square of the frequency, so reducing W_e can become prominent within the high-frequency ranges.

8.4.2 Manufacturing of powder core

Powder cores are obtained by compressing metallic powders which are electrically insulated from each other by an insulation layer at the particular surface providing a distributed air gap in the final material. The resulting density of the compactness leads to a variation in permeability values to be obtained. Small air gap distributed evenly throughout the core increases the amount of DC that can be passed through the winding before core saturation takes place. Powder cores that are not present with an organic binder do not exhibit any thermal aging effects.

A typical processing route used for the production of powder cores is illustrated in Fig. 8.4.2 [6]. Firstly, powders are prepared by atomization from a molten alloy with desired chemical composition. Atomization is a powerful powder fabrication technique in which the

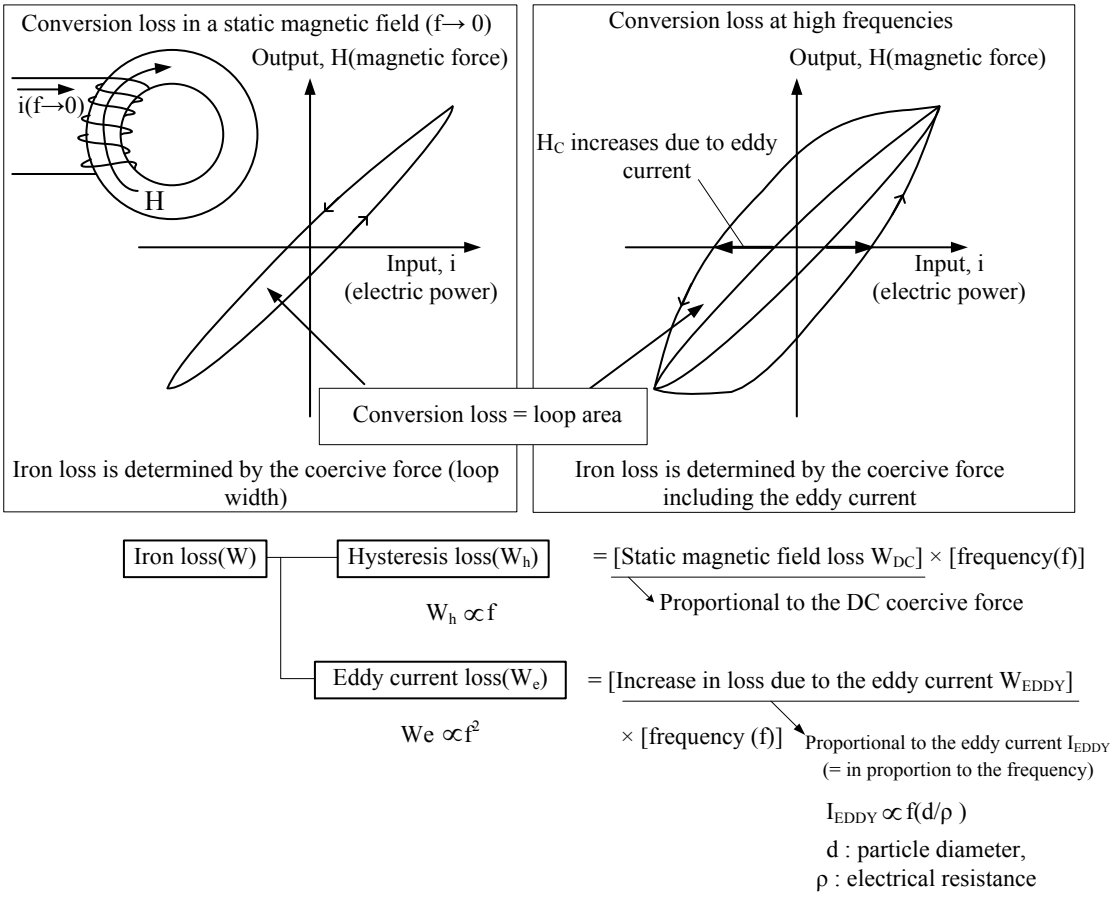

Fig. 8.4.1 Magnetic hysteresis loop and conversion loss of powder soft magnetic core materials

powder chemistry and shape characteristics can fully be controlled. Alternatively, powder material can also be obtained through grinding high permeability materials. If necessary, powders can be classified by sieving before the next step in order to obtain a desired particle size distribution. Following powder preparation, the particles are mixed with isolation means and binders to obtain a homogeneous distribution. Mixed powders are compacted in a mold, applying an external pressure to deform them, which eventually leads to shape and dimension control in the compacted bodies (green bodies) where necessary

As the next step, green bodies are sintered at an elevated temperature, specific for the alloy under consideration, which is usually below its melting point. This process creates bonding between the particles by atomic transport events that leads to the ultimate densification in the final product. An annealing step might succeed sintering in order to homogenize the microstructure. A relatively high-density structure almost free from residual voids can be obtained after the sintering process. Finally, during the finishing step, core surface is covered with an organic coating which provides a tough chemical resistance and high dielectric protection for the cores. Powder core materials, which are mainly used in low loss, high frequency and high power application, can be divided into six main groups according to their compositions:

a) Iron Powder

b) MPP (Molypermalloy Powder)

c) High flux

d) Sendust

e) FluxSan

f) Optilloy

8.4.3 Iron Powder

Iron powder used in magnetic cores consists of pure iron, Fe, and it is built up of small particles isolated from each other [7]. There exist different types of iron powder, for instance, hydrogen reduced and carbonyl iron. The carbonyl iron is usually used in radio frequency applications since they have good temperature stability, whereas the hydrogen reduced iron commonly is used for DC-chokes, mainly because of their higher permeability. Iron powder has rather high losses compared to the other powder materials, but this can be compensated for applications where size is not an issue and when low cost is important. Iron powder saturates between 1-1.5T and usually has a relative permeability ranging between 1-90μ. One major drawback with iron powder has been that the binder used for isolating the grain particles, typically epoxy, is organic and thereby is exposed to thermal aging [4]. This makes the material sensitive for high temperatures, usually above 125°C, and this will cause the material to change its magnetic properties. Recent studies on the new binding material has pushed the temperature; some manufactures now guarantee that their cores are aging free up to 200°C. More about thermal aging, can be seen in section 8.5.

8.4.4 MPP (Molypermalloy Powder)

Molypermalloy powder, MPP, was introduced in 1940 and was first used to compensate the capacitance from long telephone lines. The core is very stable in terms of flux density, DC-current and temperature. MPP generally has the lowest losses of all the powder materials and is used when a higher saturation level is needed without increasing the losses. The drawback is the cost, which is many times more than that of conventional ferrites, and the geometry which is limited to toroidal shapes. According to Magnetics, their MPP cores consist of a mix of 2% molybdenum, 17% iron and 81% nickel and the relative permeability ranges from 14-550. The frequency spectrum varies depending on which manufacturer's specification is regarded. Magnetics says that the range for their cores goes up to 1 MHz, whereas Micrometals only goes up to 200 kHz [8].

8.4.5 High flux

High flux consists of 50% iron and 50% nickel powder and is used when very high

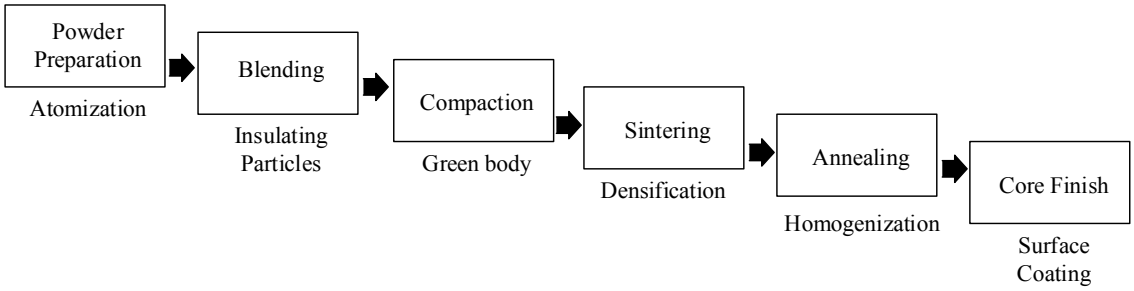

Fig. 8.4.2 Processing route used for the production of powder cores.

saturation, in the range of 1.5T, is needed [9]. The losses are higher compared to MPP but much lower than the iron powder. High flux cores are the best powder cores when it comes to keep its permeability roughly constant when the DC-bias is increased. Because of the permeability of the material, High flux cores are smaller than the standard iron powder core which makes them more suitable in applications where space is an issue. High flux cores have relative permeability between 14-160μ and a frequency range up to 200 kHz. High flux cores, like the MPP core, are only available in toroidal shapes.

8.4.6 Sendust

Sendust cores, also called Kool Mu cores, was invented in Japan 1936 and consists of 85% iron, 9% silicon and 6% aluminum [10]. They saturate at around 1T and fit between iron powder and High flux cores if compared in terms of both losses and cost. The available relative permeability for Sendust cores are between 14-125μ. Sendust is cheaper than both MPP and High flux because, there is no nickel in the alloy which makes the production process easier. Sendust cores are available in toroidal and E shape as well as in block shapes. The frequency range is again different between Magnetics and Micrometals which states the range to 500 kHz and 1 MHz respectively.

8.4.7 FluxSan

FluxSan consists 93.5% Fe and 6.5% Si. It saturates at around 1.67T while core loss is higher than all the other magnetic material except iron powder. This is third cheapest magnetic material after iron powder and Sendust, and are available in toroidal and E shape cores as well as in block shapes. The frequency range is 200 kHz and available relative permeability are between 14-90μ for Micrometals.

8.4.8 Optilloy

Optilloy has a combination of Fe, Si, Al and Ni. Core loss of Optilloy is close to Sendust and in some cases increases from it. Availability of Optilloy is only in toroidal shape and high saturation range of about 1.3T. The frequency range is 200 kHz and available relative permeability are between 14-125μ for Micrometals.

8.5 Thermal aging and temperature dependence

The aging of core materials depends on the binding material of the powder. In iron powder the binding material is constructed of epoxy which often is organic and is therefore affected by the heat in core that can lead to thermal aging. When the binder has been exposed to high temperature, the core losses will increase [11]. Once the core has been affected by high temperature, the process is irreversible i.e the core losses will increase with time. Therefore, it is important to stay within the temperature limit when operating with iron powder. Iron powder as an example, has Curie temperature of over 700°C, but the binder that holds the particles together, which usually is epoxy or phenol, has a considerable lower temperature limit. This limit has been around 125°C but manufacturers now claim to have binders that can withstand temperatures up to 200°C.

The Curie temperature of powder materials, such as the MPP, Sendust and High flux is between 450-500°C but the most important part is that, the binder that keeps the grains

together is non organic, which makes it free from thermal aging. The rated temperature is still usually put to 200°C because of the epoxy finish at the surface of the core. The fact, that these materials do not inherit the thermal aging effect until 200°C, makes them ideal for working operations with continuously high temperatures. Another important aspect to consider when it comes to temperature is the change in permeability that might occur. This will change the performance of the inductor, which in turn will affect the output ripple. If comparing the powder materials, MPP has the best temperature stability with a change of only 1.5% at 160°C where High flux, Optilloy, Fluxsan and Sendust deviate by 2%, 2%, 5.8% and 6% respectively (this comparison is for the 60μ). An interesting observation is that the permeability increases for both MPP and High flux whereas it declines for others. The deviation in temperature is greater for higher permeability.

8.6 Magnetic material performance

Table I compares all the above explained powdered magnetic material on the basis of their magnetic properties such as change in permeability with frequency and DC bias, core loss, cost and B_{sat} limit.

i) Change in initial permeability (μi) with respect to frequency:- It can be understood from (8.6.1) that, self-inductance (L) is dependent on permeability (μ) and, so, change in permeability bring variation in self-inductance. An application, based on magnetic resonance, is highly affected by the parameter variation and should be taken into consideration. Second column of Table 8.1 lists the % change of initial permeability (μi) when frequency reaches upto 1 MHz

$$L = \frac{\mu N^2 A}{l} \tag{8.6.1}$$

Here L, N, A and l are self-inductance, no of turns, cross section area and average length of coil respectively.

ii) DC bias operation:- Change in permeability with respect to magnetizing force is listed in the third column of Table 8.1. Here, manufacture values of magnetizing force obtained from Micrometals required to reach 90% of initial permeability is considered. For high magnetizing forces, the High flux core is the strongest material since the permeability is kept at a constant high value. The other powder materials have a higher reduction of their permeability where Optilloy and Fluxsan with identical behavior are slightly better than Sendust and MPP.

iii) Relative cost and Core loss:- Relative cost and core loss of different magnetic materials are listed in the fourth and fifth column of the Table 8.1 respectively. Price is estimated

Table 8.1

Magnetic material (60μ)	Change in μ_i [%]	Magnetizing force [Oe]	Relative cost	Core loss	Shape	B_{sat} (T)
MPP	96	32	10-18	12.6	T	0.88
High flux	90	47	7-9	27.8	T	1.48
Sendust	98	30	2-3	12.9	T, E & B	0.89
Fluxsan	97	40	2-4	24.2	T, E & B	1.67
Optilloy	96	41	6-7	15.9	T	1.3

relative to the least expensive iron material from Micrometals based on 25mm toroidal geometry. MPP is found to be most expensive material to be used while Sendust and Fluxsan are approximately the cheapest magnetic material. Other magnetic material such as High flux and Optilloy lie intermediate to them. As far as core loss is concerned, MPP has the lowest loss while High flux is the lossiest magnetic material.

8.7 Conclusions

Study of different magnetic materials, including ferrites and several powder magnetic materials are considered in this chapter. Starting with the limitation of ferrites for high power application and urge of powder magnetic material with superior characteristics are explained. Based on their composition, powder magnetic materials are classified into six types where each type carry their own pros and cons. MPP performs better if it comes to temperature dependency, stability in terms of frequency change and core loss, but is the most expensive material available only in a single toroidal shape. A little compromise in the core loss and effect of magnetizing on μ_i accomplish Sendust as a better option available in the toroidal, E and block shapes. But both MPP and Sendust suffer from lower saturation value of around 0.8T. Fluxsan and High flux have higher B_{sat} value with a limitation of high core loss; moreover they are preferable for high saturation demanding application, whereas Fluxsan has the additional benefit of low cost and availability in different shape. While, Optilloy may be an intermediate choice between Fluxsan and High flux with lower core loss and moderate cost.

8.8 References

[1] Chih Wen Chen, "Magnetism and Metallurgy of Soft Magnetic Materials", Courier Dover Publications, 1986.

[2] E. F. Gordon, "Soft Magnetic Materials", IEEE Proceedings of the IEEE, Vol. 78, June, 1990, pp.947-972.

[3] "Using magnetic cores at high temperature, cg-06,"Magnetics, Inc, technical Bulletin.

[4] Learn more about powder cores. Magnetics, Inc. Accessed 2013-07-04. [Online]. Available: http://www.mag-inc.com/products/powder-cores/learn-more-about-powder-cores

[5] N. Igarashi, M. Uozumi, T. Kosuge, A. Sato, K. Kusawake, and K. Yamaguchi "Pure Iron Based Soft Magnetic Composite Core That Enables Downsizing Automotive Reactors," SEI Technical Review, No. 80, pp. 98-103 (2015).

[6] Xose M.López-Fernández, H. Bülent Ertan, and J. Turowski. 2013. Transformers: analysis, design, and measurement. London New York. CRC press

[7] Iron powder cores. KDM Co.Ltd. Accesed 2013-07-04. [Online]. Available: http://www.kdm-mag.com/products/Iron-Powder-Cores1/

[8] "Micrometals arnold powder cores catalog," Micrometals Arnold Powder cores, 2012, product Catalog.

[9] "Learn more about high flux cores," Magnetics Inc., accesed 2013-05-31. [Online]. Available http://www.mag-inc.com/products/powder-cores/high-flux-cores/learn-more-high-flux

[10] T.Slatter, “A comparson of molybedenum permalloy powder and sendust cores for energy storage inductors.” Arnold Engineering company,May 2000.
[11] Thermal aging. Micrometals, Inc. Accessed 2013-07-04. [Online]. Available: http://www.micrometals.com/thermalaging index.html

Chapter 9

Dynamic modeling of WPT system

9.1 Introduction

Although WPCs are well known since some years, both the design and analysis of such system are still carried out by using simple steady - state model due to their complex nature. On the other hand use of digital hardware to implement a controller does not allow to control the waveform of such fast signals. Consequently, the control system must be designed using the transfer function between the envelope of the input and output signals of the system instead of using the common practice of considering their actual waveforms. The existing dynamic model of WPT system are set forth by two available methods such as Generalized state space averaging (GSSA) [1]-[3] and Laplace phasor transform (LPT) [4]-[6] technique that consider the envelope of the alternating signals. This chapter examines the features of the two methods. As a study case, the receiving circuit of a series-resonant WPT system is picked up. Before facing the modeling of the study case, the chapter illustrates how the two methods describe the dynamics of a resonant circuit and exemplifies this for a linear series-resonant circuit.

9.2 Series-resonant circuit

The schemes of the two circuits analyzed in the chapter are drawn in Figs.9.2.1 and 9.2.2 (a). Fig.9.2.1 shows the linear series-resonant circuit; in the scheme, R_B is the load, and L_R and C_R resonate at the frequency

$$f = \frac{1}{2\pi\sqrt{L_R C_R}} \tag{9.2.1}$$

Frequency in (9.2.1) is supposed to have a high value of 85 kHz. The voltage v_R(t) of the power source is a sinusoidal wave oscillating at the frequency in (9.2.1). Fig.9.2.2 (a) shows the receiving circuit of a series-resonant WBC system. Simplifying Fig. 9.2.2 (a) and referring battery to the chopper input results in a resistance R_B.

Due to the high-frequency sinusoidal oscillations of the voltages v_R(t) soliciting the circuits, any circuital AC variable in Figs.9.2.1 and 9.2.2 (b) has the waveform of a sine modulated in amplitude. It can be expressed as

$$u(t) \triangleq \hat{u}(t)cos\left[\omega t + \theta_{0,u}(t)\right] \tag{9.2.2}$$

were $cos\left[\omega t + \theta_{0,u}(t)\right]$ is a high-frequency term oscillating at the same frequency of the solicitation, termed as the carrier of the waveform, $\theta_{0,u}(t)$ is the initial phase of the

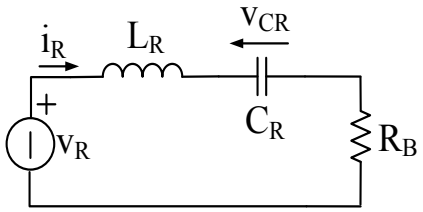

Fig. 9.2.1. Linear series-resonant circuit.

carrier, and $\hat{u}(t)$ is a low-frequency positive term, termed as the envelope of the waveform.

9.3 GSSA method

The GSSA method [1]-[3] relies on the representation of a variable with an expression like in (9.2.2) by means of its complex Fourier series

$$u(t) = \sum_{k=-\infty}^{k=+\infty} \langle u \rangle_k(t)\, e^{jk\omega t} \tag{9.3.1}$$

were ω is the angular frequency of the Fourier series and $\langle u \rangle_k(t)$ is the Fourier coefficient of order k; ω is equal to $2\pi f$, with f given in (9.2.1), whilst $\langle u \rangle_k(t)$ is a complex number calculated as

$$\langle u \rangle_k(t) = \frac{1}{T} \int_{t-T}^{t} u(\tau)\; e^{-jk\omega\tau}\, d\tau \tag{9.3.2}$$

As a matter of fact, (9.3.1) is the complex Fourier series of a periodic variable attained by snapshotting u(t) during the time window T and extending it along the whole time axis. In general, u(t) is not a periodic variable so that the Fourier coefficients depend on the initial instant t-T of the time window in (9.3.2). An important property of (9.3.2) is

$$\langle u \rangle_{-k}(t) = \langle u \rangle_k^*\,(t) \tag{9.3.3}$$

were * stands for conjugate.

Since u(t) has a predominant sinusoidal content, it can be approximated by the first-order terms in (9.3.1).

$$u(t) \cong \langle u \rangle_{-1}(t)\, e^{-j\omega t} + \langle u \rangle_1(t) e^{j\omega t} \tag{9.3.4}$$

By (9.3.3), equation (9.3.4) can be rewritten as

$$u(t) \cong 2\mathrm{Re}\left[\langle u \rangle_1(t) e^{j\omega t}\right] \tag{9.3.5}$$

were Re[ ] stands for "real part". Equation (9.3.5) is the transformation utilized by the GSSA method to describe the resonant circuit dynamics, being $\langle u \rangle_1(t)$ the transformed variable.

Using the equality

$$\frac{d\mathrm{Re}[\cdot]}{dt} = \mathrm{Re}\left[\frac{d(\cdot)}{dt}\right] \tag{9.3.6}$$

the time rate of (9.3.5) can be written as

$$\frac{du(t)}{dt} \cong 2\mathrm{Re}\left\{\left[\frac{d\langle u \rangle_1(t)}{dt} + j\omega \langle u \rangle_1(t)\right] e^{j\omega t}\right\} \tag{9.3.7}$$

i.e. is the sum of the time rate of $\langle u \rangle_1(t)$ and the product of $j\omega$ by $\langle u \rangle_1(t)$. This corresponds to replace the operator s in the Laplace transform of u(t) with the operator $s+j\omega$ in that of $\langle u \rangle_1(t)$

$$s \rightarrow s + j\omega \tag{9.3.8}$$

Calculation of Re[ ] in (9.3.5) yields

$$u(t) \cong 2|\langle u \rangle_1(t)|\cos(\omega t + Arg[\langle u \rangle_1(t)]) \tag{9.3.9}$$

where | | and Arg[ ] stand for "absolute value" and "argument", respectively. From the comparison of (9.3.9) and (9.2.2), it is recognized that i) the envelope of u(t) is equal to

$$\hat{u}(t) \cong 2|\langle u\rangle_1(t)| \tag{9.3.10}$$

and ii) the initial phase $\theta_{0,u}(t)$ of the carrier of u(t) is equal to $Arg[\langle u\rangle_1(t)]$.

Some properties of GSSA are

$$\begin{cases} \langle \frac{dx}{dt}\rangle_k = \frac{d}{dt}\langle x\rangle_k + jk\omega_s\langle x\rangle_k \\ \langle xy\rangle_k = \sum_{i=-\infty}^{\infty}\langle x\rangle_{k-i}\langle y\rangle_k \end{cases} \tag{9.3.11}$$

Method application

As an example, the GSSA method is applied to the circuit in Fig.9.2.1 with the end of computing the transfer function (TF) $S_{GSSA}(s)$ between the envelope of the current i_R(t) and that of the voltage v_R(t). The computation occurs in the state space and takes the following steps:

1. Write the system of linear differential equations relating the state variables of the circuit, namely i_R(t) and v_{CR}(t) as in (9.3.12)

$$\begin{cases} v_R = L_R\frac{di_R}{dt} + v_{CR} + R_B i_R \\ \frac{dv_{CR}}{dt} = \frac{i_R}{C_R} \end{cases} \tag{9.3.12}$$

Simplifying (9.3.12) gives

$$\begin{cases} \frac{di_R}{dt} = -\frac{R_B}{L_R}i_R - \frac{1}{L_R}v_{CR} + \frac{1}{L_R}v_R \\ \frac{dv_{CR}}{dt} = \frac{i_R}{C_R} \end{cases} \tag{9.3.13}$$

2. Apply (9.3.5) and (9.3.7) to both the state variables. This leads to

$$\begin{cases} \frac{d}{dt}\langle i_R\rangle_1 = -j\omega\langle i_R\rangle_1 - \frac{R_B}{L_R}\langle i_R\rangle_1 - \frac{1}{L_R}\langle v_{CR}\rangle_1 + \frac{1}{L_R}\langle v_R\rangle_1 \\ \frac{d}{dt}\langle v_{CR}\rangle_1 = -j\omega\langle v_{CR}\rangle_1 + \frac{1}{C_R}\langle i_R\rangle_1 \end{cases} \tag{9.3.14}$$

Notation of the transformed variables in (9.3.14) has been simplified by omitting (t).

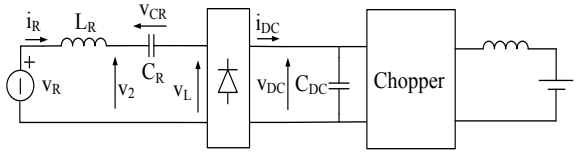

(a)

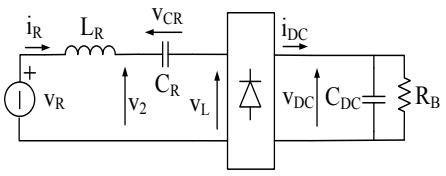

(b)

Fig. 9.2.2. (a) Receiving circuit of a resonant WPT EV charger, and (b) with battery resistance referred to the chopper input.

3. Use (9.3.2) to express the real and imaginary parts of $\langle v_R \rangle_1(t)$ as a function of the input variable $\hat{v}_R(t)$.

$$\begin{cases} \langle i_R \rangle_1 = x_1 + jx_2 \\ \langle v_{CR} \rangle_1 = x_3 + jx_4 \end{cases} \tag{9.3.15}$$

4. Separate the real and imaginary parts of the transformed state variables. System (9.3.14) turns into a system with a number of equations twice the state variables; for the circuit in Fig.9.2.1, they are four as

$$\begin{cases} \frac{dx_1}{dt} = -\frac{R_B}{L_R}x_1 + \omega x_2 - \frac{1}{L_R}x_3 + \frac{1}{2L_R}V_R \\ \frac{dx_2}{dt} = \omega x_1 - \frac{R_B}{L_R}x_2 - \frac{1}{L_R}x_4 \\ \frac{dx_2}{dt} = \frac{1}{C_R}x_1 + \omega x_4 \\ \frac{dx_3}{dt} = \frac{1}{C_R}x_2 - \omega x_3 \end{cases} \tag{9.3.16}$$

5. Then, compute the state matrix A and the input matrix B of the circuit

$$A = \begin{pmatrix} -\frac{R_B}{L_R} & \omega & -\frac{1}{L_R} & 0 \\ -\omega & -\frac{R_B}{L_R} & 0 & -\frac{1}{L_R} \\ \frac{1}{C_R} & 0 & 0 & \omega \\ 0 & \frac{1}{C_R} & -\omega & 0 \end{pmatrix}, B = \begin{pmatrix} \frac{1}{L_R} \frac{1}{2} & 0 & 0 & 0 \end{pmatrix}^T \tag{9.3.17}$$

6. Envelop of i_R can be given as

$$i_{R,env} = 2|\langle i_R \rangle_1| = 2\sqrt{x_1^2 + x_2^2} \tag{9.3.18}$$

The above equation is not linear which should be linearized around a steady state working point. This can be done with a small perturbation around the steady state of variable x_1 and x_2 as

$$\begin{cases} x_1 = X_1 + \tilde{x}_1 \\ x_2 = X_2 + \tilde{x}_2 \end{cases} \tag{9.3.19}$$

where X_1, X_2 are the steady state values of variable x_1 and x_2 while $\tilde{x}_1$ and $\tilde{x}_2$ are their perturbations. If the initial phase of v_R(t) is chosen in order that $\langle v_R \rangle_1(t)$ is real. Consequently, i_R has only real value and so X_2 is zero while X_1 is given as

$$X_1 = \frac{V_R}{R_L} \tag{9.3.20}$$

Using Taylor series expansion, (9.3.18) can be linearized as

$$\sqrt{x_1^2 + x_2^2} \cong \frac{X_1}{\sqrt{X_1^2 + X_2^2}}\tilde{x}_1 + \frac{X_2}{\sqrt{X_1^2 + X_2^2}}\tilde{x}_2 \tag{9.3.21}$$

Substituting (9.3.21) and (9.3.19) in (9.3.18) gives

$$i_{R,env} = 2\tilde{x}_1 \tag{9.3.22}$$

Output matrix C becomes

$$C = (2 \quad 0 \quad 0 \quad 0) \tag{9.3.23}$$

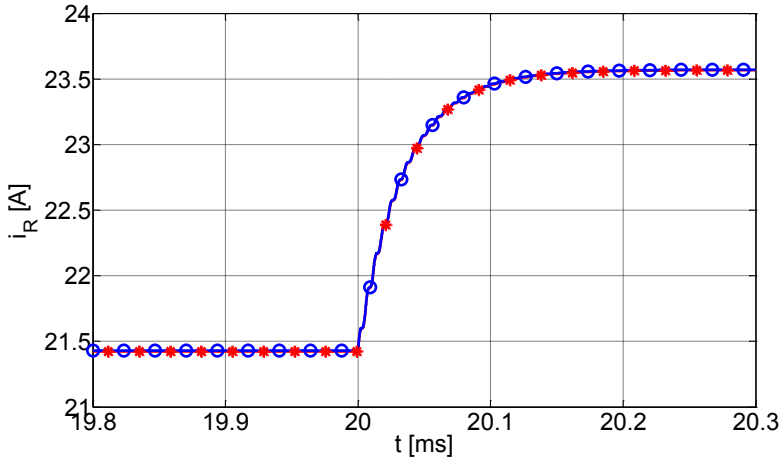

Fig. 9.3.1. Envelopes of the step responses obtained by simulation (red stars) and by model (blue circles).

7. Compute *S*(s) as

$$S_{GSSA}(s) = \mathrm{C}(sI - A)^{-1}\mathrm{B} \tag{9.3.25}$$

By (9.2.1), (9.3.17) and (9.3.23), $S_{GSSA}(s)$ results in

$$S_{GSSA}(s) \equiv \frac{\hat{I}_R(s)}{\hat{V}_R(s)} = \frac{1}{R_R} \frac{\frac{L_R^2 C_R}{R_B}s^3 + L_R C_R s^2 + \frac{2L_R}{R_R}s + 1}{\frac{L_R^3 C_R}{R_B}s^4 + \frac{2L_R^2 C_R}{R_B}s^3 + \left(L_R C_R + \frac{4L_B^2}{R_B^2}\right)s^2 + \frac{4L_R}{R_B}s + 1} \tag{9.3.26}$$

The circuit in Fig.9.2.1 has been implemented in Simulink, using the values of the parameters reported in the previous chapter, the purpose is to simulate the response of the current i_R(t) to a step of the voltage v_R(t) from 150 V to 165 V, impressed after the circuit had reached the steady-state conditions. The envelope of i_R(t) obtained by simulation is plotted in Fig.9.3.1, marked with red stars. As a comparison, the envelope of i_R(t) calculated by help of (9.3.26) is also plotted in Fig.9.3.1, marked with blue circles. The plots point out that the two envelopes match perfectly.

9.4 LPT method

A. Method background

The Laplace phasor transform (LPT) method [4]-[6] defines first the complex variable $\bar{u}$ associated to (9.2.2). The magnitude of $\bar{u}$ is set equal to the envelope of the variable in (9.2.2) and its phase is set equal to the initial phase of the carrier. Then, it construes (9.2.2) as the real part of the space phasor obtained by multiplying $\bar{u}$ by $\sqrt{2}e^{j\omega t}$, i.e. as

$$u(t) = Re\left[\sqrt{2}\bar{u}(t)e^{j\omega t}\right] \tag{9.4.1}$$

From (9.4.1), the envelope of *u(t)* is equal to

$$\hat{u}(t) = \sqrt{2}|\bar{u}(t)| \tag{9.4.2}$$

Equation (9.4.1) is the transformation utilized by the LPT method to describe the resonant circuit dynamics, being $\bar{u}(t)$ the transformed variable.

Comparison of (9.4.1) and (9.4.2) with (9.3.5) and (9.3.10), respectively, reveals the differences between the LPT and GSSA methods. They reside in i) the transformed variable:

it is a space phasor in the LPT method and the first-order coefficients of the complex Fourier series in the GSSA method, and ii) the coefficient relating the absolute value of the transformed variable to the envelope: it is equal to $\sqrt{2}$ in the LPT method and to 2 in the GSSA method.

Method application

The LPT method starts the computation of the TF S_{LPT}(s) between the output and the input variable of a resonant circuit by writing the relations between voltage and current of the R, L, C circuital elements, in agreement with (9.4.1),

$$\bar{v}_R(t) = R\,\bar{\imath}_R(t) \tag{9.4.3}$$

$$\bar{v}_L(t) = L\,\frac{d\bar{\imath}_L(t)}{dt} \tag{9.4.4}$$

Substituting $v_L(t)$ and $i_L(t)$ with the corresponding formula given by. (9.4.1) give

$$Re\{\sqrt{2}\,\bar{v}_L(t)e^{j\omega t}\} = L * \frac{d}{dt}Re\{\sqrt{2}\,\bar{\imath}_L(t)e^{j\omega t}\} \tag{9.4.5}$$

$$\sqrt{2} * Re\{\bar{v}_L(t)e^{j\omega t}\} = \sqrt{2} * Re\left\{\mathrm{L}\left[\frac{d\bar{\imath}_L}{dt}e^{j\omega t} + j\omega_s\bar{\imath}_L(t)e^{j\omega t}\right]\right\} \tag{9.4.6}$$

The previous equivalence is true if and only if the quantities inside the curly brackets are equal

$$\bar{v}_L(t)e^{j\omega_s t} = L\left[\frac{d\bar{\imath}_L}{dt}e^{j\omega_s t} + j\omega\bar{\imath}_L(t)e^{j\omega t}\right] \tag{9.4.7}$$

Finally, dividing Left Hand Side (LHS) and Right Hand Side (RHS) by $e^{j\omega t}$ the relation between the envelope current and the envelope voltage signals is obtained:

$$\bar{v}_L(t) = L\,\frac{d\bar{\imath}_L(t)}{dt} + j\omega L\,\bar{\imath}_L(t) \tag{9.4.8}$$

Following the same steps, equation for $\bar{\imath}_C(t)$ can be written as

$$\bar{\imath}_C(t) = C\,\frac{d\bar{v}_C(t)}{dt} + j\omega C\,\bar{v}_C(t) \tag{9.4.9}$$

Then, for the circuit in Fig.9.2.1, LPT method proceeds with the following steps:

1. Redraw the circuit using (9.4.3), (9.4.8) and (9.4.9). The circuit takes the configuration of Fig. 9.4.1. Weird components such as resistors with imaginary resistance appear in the circuit.
2. Write the TF, denoted with F(s), between $\bar{V}_R(s)$ and $\bar{I}_R(s)$ for the circuit of Fig.9.4.1.
3. Split F(s) into two TFs, F_{Re}(s) and F_{Im}(s), given by the real and the imaginary parts of F(s); the splitting entails the rationalization of F(s) with the consequence that the degree of the denominator of F_{Re}(s) and F_{Im}(s) is twice that of F(s).
4. Linearize (9.4.2) around a steady-state working point; the TF *S*(s) between the envelopes of v_R(t) and i_R(t) becomes

$$S_{LPT}(s) = K_{Re}F_{Re}(s) + K_{Im}F_{Im}(s) \tag{9.4.10}$$

where K_{Re} and K_{Im} are coefficients that depend on the working point selected for the linearization.

By applying the procedure above, the same TF as in (9.3.26) is attained, meaning that the LPT and GSSA methods lead to the same model for the linear series-resonant circuit in Fig. 9.2.1.

9.5 Application to WBC

The main dissimilarity of the circuit in Fig. 9.2.2(a) with respect to that in Fig.9.2.1 is its non-linear behavior due to the diode rectifier.

Let us assume that the diode rectifier conducts continuously. Further to these assumptions,

1. voltage v_{DC}(t) is a DC variable with the amplitude that changes during the circuit transients,
2. current i_{DC}(t) is the rectified counterpart of i_R(t); then, it is a pulsating variable that comprises a DC component, given by its average value, and an harmonic content at angular frequencies multiple of 2ω, which are shortened by the capacitor. It follows that only the DC component of i_{DC}(t) contributes to the dynamics of v_{DC}(t)

A. GSSA modeling

Under transients, the GSSA method calculates the DC components of v_{DC}(t) and i_{DC}(t) from (9.3.2) by putting k=0. On the other side, the DC component of i_{DC}(t) is related to the envelope of i_R(t). The relationship is found by observing that i) the envelope of i_{DC}(t) is the same as that of i_R(t), given by $2|\langle i_R \rangle_1||$ and ii) the DC component of i_{DC}(t), given by its average value, is $2/\pi$ times its envelope. Then, the dynamics of the C_{DC}-R_B mesh can be written as

$$\frac{d<v_{DC}>_0}{dt} = \frac{1}{C_{DC}} \frac{4}{\pi} |\langle i_R \rangle_1| - \frac{<v_{DC}>_0}{R_B C_{DC}} \tag{9.5.1}$$

As per point 3) above, the transformed variable of v_L(t) is

$$\langle v_L \rangle_1 = \frac{2}{\pi} < v_{DC} >_0 \; e^{j\varphi_{i_R}} \tag{9.5.2}$$

were φ_{i_R} is the phase of $\langle i_R \rangle_1$.

The description of the circuit in Fig.9.2.2 (b) is achieved by completing the system in (9.3.14) with (9.5.1) and (9.5.2). Compared to the circuit in Fig.9.2.1, the description has an additional state variable, given by $< v_{DC} >_0$. Apart from this, the computation of the TF between the envelopes of i_R(t) and v_R(t) proceeds as in Section 9.3. Because of the non-linearity of (9.5.1), linearization of the resulting system around a steady-state working point is necessary before computing the matrixes A and B. In general, the resulting FT of the circuit of Fig.9.2.2 (b) is of the fifth-order; here, using the values of the circuital parameters, a real

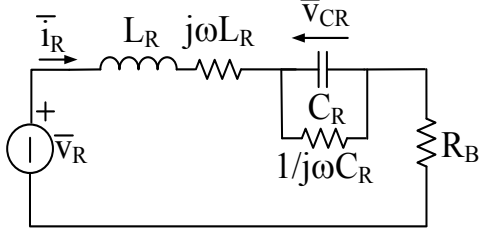

Fig. 9.4.1. Linear series-resonant circuit model by the LFT method.

zero-pole cancellation occurs and the order of FT reduces to four. Its expression is given in (9.5.3). The remaining zeros and poles of (9.5.3) are listed in (9.5.4) and (9.5.5), respectively.

$$S_{GSSA}(s) = 0.176\,\frac{3.65e{-}15\,s^3+8.81e{-}11\,s^2+2.1e{-}3\,s+1}{7.73e{-}20s^4+1.86e{-}15\,s^3+8.83e{-}8\,s^2+4.23e{-}5\,s+1} \tag{9.5.3}$$

$$z_1 = -476, \quad z_{3,3} = -1.18e^4 \pm \mathrm{j}\,7.57\mathrm{e}^5 \tag{9.5.4}$$

$$p_{3,4} = p_{1,2} = -238.1 \pm j\,3347, -1.18e^4 \pm \mathrm{j}\,1.07\mathrm{e}^6 \tag{9.5.5}$$

Like for circuit in Fig.9.2.1, the circuit in Fig.9.2.2 (b) has been implemented in Simulink to simulate the response of the current i_R(t) to a step of the voltage v_R(t). Simulation conditions are the same as before. The envelope of the response obtained by simulation is plotted in Fig.9.5.1, marked with red stars, together with that calculated by help of (9.5.3), marked with blue circles. Again, the plots point out that the two envelopes match perfectly.

B. LPT modeling

With the LPT method, the C_{DC}-R_B mesh is referred to the input of the diode rectifier. Referral is achieved by exploiting the fact that $v_{L,1}$(t) is in phase with i_R(t) and, hence, that its transformed counterpart can be expressed as

$$\bar{v}_{L,1}(t) = \frac{\bar{\imath}_R(t)}{|\bar{\imath}_R(t)|}\,\left|\bar{v}_{L,1}(t)\right| = \bar{\imath}_R(t)\,\frac{\hat{v}_{L,1}(t)}{\hat{\imath}_R(t)} \tag{9.5.6}$$

where the second equality derives from (9.4.2). On the other hand, the average values of v_{DC}(t) and i_{DC}(t) are related to the respective envelopes by

$$v_{DC,avg}(t) = \frac{\pi}{4}\hat{v}_{L,1}(t), \quad i_{DC,avg}(t) = \frac{2}{\pi}\hat{\imath}_R(t) \tag{9.5.7}$$

so that (9.5.6) can be rewritten as

$$\bar{v}_{L,1}(t) = \bar{\imath}_R(t)\,\frac{8}{\pi^2}\,\frac{v_{DC,avg}(t)}{i_{DC,avg}(t)} \tag{9.5.8}$$

By (9.5.8), the impedance seen at the input of the diode rectifier is $8/\pi^2$ times the impedance connected at its output.

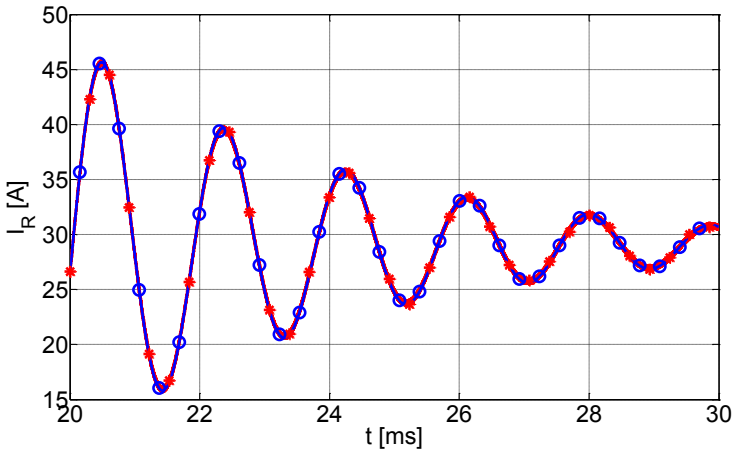

Fig. 9.5.1. Envelopes of the step responses obtained by simulation (red stars) and by GSSA and LPT (blue circles).

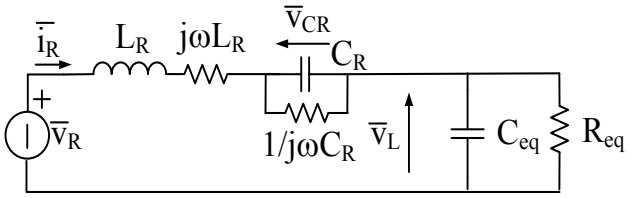

Fig. 9.5.2. Representation of the receiving circuit of a series-resonant WBC system with the LPT method.

$$C_{eq} = C_{DC}\frac{\pi^2}{8}, \quad R_{eq} = R_B\frac{8}{\pi^2} \tag{9.5.9}$$

The resulting representation of the receiving circuit of a series-resonant WBC system is shown in Fig.9.5.2.

Computation of the TF between the envelopes of i_R(t) and v_R(t) proceeds as in Section 8.4. In general, the resulting TF is of the sixth-order. Again, a complex zero-pole cancellation occurs and the order of the FT reduces to four. Its expression is given in (9.5.10). The remaining zeros and poles of (9.5.10) are listed in (9.5.11) and (9.5.12), respectively.

$$S_{LPT}(s) = 0.176\,\frac{3.65e{-}15\,s^3{+}1.74e{-}12\,s^2{+}2.1e{-}3\,s{+}1}{7.70e{-}20s^4{+}3.67e{-}17\,s^3{+}8.85e{-}8\,s^2{+}4.22e{-}5\,s{+}1} \tag{9.5.10}$$

$$z_1 = -476, \;\; z_{2,3} = = -0.0047 \pm \mathrm{j}\,7.58\mathrm{e}^5 \tag{9.5.11}$$

$$p_{1,2} = -238.5 \pm j\,3352, \;\; p_{3,4} = -0.0047 \pm \mathrm{j}\,1.07\mathrm{e}^6 \tag{9.5.12}$$

Despite the differences in the TFs, the envelope of the step response of the current calculated by (9.5.10), also plotted in Fig.9.5.1, is not discernible from that of (9.5.3). However, a close inspection of the envelopes unveils an oscillation at twice the operating frequency in the response calculated by the LPT method, as shown in Fig. 9.5.3 (red stars refer to the LPT method, blue circles to both the GSSA method and the simulation). This circumstance has been investigated by tracing the Bode diagrams of (9.5.3) and (9.5.10), normalized to the DC gain. The diagrams, traced in Fig.9.5.3, show that the TFs coincide in both their magnitude and phase, except at around twice the operating frequency, where the TF of the LPT method exhibits a peak of resonance. This finding supports the different behavior

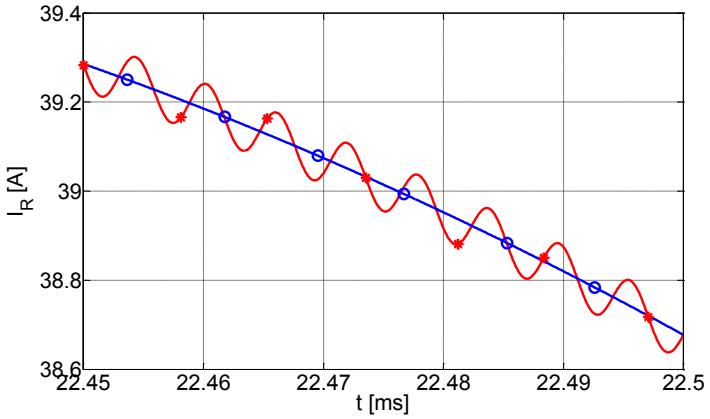

Fig. 9.5.3. Magnification of a time interval of the envelopes in Fig.9.5 (red stars refer to the LPT method, blue circles to GSSA method and simulation).

of the time responses calculated with the two methods.

9.6 Conclusions

The chapter has examined the features of two methods to model the dynamics of resonant circuits in view of their control. Two methods, namely GSSA and LPT, are available and have been considered in this chapter. With regard to the case of the receiving circuit of a series-resonance used in WPT system, the step response obtained with the GSSA modeling coincides with that of the circuit whilst that obtained the LPT modeling exhibits a superimposed oscillation at twice the operating frequency.

9.7 References:

[1] S.R. Sanders, J.M. Noworolski, X.Z. Liu, and G.C. Verghese, "Generalized averaging method for power conversion circuits," *IEEE* Trans. *on Power Electronics*, vol. 6, no. 2, pp. 251-259, Apr 1991.

[2] V.A. Caliskan, G.C. Verghese, and A.M. Stankovic, "Multifrequency averaging of DC/DC converters," *IEEE Trans. on Power Electronics*, vol. 14, no. 1, pp. 124-133, Jan 1999.

[3] H. Hao, G.A. Covic, and J.T. Boys, "An Approximate Dynamic Model of LCL-*T*-Based Inductive Power Transfer Power Supplies," *IEEE Trans. on Power Electronics*, vol. 29, no. 10, pp. 5554-5567, Oct. 2014.

[4] C. Park, S. Lee, G.H. Cho, and C.T. Rim, "Static and dynamic analysis of three-phase rectifier with LC input filter by laplace phasor transformation," in Proc. IEEE Energy Conversion Congress and Exposition (ECCE), 2012, pp. 1570-1577.

[5] C.T. Rim, "Unified General Phasor Transformation for AC Converters," *IEEE Trans. on Power Electronics*, vol. 26, no. 9, pp. 2465-2475, Sept. 2011.

[6] S. Lee, B. Choi, and C. T. Rim, "Dynamics Characterization of the Inductive Power Transfer System for Online Electric Vehicles by Laplace Phasor Transform," *IEEE Trans. on Power Electronics*, vol. 28, no. 12, pp. 5902-5909, Dec. 2013.

Conclusions

Elaborating the significance of Wireless charging of EVs, a review of three different wireless charging techniques as, electric, magnetic and electromagnetic radiation have been done. Magnetic or inductive power transfer technique (IPT) has been considered for wireless battery charger (WBC) system. Investigation of IPT revealed that it suffers from low efficiency and high power sizing factor of supply inverter which led to use resonant technique for the performance importance of WBC system.

The thesis performed a comprehensive analysis of the four one-element resonant topology i.e. SS, SP, PS and PP which can be used in wireless battery charger (WBC) system. It has been revealed that efficiency and sizing power parameters of the coil pair depend only on the receiver resonance topology while the sizing power of the supply inverter is influenced also by the transmitter resonance. Efficiency of SS and PS topologies outperforms that of the SP and PP one over almost all the typical range of low-medium power applications. Also the power sizing factors of the supply inverter and of the coupler are broad in favor of the SS and PS topologies, being the power sizing factor of the supply inverter of the SS topology a little lower. SP and PP are robust against short-circuit and open operation of the receiver terminals whereas the SS topology sustains only their short-circuit operation.

Favorable SS topology with two different WBC arrangements have been examined. Receiver of one arrangement charges the EV without chopper while other has a chopper cascaded with the diode rectifier. Figure of merits (FOMs) such as, overall efficiency, power transfer ratio, receiver efficiency and power sizing factor of both the supply inverter and the receiving coil of the two WBC arrangements have been formulated and calculated. Based on the evaluation and outcome of FOMs, receiver using chopper is found to be more suitable for WBC system.

Thesis continues with the analysis and affect of mismatch between supply and resonance frequency on efficiency and supply inverter power sizing factor due to variation of the reactive elements of the WBC system from their nominal values. Three possible strategies for updating the supply frequency have been proposed, namely the transmitter stage resonance (TSR), receiver stage resonant (RSR), and input impedance resonance (IIR) strategies to resonate the transmitter stage, receiver stage and input impedance respectively. The results of the analysis have unequivocally demonstrated that the RSR strategy endowed the WBC system with the lowest variations of efficiency and supply inverter power sizing factor. While, need of wireless transmission of high frequency receiver stage signal makes RSR inappropriate for the practical use. Eventually, between the two remaining approaches, IIR outperforms TSR in addition to the need of only transmitter stage signals. Henceforth, IIR is concluded to be the most feasible approach.

Later on, thesis focuses to extend the power range of the WBC system. For this, review of power supply architecture, core material and coil geometry is done. The power supply is classified in single stage, two stage and parallel power supply. All these three types of power supply architectures have been analyzed including their merits and demerits. Regarding core material; iron powder, MPP, High flux, sendust, Fluxsan and optilloy have been inspected on

the virtue of their B_{sat} value, thermal aging, and temperature dependence. As a results, sendust is found to be suitable for high power WBC system. Based on the literature survey, DD coil is found to be appropriate for high power application which has been analyzed and simulated successfully.

At last, thesis focuses on the control of WBC system. For this, thesis has faced modeling of a WBC system. The two available methods such as GSSA and LPT have been examined and applied to a study case. It has been shown that the step response obtained with GSSA coincides with that of the circuit more accurately than the LPT method.

Publications

[1] R.K. Jha, S. Giacomuzzi, G. Buja, M. Bertoluzzo, and M.K. Naik, "Efficiency and sizing power of SS vs. SP topology for wireless battery charging," in proc. of IEEE International Conference on Power Electronics and Motion Control (PEMC), 2016, Varna, Bulgaria.

[2] G. Buja, R.K. Jha, M. Bertoluzzo, and M.K. Naik, "Analysis and Comparison of Two Wireless Battery Charger Arrangement for Electric Vehicles," Chinese Journal of Electrical Engineering, vol. 1, no. 1, Dec. 2015.

[3] M. Bertoluzzo, R.K. Jha, and G. Buja, "Series-series resonant IPT system analysis under frequency mismatch," in proc. of IEEE Industrial Electronics Society (IECON), 2015, pp. 439-444